2008

Effect of conformational change on nanoscale friction behavior of organic thin films

Kanaga Karuppiah Kanaga Subramanian
Iowa State University

Effect of conformational change on nanoscale friction behavior of organic thin films

by

Kanaga Karuppiah Kanaga Subramanian

A dissertation submitted to the graduate faculty

in partial fulfillment of the requirements for the degree of

DOCTOR OF PHILOSOPHY

Major: Mechanical Engineering

Program of Study Committee:
Sriram Sundararajan, Major Professor
Pranav Shrotriya
Qingze Zou
Zhiqun Lin
Yan Zhao

Iowa State University

Ames, Iowa

2008

TABLE OF CONTENTS

ACKNOWLEDGEMENTS

Ever since the date for my final oral exam was finalized, I have been going through this list in my mind, of people whom I wanted to thank, in this important section of my dissertation. However, as any responsible graduate student would do, I did not try to put it down in writing ever!! Even though people near and dear to me claim that I have become real absent-minded over the last few years, am going to try and do justice in singling out all these people without whose love and support, I could not have completed this dissertation.

First and foremost, I would like to thank my advisor, Dr. Sriram Sundararajan for his guidance and constant support and the unswerving faith he had in me throughout my graduate studies. He showed me the need to be persistent to accomplish any goal. I still remember the first time I took my data to him for the research group meeting and the first question he asked was “Are you confident of the data?” Was I ? Thank you, for molding me from being a wobbly graduate student to a confident researcher and experimentalist. I am sure I cannot express my gratitude in these few lines, however, I will be ever grateful for all the knowledge that I have gained over the years which will be the foundation for every one of my forthcoming accomplishments.

I would also like to extend my sincere thanks to all my committee members: Dr. Pranav Shrotriya, Dr. Qingze Zou, Dr. Zhiqun Lin and Dr. Yan Zhao for serving on my POS committee and providing me with all the valuable inputs for my research, whenever I needed them. I owe a great deal to Dr. Shrotriya who has been ever willing to give suggestions on almost every project that I worked on. I also had a great time working for him for the “Surface stress generation” project. I would also like to thank all the collaborators who have

worked with me in the research projects: Dr. Xiaodong Li and Zhi-Hui Xu from University of South Carolina, Dr. Keith Woo and Yibo Zhou from Chemistry Department at ISU, Dr. Zhiqun Lin and Jun Wang from Materials Science Department at ISU, Dr. Abhijit Chandra and Ruqin Zhang from ME department at ISU. Thanks to all ME staff especially Patti Boone, Marti and Allison, for their willingness to help at all times.

I owe a lot to Dr. Andrew Hillier for his help with the goniometer and ellipsometry experiments and for patiently answering all my questions related to chemistry. I would like to thank Bob Doyle for his help with fluorescence measurements and for unstintingly clarifying anything and everything related to biology.

This acknowledgment would not be complete without the mention of all the lab colleagues (both Dr. S and Dr. Shrotriya's lab), former and present, with whom I have shared all my professional ups and downs and the mutual encouragement and boosting that we have showered on each other: Satyam, Chris, Rob, Jae-Joong, Dinesh, Kyungho, Xiao Ma, Yilei, Sharath, Vinay, Jason, Angela and Andrew.

I owe a lot to all my roommates and friends: Muthu, Sudha, Arun, Vikram and Venky who have been very understanding and a constant source of encouragement through every stage of these past 6 years. My sincere thanks to all the friends that I made in Ames with who I share a lot of pleasant memories – Rahul, Rajee, Shantha, Mothi, Vidya, Neeraj, Abhijit, Vatsan, Atul and numerous others.

Last but not the least: I would like to thank my family – my parents, sisters and brother-in-law. Without their unconditional love and support, I simply could not have accomplished whatever I have till now.

Financial support for this study was provided by National Science Foundation grants - grant No. CMS0609174, CMS0409625, Career grant CMMI-00547280 and a seed grant from US-DOE Ames Laboratory.

ABSTRACT

The overarching theme of this dissertation is to probe relationships between structure of organic thin films and their specific functional property of friction in the context of various engineering applications. Two specific thin film systems were studied – biological macromolecules in total joint replacements and self-assembled alkanethiol monolayers for microdevice applications. Before delving into the actual systems, a thorough understanding of friction at small length scales was required. To address this, a friction study of two material pairs (Si_3N_4/mica and Si_3N_4/ultra-high molecular weight polyethylene) was conducted using a microtribometer and atomic force microscope (AFM) at the micro- and nanometer length scales respectively, while keeping the environmental and counterface conditions same at both scales and thereby evaluating contact area dependence in the absence of surface damage and contact area independence when damage occurs.

Biological macromolecules such as proteins and lipids are important constituents of the synovial fluid which is the natural lubricant present in all of our human joints. The effect of adsorbed films of proteins and lipids on the micro/nanoscale tribological response of the polymeric materials used in total joint replacements (TJRs) were investigated. The friction and wear response of UHMWPE samples with different crystallinities was studied in the presence of bovine serum albumin protein and phospholipids. The observed friction increase upon exposure to proteins was attributed to the formation of a layer of denatured proteins on the surface. Changing the crystallinity and surface energy of UHMWPE affected the protein adsorption mechanism and the resulting increase in friction behavior. It was also found that increased crystallinity lowered the friction response and increased the scratch and wear

resistance at both micro and nanoscales. It was also found that higher crystallinity increased the adsorption of the phospholipid and acted as an effective lubricant reducing the friction response and increasing the wear resistance of the interface.

The surface stress generation during the formation of a self-assembled monolayer (SAM) of alkanethiols on a macroscale domain was investigated in order to exploit this effect for sensing systems. To that effect, a curvature interferometry technique was used to study the surface stress generated during the formation of octadecanethiol SAM on a 25 mm x 25 mm mica sample. It was seen that the magnitude of surface stress measured on macroscale domain compared well with previously reported measurement on micron sized domains.

The possibility of utilizing a SAM system as a means to achieve active friction modulation of a surface was also investigated. A low-density SAM system, shown to exhibit conformational changes in the presence of an electric field, was synthesized and its friction response was studied using an AFM. Friction experiments showed that in the presence of a positive bias, the film showed a higher friction response (up to 300%) than when a negative bias was applied. The difference in the friction responses was attributed to the changes in the structural and crystalline order of the film between the two bias conditions.

CHAPTER 1. INTRODUCTION

The overarching theme of this dissertation research is to probe relationships between structure of thin organic films and their specific functional property of friction in the context of various engineering applications. This introductory chapter outlines the background, motivation and objectives of the research work.

1.1 Background

Thin films are defined as thin layers of material which are deposited on a substrate to achieve properties at the surface that are not achieved by the bulk materials alone. Thickness of such films can vary anywhere from fraction of a nanometer (nm) to a few microns (μm). Thin films were originally developed for the need of the integrated circuit (IC) and semiconductor industry but now their applications are far-reaching. They are used in microelectronics,[1-4] optics,[5-8] magnetic,[9-12] hard and corrosion-resistant coatings[13-17] etc. Thin films can constitute any kind of material – metallic, non-metallic, organic, polymeric etc. In this dissertation, the emphasis will be on two kinds of thin films – ultrathin organic films (self-assembled monolayers) and biological macromolecule films (proteins and lipids).

1.1.1 Organic Thin Films

Thin organic films in the thickness range of a few to several hundred nanometers are being used in several areas such as photonics,[18-21] molecular optics,[8, 22-24] molecular electronics[25-28] and as lubricants for magnetic media[29-32] and microelectromechanical systems (MEMS).[33-35] Thin organic films could be either amorphous such as spin-coated polymer or

highly organized such as Langmuir-Blodgett (LB) or self-assembled monolayer (SAM) films. Self-assembled monolayers (SAMs) consist of a single layer of molecules on a substrate in which the molecules exhibit a high degree of orientation, molecular order and packing. The monolayer spontaneously forms upon exposure of the substrate to a solution or vapor containing the molecules as shown in Figure 1. Successful self-assembly requires a relatively strong bond between the substrate and the molecule, and an additional lateral interaction between molecules in the monolayer. Though several molecules have the ability to form a monolayer, the most commonly studied SAM is an alkanethiolate monolayer on a gold substrate. The alkanethiol consists of a sulphur head group, a long carbon backbone and a tail group. The sulphur group has an affinity to the underlying gold atom and attaches itself to the threefold hollow sites of the gold and thus forming a highly ordered ($\sqrt{3}$ x $\sqrt{3}$) R30° structure.

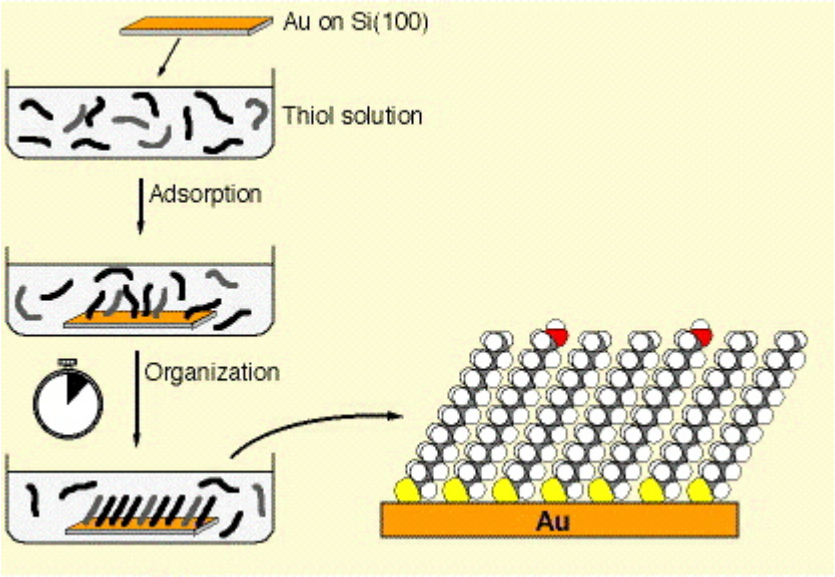

Figure 1: Schematic outline of SAM preparation (Source: http://www.ifm.liu.se/applphys/ftir/sams.html)

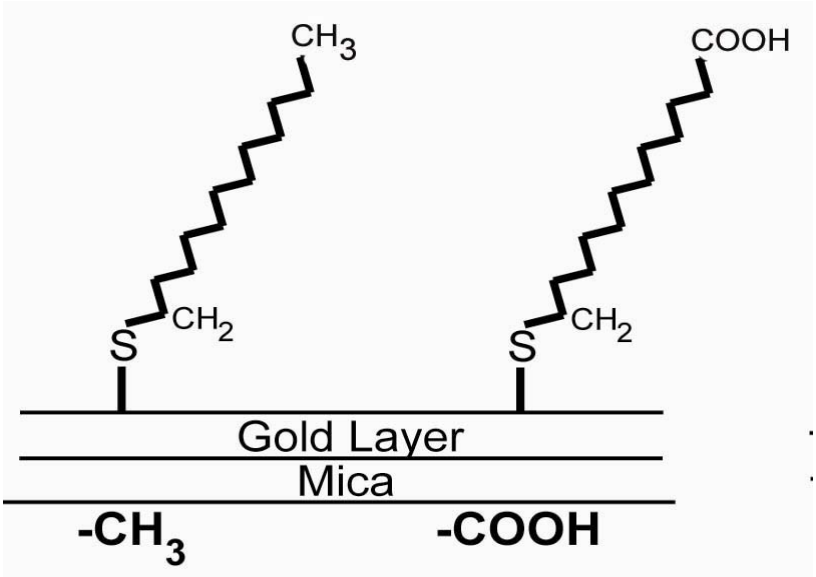

Figure 2: Structure of an alkanethiol molecule – Sulphur headgroup, carbon backbone and a tail group (-CH_3 and -COOH)

The Au-thiolate bond is very strong with bond strength of 44 kcal/mol. The ability to tailor the tail group and the backbone results in a myriad of possibilities for various applications. Figure 2 shows a schematic of a carboxylic acid (-COOH) terminated and methyl (-CH_3) terminated alkanethiol molecule.

Self-assembled monolayers as chemical and biological sensors

Thundat et al.[36] reported the deflection of atomic force microscope (AFM) cantilevers due to changes in relative humidity and ever since, AFM cantilever deflection based sensors have been on the rise. The deflection change could be induced by various factors such as pH,[37-40] temperature,[41-44] mass[45-48] or molecular adsorption.[49-52] Cantilever deflection due to various factors are shown in the form of a schematic in Figure 3. The generation of surface stress when self-assembled monolayers are forming on gold-coated cantilevers was first

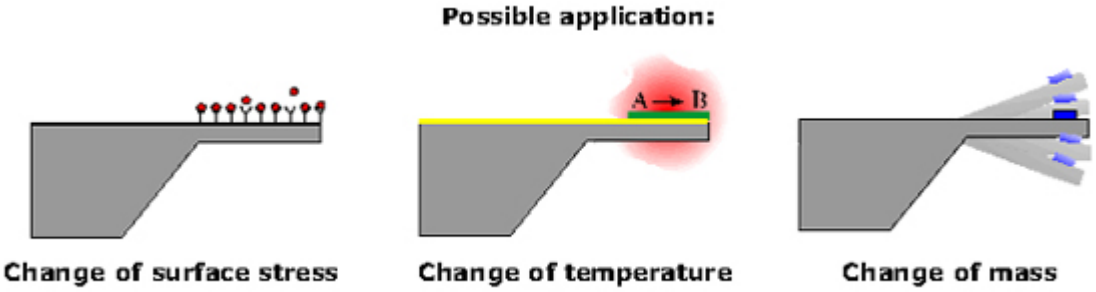

Figure 3: Possible factors inducing cantilever deflection (Source: http://www.nanotech.dtu.dk/research/nse/nanoprobes.aspx)

reported by Berger et al.[49] They reported that the induced surface stress increased with the chain length of the SAM. Fritz et al.[53] went a step further in using the surface stress generation as a biological sensor. In their work, a single-stranded DNA oligonucleotide was covalently immobilized onto a gold-coated cantilever using thiol chemistry and this introduced the initial surface stress. Once the complementary DNA strand was introduced, the hybridization of the two single strands was observed by the deflection of the cantilever and this introduced further surface stress. The analysis of the change in surface stress was used to distinguish strands differing by just one base pair. Godin et.al.[50] have shown that the kinetics of formation of self-assembled monolayers on gold-coated cantilevers and the resulting structure are dependent on the structure of the gold grain itself and also the rate at which the SAM reaches the surface. They showed a surface stress value on the order of 0.5 to 15 N/m. However, all these studies are based on a microscale domain. The application of the sensing technique on a macroscale domain would require a different instrumentation than the AFM cantilever. One such method is a curvature interferometry technique. In chapter 7 of this dissertation, we have reported the use of a high-resolution curvature interferometry

technique (Wang et al.[54]) to demonstrate the detection of surface stress generation during the formation of an alkanethiol self-assembled monolayer on a macroscale domain.

1.1.2 Biological macromolecules

Biological macromolecules are defined as large molecules which constitute of smaller organic molecules. There are four types – carbohydrates, lipids, proteins and nucleic acids. Since the work in this dissertation will focus on proteins and lipids, these are described in more detail below.

Proteins

Proteins are large organic compounds made of linear chains of amino acids formed by peptide bonds between the carboxylic group and the amino groups of adjacent amino acid residues. The chemical structure of an amino acid is shown in Figure 4(a). Proteins are essential parts of all organisms and are integral part of many cellular processes. They are involved in many functions in the body such as enzymes for chemical reactions, cell signaling, structural and mechanical scaffold and as storage proteins. Primary protein structure is a sequence of chain of amino acids but often the proteins fold into 3-dimensional structures with different spatial conformations. This is made possible by hydrogen bonding, van der waals interactions and ionic interactions between the substituted amino acid residues. A typical 3-dimensional coil structure of a protein molecule is shown in Figure 4(b).

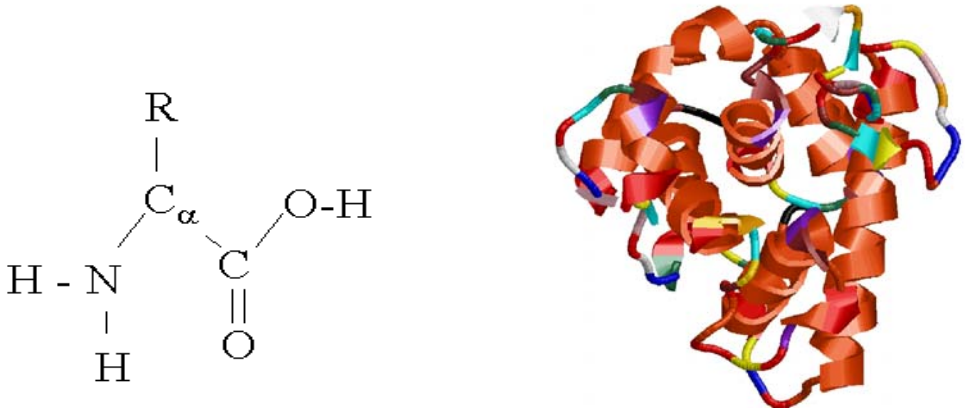

(a) (b)

Figure 4: (a) Chemical structure of an amino acid (Source: http://en.wikipedia.org/wiki/Protein_structure) and (b) 3-dimensional structure of a protein molecule (Source: www.dsimb.inserm.fr)

Lipids

Lipids are a class of biological macromolecules which are water-insoluble or lipophilic in nature. Triglycerides are most common type of fat (a type of lipid) and it makes up for about 95% of the lipids in our bodies. All triglycerides have a similar basic structure as shown in Figure 5 with three fatty acid units and one glycerol unit.

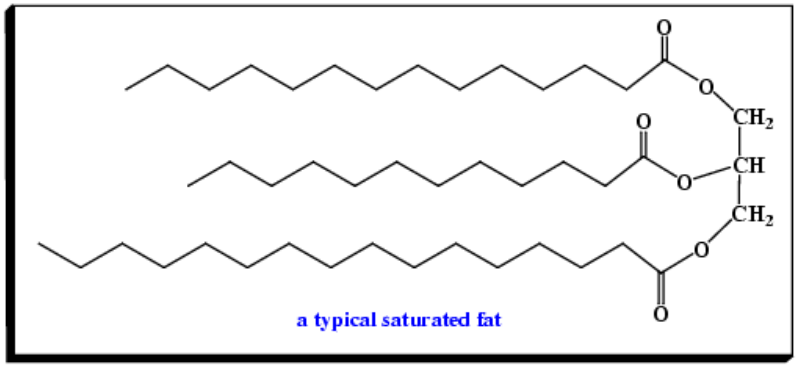

Figure 5: Chemical structure of an saturated fat (Source: http://scholar.hw.ac.uk/site/chemistry/graphics/saturfat.gif)

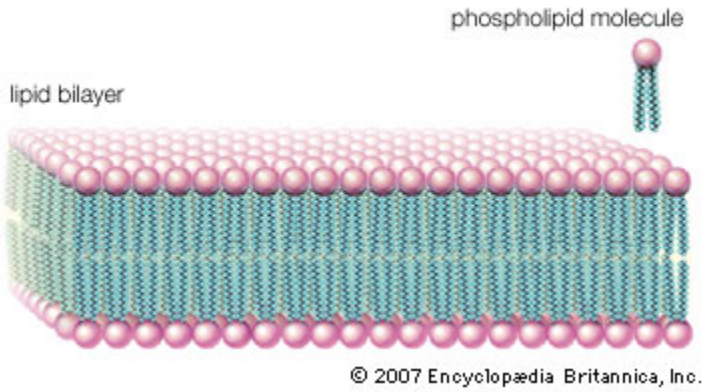

Figure 6: Structure of a phospholipid bilayer (Source: www.britannica.com)

Lipids are mainly used as energy storage sources in our body. They also serve other purposes such as structural components of cell membranes and in cell signaling. More complex lipids are phospholipids, glycolipids and cholesterol and they are present in cellular membranes. As lipids are amphiphilic molecules, consisting of a polar head group and non-polar fatty acid tail, they form bilayers in cellular membranes with the hydrocarbon tails facing one another to form a core and the head group facing the aqueous solutions. An example of a phospholipid molecule and its bilayer is shown in Figure 6.

1.2 Tribology

The field of *tribology* is concerned with the study of two interacting surfaces in relative motion with each other and encompasses the following broad fields - friction, lubrication and wear. The concept of friction and lubrication has been existent since the invention of the wheel. The idea that the friction of rolling resistance is less than that associated with kinetic friction led to the invention of the wheel. It is believed that ancient Egyptians used lubricants of some sort while sliding huge statues of pharaohs on wooden

sledges. After the industrial revolution, tribology became very essential for the modern machinery which used sliding and rolling surfaces. The purpose of the study of tribology became the reduction and if possible, the elimination of the sources of friction and wear at every level of modern technology.

Any engineering surface has an apparent area of contact and roughness associated with it at all length scales. Hence, when two engineering surfaces come into contact, the contact occurs at discrete points called asperities as shown in Figure 7. The sum of all those individual areas of contacts will constitute the real area of contact. In order to study the tribological properties of interacting surfaces at small length scales, the fields of micro/nanoscale tribology emerged. An instrument capable of studying the tribological interface contacting at multiple asperities and with a contact area of a few square microns is the microtribometer. An instrument that can simulate a single asperity contact and a contact area of a few square nanometers is the atomic force microscope (AFM).

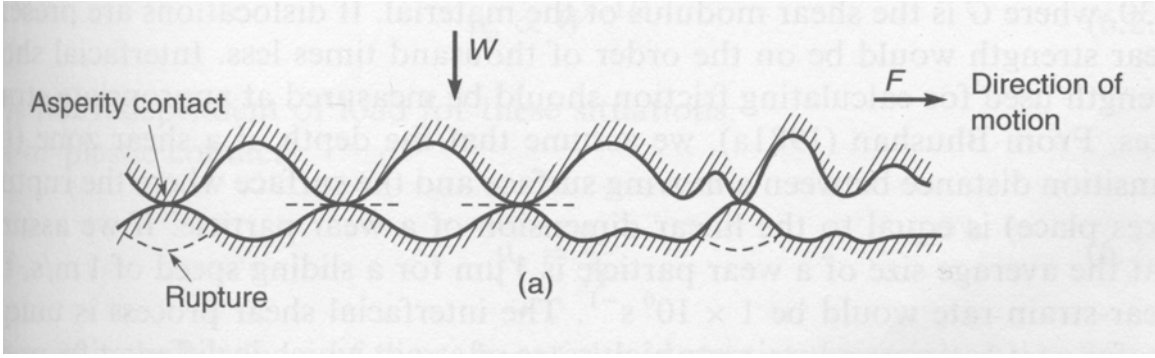

Figure 7: Two engineering surfaces comes into contact at discrete points called asperities (Source: [55]B. Bhushan, Principles and applications of tribology, 1999, John Wiley & Sons, NY)

Experimental techniques using these instruments were the primary mode of data gathering in this dissertation and are explained in depth in the next chapter.

1.2.1 Tribology of Total joint replacements

Total joint replacement (TJR) is a surgical procedure in which certain parts of an arthritic or damaged joint, such as a hip or knee joint, are removed and replaced with a plastic or metal device called prosthesis. The prosthesis is designed to enable the artificial joint to move just like normal, healthy joint. It can be performed on any joints of the body including the hip, knee, ankle, foot, shoulder, elbow, wrist, and fingers. Of these procedures, the hip and knee total joint replacements are by far the most common. A typical hip joint prosthesis is shown in Figure 8.

Figure 8: A typical hip implant – hip socket with the plastic cup, femoral head (oxinium, ceramic or cobalt chrome) and the hip stem (Source: http://www.designfax.net/archives/0503/0503app_ideas.asp)

TJRs can become loose and require a revision surgery due to several reasons such as mechanical failures (fracture), surgical problems (misalignment, contamination) and friction and wear of contacting surfaces resulting in aseptic loosening. Of all these reasons, it has been recognized that tribology (wear) is the major cause of long term failure of joint replacements. Specifically, the tribological issues, friction and wear at interface between the femoral head (usually a hard metal alloy) and acetabular cup lining (usually a soft polymer) and the fretting corrosion at the interface between the head and stem.

Many different material pairs have been used for TJRs but the combination of ceramic or metal with the polymer, ultra-high molecular weight polyethylene (UHMWPE) has proved to be extremely successful, giving low friction, low wear rates of the UHMWPE and smaller amount of wear debris, which could be tolerated by the body. Although UHMWPE has a wear rate lower than many other materials, the average lifetime of artificial hip joints incorporating the polymer are only 15-20 years. Considerable amount of research is being devoted to increasing the wear life of the prosthesis.

The human joint operates in the presence of a physiological fluid known as the synovial fluid. The natural lubricant, called synovial fluid, is a clear, viscous fluid which serves three purposes: it lubricates the articulating surfaces, carries nutrients to the cartilage cells, or chondrocytes, and transports waste products away from the cartilage. A diagram of a simplified synovial joint is shown in Figure 9.

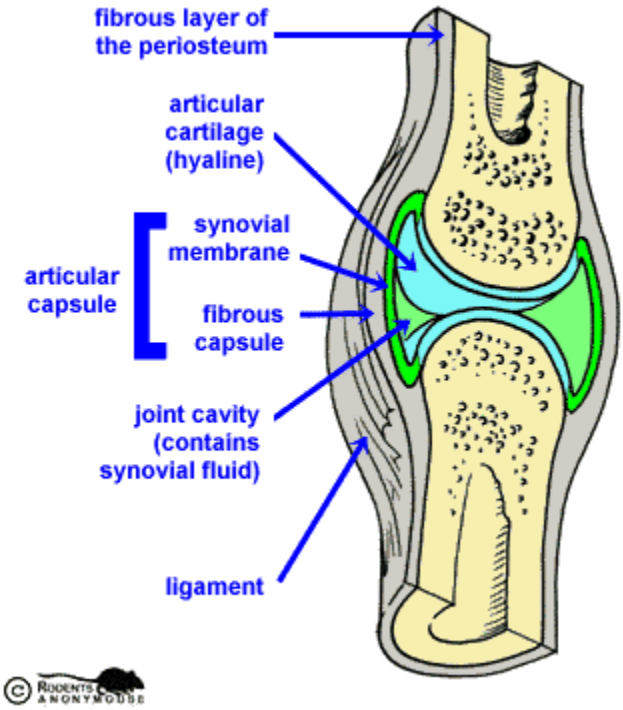

Figure 9: Schematic of a synovial joint (Source: http://www.zoology.ubc.ca/~biomania/tutorial/bonejt/jt01ac01.htm)

The synovial fluid contains various kinds of serum proteins, hyaluronic acid (HA) and also various kinds of lipids.[56] It is generally believed that the synovial fluid acts as a boundary lubricant to the joint interface and helps to minimize friction and wear. It has been found that albumin constitutes to almost 60% of the total protein concentration in serum and synovia.[56] As a result of numerous studies to identify an alternate physiological fluid for use in experiments *in-vitro*, ASTM (American society for testing and materials) has established that the use of bovine serum albumin is acceptable for TJR biomaterials testing. Several studies have attempted to elucidate the role of BSA in the tribology of the cup-head interface in TJRs.

Sawae et.al.[56] have studied the effect of two different synovial constituents (albumin and hyaluronic acid) on the friction and wear of UHMWPE using a pin-on disk apparatus and have shown that proteins affect the friction and wear quite drastically than the other constituents. Heuberger et.al.[57] and Widmer et.al.[58] have shown that rendering the polymeric surface more hydrophilic modifies the protein adsorption behavior of albumin and enhances the boundary lubrication behavior of bovine serum albumin. Though there are many studies on the tribological aspect of BSA on polymers using sophisticated joint simulators and tribometers, there are only a few which has realized the efficacy of atomic force microscopy to study the tribological behavior of bovine serum albumin on polymers. Park et.al.[59] have studied both macroscopic and microscopic (using AFM) friction measurements on bovine articular cartilages and shown that the microscale and macroscale friction coefficient exhibited no statistical differences and that AFM could be used to explore the role of boundary lubricants in cartilages and provide greater insight into design of biomaterials. Ho et.al.[60] have used atomic force microscopy to study the wear mechanism and eventual failure of UHMWPE insert in TJR prosthesis.

The other important component in the synovial fluid which researchers have shown to have a lubricating effect is the surface active phospholipids (SAPL). The SAPL, being an amphiphilic molecule, attaches to the hydrophilic UHMWPE surface and the hydrophobic fatty-acid tail sticks out to form a monolayer on the surface of UHMWPE, thus changing the interfacial properties. The most abundant SAPL in the body is the dipalmitoyl phosphatidylcholine (DPPC).[61] Jones et al.[62] have shown that DPPC dissolved in propylene glycol showed a lower friction response on sheep joints than just propylene glycol. Also,

ethanol dissolved DPPC has shown a similar friction response on UHMWPE than regular saline lubricants.[63]

Another factor affecting the tribological performance of UHMWPE in implants is its processing. Medical grade UHMWPE stock material may undergo a variety of processing techniques during implant manufacturing,[64] including molding, extrusion and milling or turning. These manufacturing processes can affect the surface morphology and mechanical properties of the polymer,[65, 66] which in turn can affect its friction and wear performance.

In chapters 4, 5 and 6, the effect of processing of UHMWPE and their effects on protein and lipid adsorption are discussed in terms of the friction and wear performance of the material interface.

1.2.2 Active tribological control

Researchers have devoted large amounts of effort in developing strategies to minimize friction and wear from macroscale down to nanoscale applications. In macroscale applications, mineral and synthetic lubricants are designed using specific molecular structures of the lubricants to vary their pressure-viscosity, temperature-viscosity characteristics;[67, 68] formulations of additives in lubricating fluids are also used to minimize friction and wear.[69, 70] For micro/nanoscale systems, the use of self-assembled monolayers (SAMs) as solid-like boundary lubricants has proven to be an effective lubrication scheme.[71-75] However, with the current development of technology, a stricter requirement of controlling tribological phenomena at desired levels is arising in various engineering practices and especially in micro/nanoscale systems. Control in tribology has traditionally involved “passive” strategies such as sophisticated formulation of additives in lubricating

fluids and complex composite formations of interface materials. In such systems, the tribological elements respond to specific operating conditions in a manner which is predetermined by their given properties. A more powerful means of tribological control involves "active" strategies characterized by the feature that, by externally supplying energy, the tribological response of a system is altered as desired. An example of a macroscale system that employs such a scheme is the anti-lock brake system which automatically controls the braking torque on each wheel to establish an appropriate slide-to-roll ratio so that maximum deceleration and sufficient cornering force are maintained at the tire-road interface. Examples of micro/nanoscale applications that may utilize a system with "high" and "low" friction states include release mechanisms for stiction problems, locking mechanisms in defense applications and consumer applications. The ability to thus *actively* control and modulate the tribological properties of an interface is a subject of great interest to systems of all scales, particularly to micro/nanoscale systems. Although some studies to active achieve friction and wear control of an interface have been performed on the macroscale, studies on the micro/nanoscale appear to be surprisingly lacking. In chapter 8 of this dissertation, we report the active tribological control of a low density alkanethiol SAM (LD-SAM) system in the presence of an external electric field. The switchability of the LD-SAM system in the presence of an electric field[76] as shown in Figure 10 has been exploited to be used as active friction switch.

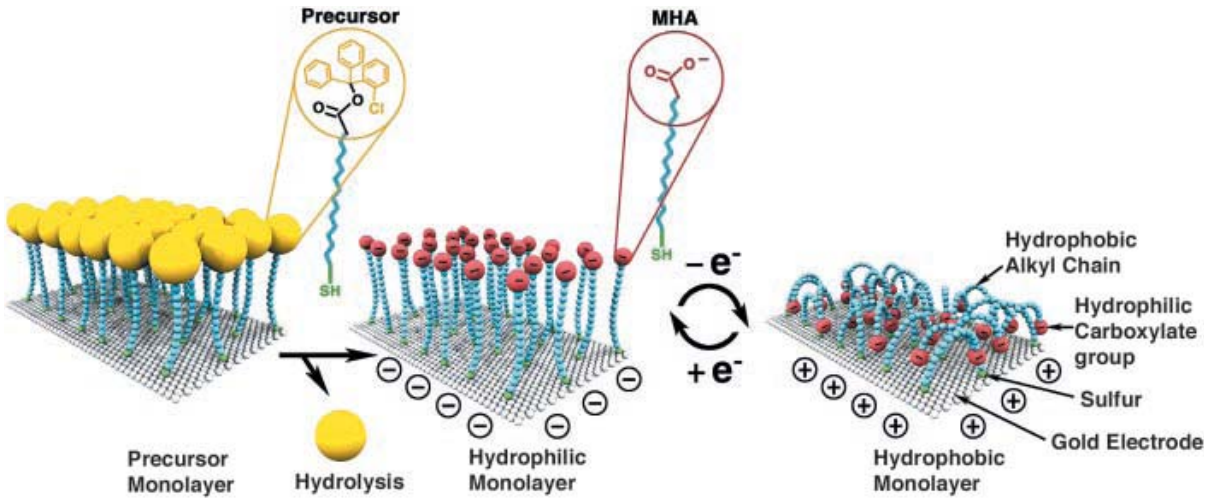

Figure 10: LD-SAM showing the switching behavior in the presence of an electric field (Source: Lahann et al[76])

1.3 Motivation and research objectives

It is quite clear that thin organic films play a critical role in the performance of several engineering applications including total joint replacements (as surface films affecting friction and wear of the implants) and in microscale systems (as a sensing or lubricative thin film). These two specific applications have broad technological and social impact. Miniaturized sensors and devices have widespread applications in defense, medical and consumer applications. Improving the durability of total joint replacements positively impact our society from an economic stand point as well. Improved durability and reliability of the joint can reduce the need for revision surgeries associated with TJRs which costs about 3-4 times than a primary knee implant.

With this in mind, the research objectives of this dissertation are the following:

1. Investigate friction behavior at the nanoscale and microscale as measured using atomic force microscopy and tribometer respectively and understand the phenomenon of contact area dependency of friction.
2. Understand the role of adsorbed protein and lipid films on the friction and wear behavior of polymeric surfaces in total joint replacements.
3. Understand mechanisms of surface stress generation during thin film (self assembled monolayer) formation in the context of sensing systems.
4. Investigate strategies to realize thin films (self assembled monolayers) with the ability to actively modulate the friction properties on demand for applications in microscale systems.

1.4 Dissertation organization

Figure 11 shows an outline of the research efforts and the chapters into which they are organized in this dissertation.

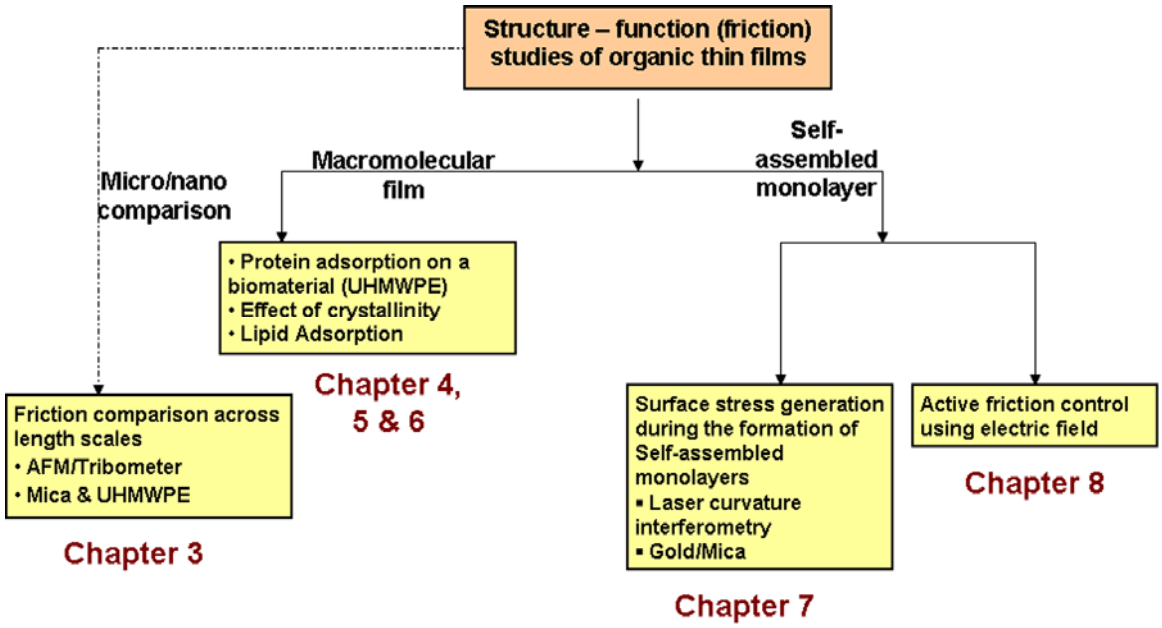

Figure 11: Outline of research efforts

Following this introductory chapter, chapter 2 describes the major experimental techniques used in the research. In chapter 3, the comparison of friction response across two length scales is reported on two material pairs – Si_3N_4/mica and Si_3N_4/UHMWPE. Chapter 4 reports the effect of material processing and protein adsorption on the tribological properties of UHMWPE. In chapter 5, the effect of crystallinity on the tribological behavior of UHMWPE is discussed. The combined effect of crystallinity and lipid adsorption on the frictional and wear behavior of UHMWPE is reported in chapter 6.

Surface stress generation due to formation of self-assembled monolayers on a macroscale domain is reported in Chapter 7. In chapter 8, we report the active friction control of a low-density alkanethiol SAM system in the presence of an external stimulus, electric field.

References

1. Maex, K.; Baklanov, M. R.; Shamiryan, D.; Iacopi, F.; Brongersma, S. H.; Yanovitskaya, Z. S., Low dielectric constant materials for microelectronics. *Journal of Applied Physics* **2003,** 93, (11), 8793-8841.

2. Opila, R. L.; Eng, J., Thin films and interfaces in microelectronics: composition and chemistry as function of depth. *Progress in Surface Science* **2002,** 69, (4-6), 125-163.

3. Maier, G., Low dielectric constant polymers for microelectronics. *Progress in Polymer Science* **2001,** 26, (1), 3-65.

4. Murarka, S. P., Silicide thin-films and their applications in microelectronics. *Intermetallics* **1995,** 3, (3), 173-186.

5. Frumar, M.; Frumarova, B.; Nemec, P.; Wagner, T.; Jedelsky, J.; Hrdlicka, M., Thin chalcogenide films prepared by pulsed laser deposition - new amorphous materials applicable in optoelectronics and chemical sensors. *Journal of Non-Crystalline Solids* **2006,** 352, (6-7), 544-561.

6. Komatsu, K.; Nanjo, H.; Yamagishi, Y.; Kaino, T., Oriented thin film fabrication of organic non-linear optical crystals. *Thin Solid Films* **2001,** 393, (1-2), 1-6.

7. Plucinski, K. J.; Makowska-Janusik, M.; Mefleh, A.; Kityk, I. V.; Yushanin, V. G., SiON films deposited on Si(111) substrates - new promising materials for nonlinear optics. *Materials Science and Engineering B-Solid State Materials for Advanced Technology* **1999,** 64, (2), 88-98.

8. Gauvin, S.; Zyss, J., Growth of organic crystalline thin films, their optical characterization and application to non-linear optics. *Journal of Crystal Growth* **1996,** 166, (1-4), 507-527.

9. Xu, J. P.; Lin, Y. B.; Lu, Z. H.; Liu, X. C.; Lu, Z. L.; Wang, J. F.; Zou, W. Q.; Lv, L. Y.; Zhang, F. M.; Du, Y. W., Enhanced ferromagnetism in Mn-doped TiO2 films during the structural phase transition. *Solid State Communications* **2006,** 140, (11-12), 514-518.

10. Lin, Y. H.; Zhao, R. J.; Nan, C. W.; Ying, M. H.; Kobayashi, M.; Ooki, Y.; Fujimori, A., Enhancement of ferromagnetic properties of NiO : Fe thin film by Li doping. *Applied Physics Letters* **2006,** 89, (20).

11. Gupta, N.; Verma, A.; Kashyap, S. C.; Dube, D. C., Microstructural, dielectric and magnetic behavior of spin-deposited nanocrystalline nickel-zinc ferrite thin films for microwave applications. *Journal of Magnetism and Magnetic Materials* **2007,** 308, (1), 137-142.

12. Wan, J. G.; Wang, X. W.; Wu, Y. J.; Zeng, M.; Wang, Y.; Jiang, H.; Zhou, W. Q.; Wang, G. H.; Liu, J. M., Magnetoelectric CoFe2O4-Pb(Zr,Ti)O-3 composite thin films derived by a sol-gel process. *Applied Physics Letters* **2005,** 86, (12).

13. Sinha, S. K.; Kawaguchi, M.; Kato, T.; Kennedy, F. E., Wear durability studies of ultra-thin perfluoropolyether lubricant on magnetic hard disks. *Tribology International* **2003,** 36, (4-6), 217-225.

14. Sundararajan, S.; Bhushan, B., Micro/nanotribology of ultra-thin hard amorphous carbon coatings using atomic force friction force microscopy. *Wear* **1999,** 229, 678-689.

15. Gupta, B. K.; Bhushan, B., Mechanical and tribological properties of hard carbon coatings for magnetic recording heads. *Wear* **1995,** 190, (1), 110-122.

16. Bhushan, B.; Gupta, B. K.; Azarian, M. H., Nanoindentation, microscratch, friction and wear studies of coatings for contact recording applications. *Wear* **1995,** 181, 743-758.

17. Bhushan, B.; Ruan, J. A., Atomic-scale friction measurements using friction force microscopy .2. Application to magnetic media. *Journal of Tribology-Transactions of the Asme* **1994,** 116, (2), 389-396.

18. Lu, C.; Dimov, S. S.; Lipson, R. H., Poly(vinyl pyrrolidone)-assisted sol - Gel deposition of quality beta-Barium borate thin films for photonics applications. *Chemistry of Materials* **2007,** 19, (20), 5018-5022.

19. Cravino, A.; Moggio, I.; Dell'Erba, C.; Comoretto, D.; Cuniberti, C.; Dellepiane, G.; Giorgetti, E.; Grando, D.; Margheri, M.; Sottini, S., Films of a novel polydiacetylene for photonics studies. *Synthetic Metals* **2000,** 115, (1-3), 275-277.

20. Sakaguchi, H.; Iwata, F.; Hirai, A.; Sasaki, A.; Nagamura, T., Nanometer-scale photoelectric property of organic thin films investigated by a photoconductive atomic force microscope. *Japanese Journal of Applied Physics Part 1-Regular Papers Short Notes & Review Papers* **1999,** 38, (6B), 3908-3911.

21. Dalton, L. R.; Harper, A. W.; Ghosn, R.; Steier, W. H.; Ziari, M.; Fetterman, H.; Shi, Y.; Mustacich, R. V.; Jen, A. K. Y.; Shea, K. J., Synthesis and processing of improved organic 2nd-order nonlinear-optical materials for applications in photonics. *Chemistry of Materials* **1995,** 7, (6), 1060-1081.

22. Khan, R. U. A.; Kwon, O. P.; Tapponnier, A.; Rashid, A. N.; Gunter, P., Supramolecular ordered organic thin films for nonlinear optical and optoelectronic applications. *Advanced Functional Materials* **2006,** 16, (2), 180-188.

23. Rashid, A. N.; Gunter, P., Self-assembled organic supramolecular thin films for nonlinear optics. *Organic Electronics* **2004,** 5, (1-3), 147-155.

24. van der Boom, M. E.; Zhu, P. W.; Evmenenko, G.; Malinsky, J. E.; Lin, W. B.; Dutta, P.; Marks, T. J., DNanoscale consecutive self-assembly of thin-film molecular materials for electrooptic switching. Chemical streamlining and ultrahigh response chromophores. *Langmuir* **2002,** 18, (9), 3704-3707.

25. Facchetti, A.; Mushrush, M.; Yoon, M. H.; Hutchison, G. R.; Ratner, M. A.; Marks, T. J., Building blocks for n-type molecular and polymeric electronics. Perfluoroalkyl-versus alkyl-functionalized oligothiophenes (nT; n=2-6). Systematics of thin film microstructure, semiconductor performance, and modeling of majority charge injection in field-effect transistors. *Journal of the American Chemical Society* **2004,** 126, (42), 13859-13874.

26. Witte, G.; Woll, C., Growth of aromatic molecules on solid substrates for applications in organic electronics. *Journal of Materials Research* **2004,** 19, (7), 1889-1916.

27. Stapleton, J. J.; Harder, P.; Daniel, T. A.; Reinard, M. D.; Yao, Y. X.; Price, D. W.; Tour, J. M.; Allara, D. L., Self-assembled oligo(phenylene-ethynylene) molecular electronic switch monolayers on gold: Structures and chemical stability. *Langmuir* **2003,** 19, (20), 8245-8255.

28. Dimitrakopoulos, C. D.; Malenfant, P. R. L., Organic thin film transistors for large area electronics. *Advanced Materials* **2002,** 14, (2), 99-+.

29. He, Y.; Fujikawa, Y.; Zhang, H.; Fukuzawa, K.; Mitsuya, Y., Evaluations of tribological characteristics of PFPE lubricants on DLC surfaces of magnetic disks. *Tribology Letters* **2007,** 27, (1), 1-11.

30. Kasai, P. H.; Raman, V., Z-dol versus Z-tetraol: Bonding and durability in magnetic hard disk application. *Tribology Letters* **2004,** 16, (1-2), 29-36.

31. Zhang, Q.; Archer, L. A., Boundary lubrication and surface mobility of mixed alkylsilane self-assembled monolayers. *Journal of Physical Chemistry B* **2003,** 107, (47), 13123-13132.

32. Jhon, M. S.; Choi, H. J., Lubricants in future data storage technology. *Journal of Industrial and Engineering Chemistry* **2001,** 7, (5), 263-275.

33. Tsukruk, V. V., Molecular lubricants and glues for micro- and nanodevices. *Advanced Materials* **2001,** 13, (2), 95-108.

34. Zhu, X. Y.; Houston, J. E., Molecular lubricants for silicon-based microelectromechanical systems (MEMS): a novel assembly strategy. *Tribology Letters* **1999,** 7, (2-3), 87-90.

35. Seto, J.; Asai, N.; Fujiwara, I.; Ishibashi, T.; Kamei, T.; Tamura, S., Functional organic ultra-thin films for device applications. *Thin Solid Films* **1996,** 273, (1-2), 97-104.

36. Thundat, T.; Warmack, R. J.; Chen, G. Y.; Allison, D. P., Thermal and ambient-induced deflections of scanning force microscope cantilevers. *Applied Physics Letters* **1994,** 64, (21), 2894-2896.

37. Zhang, Y. F.; Ji, H. F.; Snow, D.; Sterling, R.; Brown, G. M., A pH sensor based on a microcantilever coated with intelligent hydrogel. *Instrumentation Science & Technology* **2004,** 32, (4), 361-369.

38. Hilt, J. Z.; Gupta, A. K.; Bashir, R.; Peppas, N. A., Ultrasensitive biomems sensors based on microcantilevers patterned with environmentally responsive hydrogels. *Biomedical Microdevices* **2003,** 5, (3), 177-184.

39. Bashir, R.; Hilt, J. Z.; Elibol, O.; Gupta, A.; Peppas, N. A., Micromechanical cantilever as an ultrasensitive pH microsensor. *Applied Physics Letters* **2002,** 81, (16), 3091-3093.

40. Fritz, J.; Baller, M. K.; Lang, H. P.; Strunz, T.; Meyer, E.; Guntherodt, H. J.; Delamarche, E.; Gerber, C.; Gimzewski, J. K., Stress at the solid-liquid interface of self-assembled monolayers on gold investigated with a nanomechanical sensor. *Langmuir* **2000,** 16, (25), 9694-9696.

41. Lee, J.; King, W. P., Microcantilever hotplates: Design, fabrication, and characterization. *Sensors and Actuators a-Physical* **2007,** 136, (1), 291-298.

42. Mertens, J.; Finot, E.; Thundat, T.; Fabre, A.; Nadal, M. H.; Eyraud, V.; Bourillot, E., Effects of temperature and pressure on microcantilever resonance response. *Ultramicroscopy* **2003,** 97, (1-4), 119-126.

43. Barnes, J. R.; Stephenson, R. J.; Woodburn, C. N.; Oshea, S. J.; Welland, M. E.; Rayment, T.; Gimzewski, J. K.; Gerber, C., A femtojoule calorimeter using micromechanical sensors. *Review of Scientific Instruments* **1994,** 65, (12), 3793-3798.

44. Gimzewski, J. K.; Gerber, C.; Meyer, E.; Schlittler, R. R., Observation of a chemical-reaction using a micromechanical sensor. *Chemical Physics Letters* **1994,** 217, (5-6), 589-594.

45. Ganesan, P. G.; Wang, X.; Nalamasu, O., Method for sensing the self-assembly of polyelectrolyte monolayers using scanning probe microscope cantilever. *Applied Physics Letters* **2006,** 89, (21).

46. Hosaka, S.; Chiyoma, T.; Ikeuchi, A.; Okano, H.; Sone, H.; Izumi, T., Possibility of a femtogram mass biosensor using a self-sensing cantilever. *Current Applied Physics* **2006,** 6, (3), 384-388.

47. Ilic, B.; Craighead, H. G.; Krylov, S.; Senaratne, W.; Ober, C.; Neuzil, P., Attogram detection using nanoelectromechanical oscillators. *Journal of Applied Physics* **2004,** 95, (7), 3694-3703.

48. Gupta, A.; Akin, D.; Bashir, R., Single virus particle mass detection using microresonators with nanoscale thickness. *Applied Physics Letters* **2004,** 84, (11), 1976-1978.

49. Berger, R.; Delamarche, E.; Lang, H. P.; Gerber, C.; Gimzewski, J. K.; Meyer, E.; Guntherodt, H. J., Surface stress in the self-assembly of alkanethiols on gold. *Science* **1997,** 276, (5321), 2021-2024.

50. Godin, M.; Williams, P. J.; Tabard-Cossa, V.; Laroche, O.; Beaulieu, L. Y.; Lennox, R. B.; Grutter, P., Surface stress, kinetics, and structure of alkanethiol self-assembled monolayers. *Langmuir* **2004,** 20, (17), 7090-7096.

51. Kohale, S.; Molina, S. M.; Weeks, B. L.; Khare, R.; Hope-Weeks, L. J., Monitoring the formation of self-assembled monolayers of alkanedithiols using a micromechanical cantilever sensor. *Langmuir* **2007,** 23, (3), 1258-1263.

52. Rogers, B.; Manning, L.; Jones, M.; Sulchek, T.; Murray, K.; Beneschott, B.; Adams, J. D.; Hu, Z.; Thundat, T.; Cavazos, H.; Minne, S. C., Mercury vapor detection with a self-sensing, resonating piezoelectric cantilever. *Review of Scientific Instruments* **2003,** 74, (11), 4899-4901.

53. Fritz, J.; Baller, M. K.; Lang, H. P.; Rothuizen, H.; Vettiger, P.; Meyer, E.; Guntherodt, H. J.; Gerber, C.; Gimzewski, J. K., Translating biomolecular recognition into nanomechanics. *Science* **2000,** 288, (5464), 316-318.

54. Wang, J.; Shrotriya, P.; Kim, K. S., Surface residual stress measurement using curvature interferometry. *Experimental Mechanics* **2006,** 46, (1), 39-46.

55. Bhushan, B., *Principles and applications of tribology*. John Wiley & Sons: New York, 1999.

56. Sawae, Y.; Murakami, T.; Chen, J., Effect of synovia constituents on friction and wear of ultra-high molecular weight polyethylene sliding against prosthetic joint materials. *Wear* **1998,** 216, (2), 213-219.

57. Heuberger, M. P.; Widmer, M. R.; Zobeley, E.; Glockshuber, R.; Spencer, N. D., Protein-mediated boundary lubrication in arthroplasty. *Biomaterials* **2005,** 26, (10), 1165-73.

58. Widmer, M. R.; Heuberger, M.; Voros, J.; Spencer, N. D., Influence of polymer surface chemistry on frictional properties under protein-lubrication conditions: implications for hip-implant design. *Tribology Letters* **2001,** 10, (1-2), 111-116.

59. Park, S.; Costa Kevin, D.; Ateshian Gerard, A., Microscale frictional response of bovine articular cartilage from atomic force microscopy. *Journal of biomechanics* **2004,** 37, (11), 1679-87.

60. Ho, S. P.; Carpick, R. W.; Boland, T.; LaBerge, M., Nanotribology of CoCr-UHMWPE TJR prosthesis using atomic force microscopy. *Wear* **2002,** 253, (11-12), 1145-1155.

61. Ozturk, H. E.; Stoffel, K. K.; Jones, C. F.; Stachowiak, G. W., The effect of surface-active phospholipids on the lubrication of osteoarthritic sheep knee joints: Friction. *Tribology Letters* **2004,** 16, (4), 283-289.

62. Jones, C. F.; Stoffel, K.; Ozturk, H. E.; Stachowiak, G. W., The effect of surface active phospholipids on the lubrication of osteoarthritic sheep knee joints: Wear. *Tribology Letters* **2004,** 16, (4), 291-296.

63. Gale, L. R.; Coller, R.; Hargreaves, D. J.; Hills, B. A.; Crawford, R., The role of SAPL as a boundary lubricant in prosthetic joints. *Tribology International* **2007,** 40, (4), 601-606.

64. Kurtz, S. M.; Muratoglu, O. K.; Evans, M.; Edidin, A. A., Advances in the processing, sterilization, and crosslinking of ultra-high molecular weight polyethylene for total joint arthroplasty. *Biomaterials* **1999,** 20, (18), 1659-1688.

65. Bellare, A.; Cohen, R. E., Morphology of rod stock and compression moulded sheets of ultra-high molecular-weight polyethylene used in orthopaedic implants. *Biomaterials* **1996,** 17, (24), 2325-2333.

66. Ho, S. P.; Riester, L.; Drews, M.; Boland, T.; LaBerge, M., Nanoindentation properties of compression-moulded ultra-high molecular weight polyethylene. *Proceedings of the Institution of Mechanical Engineers Part H-Journal of Engineering in Medicine* **2003,** 217, (H5), 357-366.

67. Sharma, S. K.; Rosado, L.; Hoglund, E.; Hamrock, B. J., Rheology of perfluoropolyalkylether fluids in elastohydrodynamic lubrication. *Tribology Transactions* **1995,** 38, (4), 769-780.

68. Gschwender, L. J.; Kramer, D. C.; Lok, B. K.; Sharma, S. K.; Snyder, C. E., Jr.; Sztenderowicz, M. L., Liquid Lubricants and Lubrication. In *Handbook of Modern Tribology*, Bhushan, B., Ed. CRC Press: New York, 2001; pp 361-383.

69. Tung, S. C.; Wang, S. S., Insitu electro-charging for friction reduction and wear resistant film formation. *Tribology Transactions* **1991,** 34, (4), 479-488.

70. Kapoor, A.; Tung, S. C.; Schwartz, S. E.; Dwyer-Joyce, R. S., Automotive Tribology. In *Handbook of Modern Tribology*, Bhushan, B., Ed. CRC Press: New York, 2001; pp 1187-1230.

71. Maboudian, R.; Carraro, C., Surface engineering for reliable operation of MEMS devices. *Journal of Adhesion Science and Technology* **2003,** 17, (4), 583-591.

72. Maboudian, R.; Ashurst, W. R.; Carraro, C., Self-assembled monolayers as anti-stiction coatings for MEMS: characteristics and recent developments. *Sensors and Actuators a-Physical* **2000,** 82, (1-3), 219-223.

73. Srinivasan, U.; Houston, M. R.; Howe, R. T.; Maboudian, R., Alkyltrichlorosilane-based self-assembled monolayer films for stiction reduction in silicon micromachines. *Journal of Microelectromechanical Systems* **1998,** 7, (2), 252-260.

74. Sundararajan, S.; Bhushan, B., Static friction and surface roughness studies of surface micromachined electrostatic micromotors using an atomic force/friction force microscope. *Journal of Vacuum Science & Technology a-Vacuum Surfaces and Films* **2001,** 19, (4), 1777-1785.

75. Kiely, J. D.; Houston, J. E.; Mulder, J. A.; Hsung, R. P.; Zhu, X. Y., Adhesion, deformation and friction for self-assembled monolayers on Au and Si surfaces. *Tribology Letters* **1999,** 7, (2-3), 103-107.

76. Lahann, J.; Mitragotri, S.; Tran, T. N.; Kaido, H.; Sundaram, J.; Choi, I. S.; Hoffer, S.; Somorjai, G. A.; Langer, R., A reversibly switching surface. *Science* **2003,** 299, (5605), 371-374.

CHAPTER 2. EXPERIMENTAL TECHNIQUES

Tribological characterization studies were performed primarily at the nanoscale and the microscale. At the nanoscale the atomic force microscope (AFM) was used to simulate a single asperity contact and study adhesion and friction behavior whereas at the microscale a ball-on-flat microtribometer was used. The instruments and associated measurement techniques are described below.

2.1 Atomic force microscope

To simulate the single asperity contact, we used an atomic force microscope (AFM). The AFM can measure very small forces between the probe and the surfaces with sub-nanometer resolution. The operating principle behind an AFM is shown in Figure 1.

A sharp cantilever/tip assembly is placed at the end of a piezo tube. The probe is scanned over the surface in a raster pattern. A laser beam is focused on the end of the cantilever during raster-scanning and is reflected onto a quadrant photodiode. A constant force on the sample is maintained by a feedback loop control system to compensate for the topographical features of the surface. This results in a three-dimensional map of the sample. The deflection signal for achieving topographical map is calculated as laser spot intensity for quadrants (A+B) – (C+D) as shown in Figure 1. When measuring friction, the cantilever is scanned perpendicular to the cantilever's axis, during which the tip will experience torsion and this will increase or decrease based on the frictional characteristics of the sample. Frictional signal is calculated as (A+C) – (B+D).

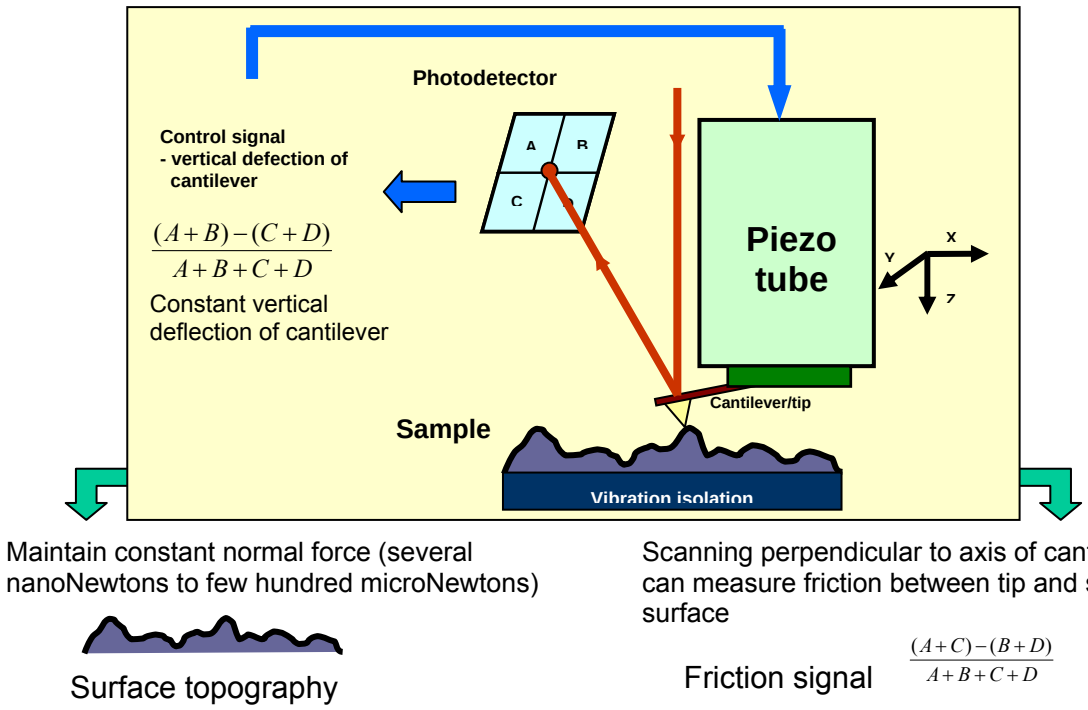

Figure 1: Operating principle of an atomic force microscope (AFM)

For any meaningful quantitative analysis of the friction signals obtained with an atomic force microscope, one has to accurately determine the normal force constant and the lateral calibration factor to convert the measured friction signal in volts to force units (nanonewtons). Also, for contact theories to be obtained for the friction measurements, the determination of the probe radius is essential.

2.1.1 Normal calibration

Normal calibration of cantilevers is an essential step in the quantitative analysis of friction between interfaces. Cantilevers are generally batch-manufactured by companies using microfabrication techniques and hence, the dimensions of the cantilevers in a particular batch vary quite a bit. The nominal force constant given by the manufacturer's quote will not

be true for all the cantilevers and sometimes, it might even be 100% off. There are several techniques available in literature for the normal calibration of cantilevers. The method we have followed in all our work is that of Torii et al.[1] In this method, firstly, the cantilever under test is placed over an infinitely hard sample, like sapphire, and the total cantilever deflection, δ_{tot}, is noted as the cantilever is in contact with the sample. Later, the test cantilever is placed into contact with the free end of a reference cantilever as shown in Figure 2, whose force constant is accurately known. After the deflection experienced on the reference cantilever, δ_{test}, is known, using the formula

$$k_{test} = \frac{k_{ref}(\delta_{tot} - \delta_{test})}{\delta_{test}\cos\theta} \tag{1}$$

the force constant of the test cantilever is accurately determined.

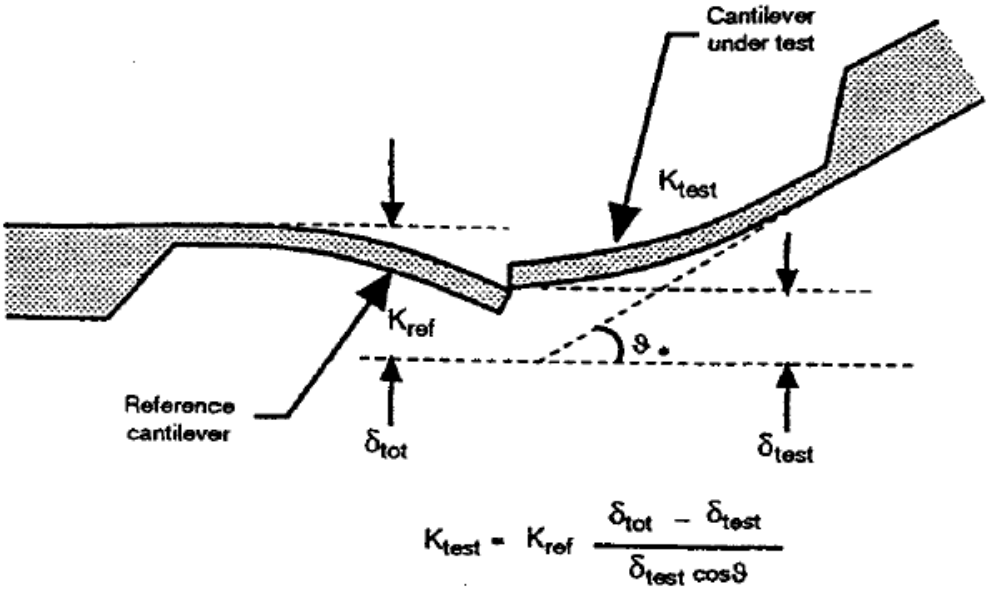

Figure 2: Schematic of the calibrated lever technique to measure the normal force constant of cantilevers (Source: Tortonese and Kirk [2])

2.1.2 Lateral Calibration

Considerable research has gone into the lateral calibration of cantilevers for quantitative friction force microscopy. One of the widely used lateral calibration technique is by Ruan and Bhushan.[3] We have used this technique in all our studies. A brief overview of the technique is given below.

The technique consists of two steps. In the first step, the tip scans parallel to the cantilever's long axis. The cantilever deflects due to topographic feature and also the friction between the probe and the surface. The frictional force, W_f, is given by

$$W_f = (\Delta W_1 + \Delta W_2) * L / 2l \tag{2}$$

where L is the cantilever length and l is the length of the tip. The coefficient of friction, μ, is given by

$$\mu = W_f / W_0 = (\Delta W_1 + \Delta W_2) L / W_0 (2l) \tag{3}$$

where W_0 is given by W_0 = *vertical deflection* H_0 * *normal spring constant k.* Figure 3 shows a typical plot used to obtain the coefficient of friction obtained from the first step. In this plot, the z center position and Height TMR are representations of ΔH_0 and (ΔH_1 + ΔH_2) respectively.

In the second step, the tip is scanned perpendicular to the long axis of the cantilever and traditional friction measurements is calculated at different normal loads and the slope of this plot (shown in Figure 4) is equated to the friction coefficient obtained in the first step. This will give a calibration factor in terms of nanonewtons per volt of lateral torsion.

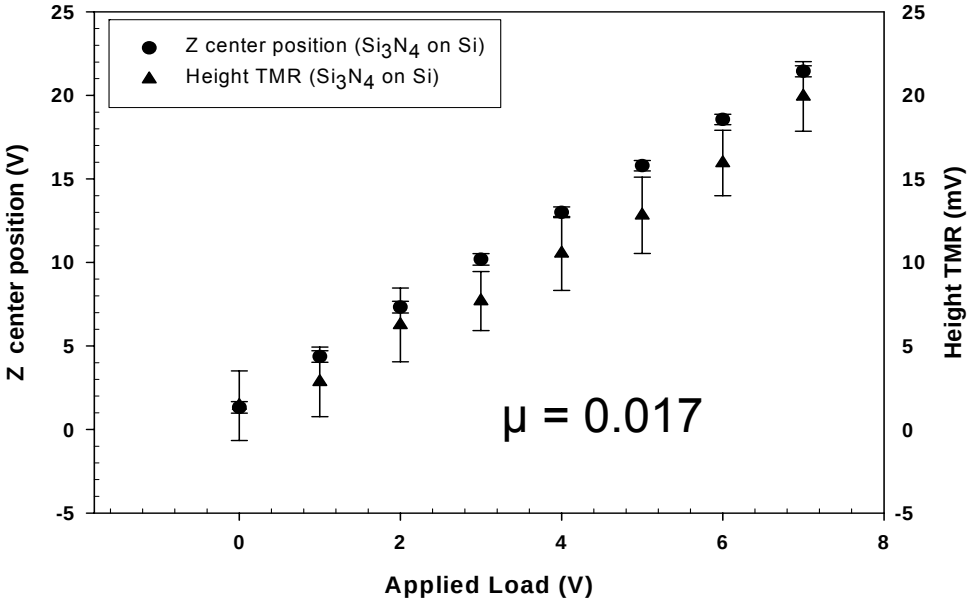

Figure 3: Variation of (Δ H1 + Δ H2) (represented by height TMR) and H0 (represented by z center position) as a function of applied load for a Si_3N_4 cantilever on Silicon.

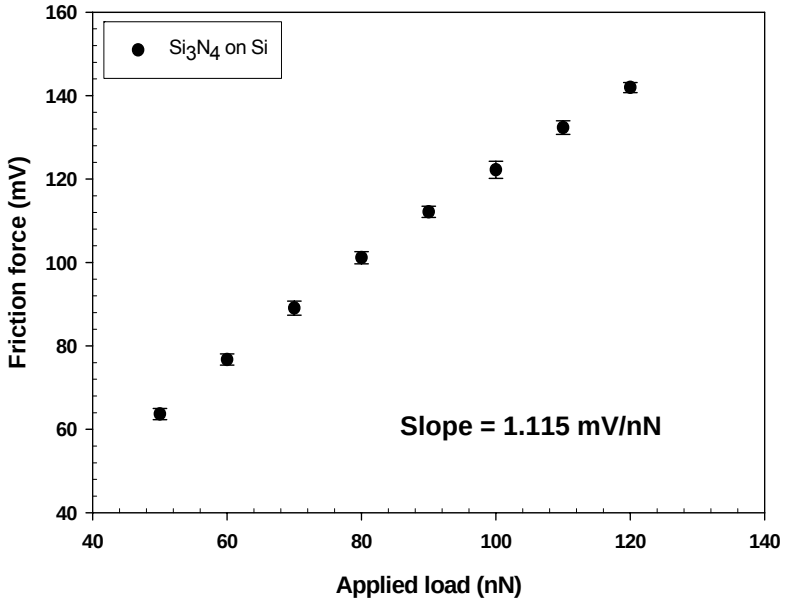

Figure 4: Variation of friction force (represented by friction TMR) as a function of applied load for a Si_3N_4 cantilever on Silicon.

2.1.3 Tip radius calculation

Contact mechanics theories require the determination of the real area of contact and the contact in the case of an atomic force microscope is determined by the radius of curvature of the probe. Manufacturers produce tips with radii ranging from a few nanometers to a few microns. The tip shape and radius can be determined with some precision using commercially available samples (TGT01 from MikroMasch, Portland, OR). The TGT01 has sharp silicon spiked features (radius < 10 nm) which is shown as an inset in Figure 5. When a probe with radius larger than 10 nm is scanned across the silicon spikes, the resulting image will be height maps containing information about the tip shape and radius. Deconvolution of these images using blind reconstruction methods results in fairly accurate estimate of the tip shape and the radius. A typical image of a probe is shown in Figure 5 and the parabolic fit to the probe is shown in Figure 6 which was generated by a custom written MATLAB code (Appendix A).

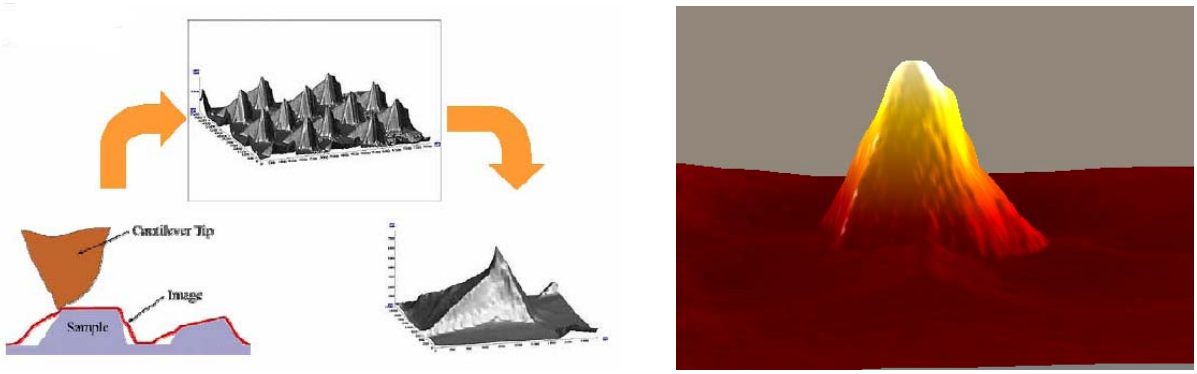

Figure 5: Schematic of reverse imaging of the probe when it scans over the silicon spiked features of a standard TGT01 sample (MikroMasch, Portland, OR). The image on the right shows a silicon nitride probe image generated using this technique.

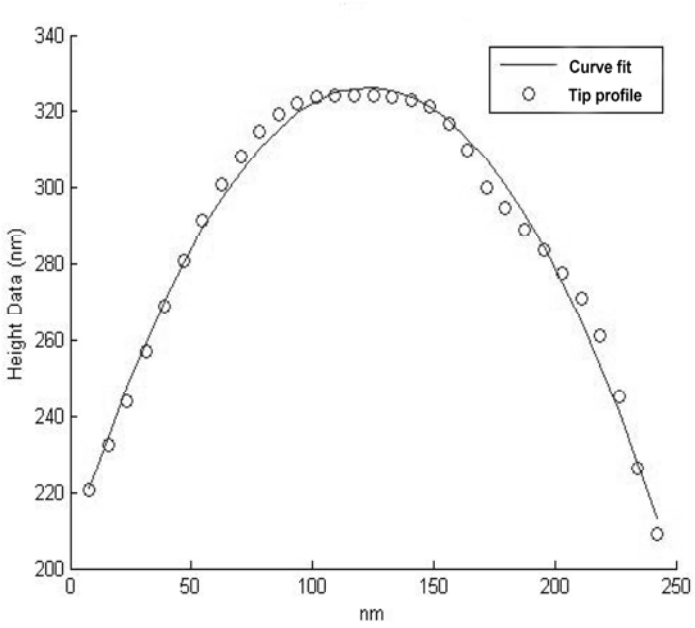

Figure 6: Parabolic fit to an AFM probe [4]

2.1.4 Contact mechanics theories

If externally applied loads are kept low, then the AFM tip forms a nanometer-sized single asperity contact with the surface being probed, and interaction forces can be measured without causing plastic deformation. According to Bowden and Tabor[5], in the absence of ploughing, the adhesive friction is directly proportional to the real area of contact and is given by

$$F = \tau A_r \quad (4)$$

where τ is the interfacial shear strength of the contact and A_r is the real area of contact. When the normal load is increased, the real area of contact increases as the surfaces deform elastically or plastically.

In the absence of adhesion, the Hertz model[6] can be used to describe the contact between two elastic spheres. However, at the small length scales, the adhesion between the

solid surfaces is not negligible and has to be included in the calculation for contact area. For compliant materials with strong adhesion forces, the contact area is described by Johnson-Kendall-Roberts (JKR)[7] theory and for stiff materials with weak adhesion forces, the contact area is described by Derjaguin-Muller-Toporov (DMT)[8] model. The intermediate regime (transition regime) between JKR and DMT is best described by Maugis-Dugdale (MD)[9] model. In order to find out which contact theory is to be used for the contact conditions in one's experiments, Tabor came up with a non-dimensional parameter called the Tabor's parameter which is given as

$$\chi = \left(\frac{16 R \gamma^2}{9 K^2 z_0^3} \right)^{1/3} \tag{5}$$

where R is the radius of the probe, γ is the work of adhesion, z_0 is the equilibrium spacing of the two surfaces (taken to be 0.2 nm[10]) and K is the composite elastic modulus given by

$$K = \frac{4}{3} \left[\frac{1 - \nu_1^2}{E_1} + \frac{1 - \nu_2^2}{E_2} \right]^{-1} \tag{6}$$

where $\nu_{1,2}$ and $E_{1,2}$ are the Poisson's ratio and elastic modulus of the tip and sample respectively. When χ is > 5, JKR theory applies and when χ < 0.1, the DMT theory applies.

JKR theory describes the contact area A as a function of load L which is given by

$$A = \frac{\pi R^{2/3}}{K^{2/3}} . [L + 3\pi R\gamma + \sqrt{6\pi R\gamma L + (3\pi R\gamma)^2}]^{2/3} \tag{7}$$

and the critical load (which is the load required to detach the surfaces even after the external load is removed) is given by

$$L_c = -\frac{3}{2}\pi R\gamma \tag{8}$$

DMT theory describes the contact area A as a function of load L which is given by

$$A = \frac{\pi R^{2/3}}{K^{2/3}}.[L + 2\pi R\gamma]^{2/3} \tag{9}$$

and the critical load is given by

$$L_c = -2\pi R\gamma \tag{10}$$

When χ is between 0.1 and 5, MD model applies. However, the MD model requires a very difficult analysis and provides only analytical solutions. Carpick et al.[11] came up with a generalized transition equation which is an approximation to MD model.

The other term in equation 4 is the interfacial shear strength, τ. Researchers have used several techniques to compute the shear strength, τ, of an AFM probe contact by utilizing different methods of interpreting the frictional data. Carpick et.al[12] described a simple method to determine the shear strength of a LFM tip-sample contact independent of contact mechanics-models, by measuring the lateral contact stiffness. Cain et.al [13] followed on the lines of Carpick et.al. [12] for the interpretation of frictional data and measured friction with colloidal spherical probes and the derivation of shear strength from those measurements. Some of the other works done in this area are as follows: Pietrement and Troyon [14] has used a combination of magnetic force microscopy and lateral force microscopy to determine the shear modulus and shear strength on high and low-density polyethylene. Carpick et.al. [15] employed a platinum probe on a mica surface, and using an extended JKR model, estimated the interfacial surface energies and shear strength. Major et.al.[16] studied the tribological properties of alkoxyl monolayers on oxide terminated silicon and using contact mechanics models, estimated the adhesion energy and interfacial shear strength of the self-assembled monolayers.

2.2 Microtribometer

To study the friction and wear of material interfaces at the microscale, a microtribometer was used in all our studies. The instrument used was a custom-built reciprocating microtribometer with a sub-millinewton resolution. A probe (Silicon nitride ball of ~ 1.2 mm) is placed at the end of crossed I-beam structure as shown in Figure 7. The normal and frictional (lateral) forces are monitored with the use of semiconductor strain gages mounted on the cantilevers. A schematic of the tribometer setup is shown in Figure 8. The sample is placed on a spacer block and it can be moved in a reciprocating manner with a two-axis stage controller. The vertical stage moves with the crossed I-beam structure onto the sample by which it applies different normal loads on the sample. The signals from the stain gages mounted on the cantilevers are amplified using a signal amplifier.

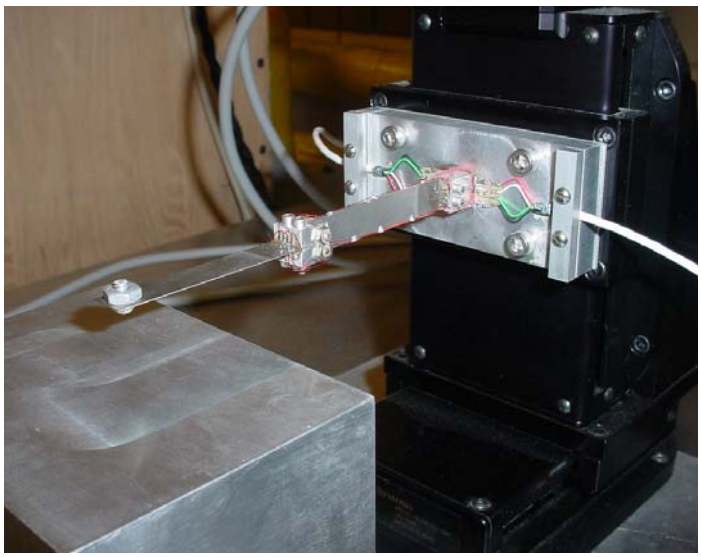

Figure 7: Crossed I-beam structure with the two cantilevers (normal and lateral) and strain gages mounted on them [17]

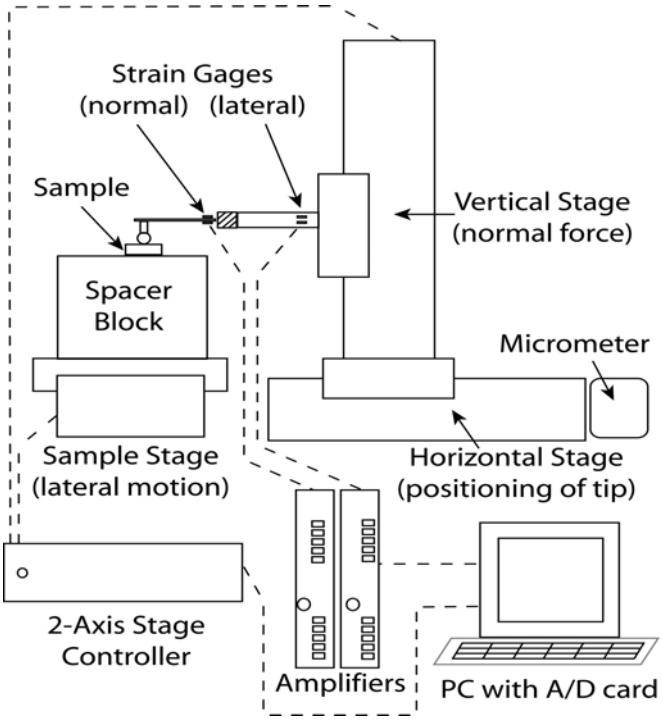

Figure 8: Schematic of the custom-built microtribometer system [18]

Researchers have reported friction response of material interfaces at the micro/nanoscale and have attributed a coefficient of friction or contact area dependence of friction with respect to the applied normal load. Before going into a detailed study of tribological properties of interfaces using the AFM or tribometer, one has to understand the friction mechanism and the effect of length scale on micro/nanoscale contacts. To that effect, in chapter 3 of this thesis, we have measured the friction response of a material pair at two different length scales and have analyzed the friction response in the context of contact area dependence and coefficient of friction.

References

1. Torii, A.; Sasaki, M.; Hane, K.; Okuma, S., A method for determining the spring constant of cantilevers for atomic force microscopy. *Measurement Science & Technology* **1996,** 7, (2), 179-184.

2. Tortonese, M.; Kirk, M., Characterization of application specific probes for SPMs. *Proceedings of SPIE-The International Society for Optical Engineering* **1997,** 3009, (Micromachining and Imaging), 53-60.

3. Ruan, J. A.; Bhushan, B., Atomic-Scale Friction Measurements Using Friction Force Microscopy .1. General-Principles and New Measurement Techniques. *Journal of Tribology-Transactions of the Asme* **1994,** 116, (2), 378-388.

4. Karuppiah, K. S. K.; Sundararajan, S.; Xu, Z. H.; Li, X. D., The effect of protein adsorption on the friction behavior of ultra-high molecular weight polyethylene. *Tribology Letters* **2006,** 22, (2), 181-188.

5. Bowden, F. P.; Tabor, D., *The Friction and Lubrication of Solids*. 1950.

6. Hertz, H., *Journal für die reine und angewandte Mathematik* **1882,** 92, 156-171.

7. Johnson, K. L.; Kendall, K.; Roberts, A. D., Surface Energy and Contact of Elastic Solids. *Proceedings of the Royal Society of London Series a-Mathematical and Physical Sciences* **1971,** 324, (1558), 301-&.

8. Derjaguin, B. V.; Muller, V. M.; Toporov, Y. P., Effect of Contact Deformations on Adhesion of Particles. *Journal of Colloid and Interface Science* **1975,** 53, (2), 314-326.

9. Maugis, D., Adhesion of Spheres - the Jkr-Dmt Transition Using a Dugdale Model. *Journal of Colloid and Interface Science* **1992,** 150, (1), 243-269.

10. Carpick, R. W.; Agrait, N.; Ogletree, D. F.; Salmeron, M., Variation of the interfacial shear strength and adhesion of a nanometer-sized contact. *Langmuir* **1996,** 12, (13), 3334-3340.

11. Carpick, R. W.; Ogletree, D. F.; Salmeron, M., A general equation for fitting contact area and friction vs load measurements. *Journal of Colloid and Interface Science* **1999,** 211, (2), 395-400.

12. Carpick, R. W.; Ogletree, D. F.; Salmeron, M., Lateral stiffness: A new nanomechanical measurement for the determination of shear strengths with friction force microscopy. *Applied Physics Letters* **1997,** 70, (12), 1548-1550.

13. Cain, R. G.; Biggs, S.; Page, N. W., Force calibration in lateral force microscopy. *Journal of Colloid and Interface Science* **2000,** 227, (1), 55-65.

14. Pietrement, O.; Troyon, M., Quantitative study of shear modulus and interfacial shear strength by combining modulated lateral force and magnetic force modulation microscopies. *Surface and Interface Analysis* **2001,** 31, (11), 1060-1067.

15. Carpick, R. W.; Agrait, N.; Ogletree, D. F.; Salmeron, M., Measurement of interfacial shear (friction) with an ultrahigh vacuum atomic force microscope. *Journal of Vacuum Science & Technology B* **1996,** 14, (2), 1289-1295.

16. Major, R. C.; Kim, H. I.; Houston, J. E.; Zhu, X. Y., Tribological properties of alkoxyl monolayers on oxide terminated silicon. *Tribology Letters* **2003,** 14, (4), 237-244.

17. Check, J. Design and construction of a microtribometer and its use in the study of the micro/nanotribological behavior of ultra-high molecular weight polyethylene (UHMWPE) Masters Thesis, Iowa State University, Ames, 2004.

18. Check, J.; Karuppiah, K. S. K.; Sundararajan, S., Comparison of the effect of surface roughness on the micro/nanotribological behavior of ultra-high-molecularweight polyethylene (UHMWPE) in air and bovine serum solution. *Journal of Biomedical Materials Research Part A* **2005,** 74A, (4), 687-695.

CHAPTER 3. EVALUATION OF FRICTION BEHAVIOR AND ITS CONTACT AREA DEPENDENCE AT THE MICRO AND NANOSCALES

Modified from a paper submitted to *Journal of Colloid and Interface Science*

K.S. Kanaga Karuppiah, Angela L. Bruck, Sriram Sundararajan

3.1 Introduction

According to Bowden and Tabor [1], friction force can be considered to be a sum of two different components: adhesive friction (F_{adh}) and deformation friction (F_{def}), as given by

$$F = F_{adh} + F_{def} \quad (1)$$

Adhesive friction arises from the contact and subsequent shearing of individual asperities and the deformation component arises due to the ploughing or other forms of deformation caused by the harder surface on the softer surface. In the absence of ploughing, the adhesive friction is directly proportional to the real area of contact and is given by

$$F = \tau A_r \quad (2)$$

where τ is the interfacial shear strength of the contact and A_r is the real area of contact. When the normal load is increased, the real area of contact increases as the surfaces deform elastically or plastically.

Macroscale friction studies typically define a coefficient of friction according to Amonton's law:

$$F = \mu N \quad (3)$$

where μ is the coefficient of friction and N is the normal load. This is because in the case of randomly rough surfaces, the real area of contact increases in direct proportion to the normal load and hence, Eq. 2 reduces to Amontons' law. We also note that once surface damage occurs, the friction force typically shows contact area independence.

With the advent of surface force apparatus (SFA)[2, 3] and the atomic force microscope (AFM) [4], researchers have been able investigate friction mechanisms at the asperity (nanometer) level. This single asperity nature of the contact proved useful in investigating the contact area dependence of the friction according to the adhesive friction given in equation 2. For single-asperity contacts under elastic contact conditions, the real area of contact varies non-linearly with applied load. Hence observation of a non-linear relationship between friction force and the normal load (typically $F \alpha N^a$, where *a* is typically a fraction) is suggestive of contact area dependence. A number of studies that have demonstrated contact area dependence of friction at the nanoscale are summarized in Table 1. The role of adhering contacts in the measurements are briefly discussed below.

Homola et.al.[5], using an SFA, showed that at low normal loads and in the absence of damage, friction on mica followed a single asperity contact and hence a dependence on contact area was noted. The contact area, in turn varied with normal load according to Johnson-Kendall-Roberts (JKR) [6] theory for adhesive contacts and Hertz theory for non-adhesive contacts. At higher loads, damage occurred and the contact area was believed to have entered the multiple asperity regime and whereupon the friction behavior followed the classical Amontons' law of friction with a unique friction coefficient value. Berman et.al.[7], using modified SFA experiments and a physical model based on intermolecular forces and

Table 1: Summary of micro/nanoscale friction experiments and observations on contact area dependence

Authors	Instrument	Sample	Experimental conditions	Contact area dependence		Contact area independence
		Mica		Contact theory	Interfacial shear strength	Coefficient of friction
Carpick et.al. [17]	UHV-AFM [a]		Vacuum, Pt-coated Si_3N_4 probe, Load range 0-200 nN	JKR [h]	0.27 GPa	
Carpick et.al. [24]	AFM [b]		55% RH, Si_3N_4 probe, Load range 0-40 nN	DMT [i]	680 MPa	
Carpick et.al. [21]	UHV-AFM[a]		Vacuum, Pt-coated Si_3N_4 probe, Load range 0-200 nN	JKR [h]	0.86 GPa	
Homola et.al. [5]	SFA [c]		Dry air, Load range 0-0.3 N	JKR [h]	20 MPa (before damage)	0.35 (after damage)
Pietrement et.al. [25]	MLFM [d]		60% RH, Si_3N_4 probe, Load range 0-50 nN	DMT [i]	590 MPa	
Pietrement et.al. [26]	MLFM [d]		Ambient, Si_3N_4 probe, Load range 0-60 nN	Carpick Generalized fit	450 MPa	
			Vacuum, Si_3N_4 probe, Load range 0-40 nN	Carpick Generalized fit	290 MPa	
Liu et.al. [11]	AFM [b]		50% RH, Si_3N_4 probe, Load range 30-180 nN			0.001-0.13
	Tribometer		50% RH, Si_3N_4 ball, Load range 1-15 N			0.17-0.35 (Initial), 0.08-0.52 (Steady)
Berman et.al. [7]	SFA [c]		Ambient, 0.5 M KCl soln, Load range 0-250 mN			0.015
Choo et.al. [12]	Ball-on-flat tribometer		Ambient, glycerol solution, Load range 0-0.05 N			0.33
Enachescu et.al. [27]	UHV-AFM [a]	H_2 terminated diamond(111)	Vacuum, Tungsten carbide tip, Load range 0-12 nN	DMT [i]	238 MPa	
Lantz et.al. [28]	UHV-AFM [a]	$NbSe_2$	Vacuum, Silicon tip, Load range 0-50 nN	Maugis-Dugdale	0.6 GPa	
Pietrement et.al. [20]	MLFM [d], MFMM [e]	HDPE [f]	Ambient, Si_3N_4 probe, Load range 0-60 nN	Carpick Generalized fit	27 MPa	
		HDPE [f]	Vacuum, Si_3N_4 probe, Load range 0-60 nN	Carpick Generalized fit	21 MPa	
Ho et.al. [9]	UHV-AFM [a]	UHMWPE [g]	Vacuum, Si_3N_4 probe, Load range 1-11 nN			0.22
Ruths [8]	AFM [b]	Template-stripped gold	Ambient, Si probe, ethanol solution, Load range 0-100 nN			0.42
Ruths et.al. [29]	AFM [b]	Benzyltrichloro-silane covered glass	Ambient, Monolayer coated probe, ethanol solution, Load range 0-10 nN			0.30
	SFA [c]		Ambient, ethanol solution, Load range 0-80 mN			0.30

[a] Ultra-high vacuum-Atomic force microscopy, [b] Atomic force microscopy, [c] Surface force apparatus, [d] Modulated lateral force microscopy, [e] Magnetic force modulation microscopy, [f] High-density polyethylene, [g] Ultra-high molecular weight polyethylene, [h] Johnson-Kendall-Roberts, [i] Derjaguin-Muller-Toporov

thermodynamic considerations, have shown that even at the molecular scale, friction can be proportional to normal load as Amontons' law suggests, if the materials are non-adhering. They argued that the friction is proportional to the contact area as suggested by Bowden and Tabor[1] only in the case of adhering surfaces. Ruths[8] reported a contact area-independent friction response on template-stripped gold using an AFM with a silicon probe in the presence of ethanol, which was used in order to reduce the effects of adhesion. Considering it to be purely non-adhesive contact, they were able to show that the friction varied linearly with normal load, in the absence of any damage. In general, contact area dependence is observed in experiments involving single-asperity adhesive contacts and in the absence of damage.

Several other researchers [9-16] have shown contact area dependence of friction, when working under low loads (adhesive regime) on various material interfaces under different environmental conditions. Some studies [9-11] have reported contact area-independent friction behavior using an AFM without the consideration of non-adhesive contacts. These reports of contact area-dependent and contact-area independent friction behavior at the single asperity level raises an important question as to whether a friction coefficient (Amontons' law) alone is a sufficient and/or valid interpretation of the friction behavior at the small scales. Coefficient of friction thus evaluated at nanoscale is often used for comparative purposes.

On the microscale (nominal contact area on the order of 100 μm^2), contact area-independent friction behavior has generally been reported and a friction coefficient is often quoted in these studies. For instance, Choo et.al. [12] reported a linear increase in friction on mica under ambient conditions using a ball-on-flat tribometer. Few researchers have

attempted to study the role of length scales on frictional behavior of a particular interface. Liu et.al. [11] have reported that the friction coefficients on mica obtained using the microtribometer is generally higher compared to the values obtained using an AFM cantilever. La Torre and Bhushan [10] examined the scale effects on the tribological properties of human hair. They showed that the coefficient of friction varies across scales, with macroscale being the largest and nanoscale being the smallest.

To fully understand the effect of length scale on contact area dependency of friction, it is useful to measure the friction response of a given material pair at multiple length scales while maintaining comparable environmental and loading conditions. In this study, we perform such a study on the nano and microscales using Si_3N_4 probes on mica and ultra-high molecular weight polyethylene (UHMWPE) with an AFM and ball-on-flat reciprocating microtribometer. The observed friction behavior is discussed in the context of contact area dependency at both scales.

3.2 Experimental Details

3.2.1 Materials

Hi-grade mica surfaces (1 in. x 1 in.) were purchased from Ted Pella Inc, Redding, CA. The surfaces were cleaved before use. The surface roughness (RMS) of the cleaved mica was 0.108 ± 004 nm (1 μm x 1 μm scan), as measured using an AFM. Commercially available, ram extruded GUR 1050, rod-stock; medical grade UHMWPE (Poly Hi Solidur, Fort Wayne, Indiana) was cut into small square (30 mm) pieces. The melting point of the polymer was established using differential scanning calorimetry (DSC) to be 125 ^{0}C. The

sample was heated to 200 ^{0}C and held for 3 hours after which it was held at 110 ^{0}C for 48 hours in order to allow recrystallization. The sample was clamped with minimal load against a quartz plate while heating to impart low consistent surface roughness. The final surface roughness (RMS) of the sample was 4.58 ± 0.18 nm (1 μm x 1 μm scan), as measured using an AFM.

3.2.2 Atomic Force Microscopy

AFM experiments in contact mode were carried out with a Dimension ™ 3100 AFM (Nanoscope IV, Veeco Instruments, Santa Barbara, CA) in controlled low humidity (6 ± 2 % RH) conditions to minimize effects of adsorbed water vapor. Standard V-shaped silicon nitride probes from Veeco with a quoted normal spring constant of 0.58 N/m and tip radius of 10-40 nm were used. The normal spring constant of the cantilever used was calibrated using the reference lever technique described by Torii et.al. [13] and found to have an actual value of 0.35 N/m. AFM force-displacement curves were used to determine the pull-off (adhesive) force, between the Si_3N_4 tip and the sample. Normal loads used were in the range of -15 nN (adhesive regime) to 60 nN.

Friction force scans were performed at a 90^0 scan angle on a 1 μm scan area at a speed of 4 μm/s. Friction force and adhesive force data presented are averages of five measurements at multiple sample locations. The friction force was calibrated using Ruan and Bhushan's method[14]. The radius of the tip was characterized before and after the experiments using a commercially available tip characterizer sample TGT01 (Mikromasch). The images were analyzed using commercial software (Image Metrology) to calculate the tip radius. The tip

profiles were generated using a MATLAB code. The typical tip radius was about 38 ± 2 nm which results in nominal contact areas of 10-100 nm^2 and average (Hertzian) pressures on the order of 0.4 - 2.5 GPa.

3.2.3 Microtribometer measurements

Microscale friction response was obtained using a custom-built ball-on-flat microtribometer. Tests were conducted using a smooth Si_3N_4 probe (radius ~ 1.2 mm) with a roughness of 4.3 ± 0.5 nm measured by an AFM as shown in Figure 1. A preliminary upper limit for the normal loads, to ensure elastic conditions, was obtained from a Hertzian analysis. Correspondingly, load ranges of 0-50 mN and 0-7 mN were used for friction tests

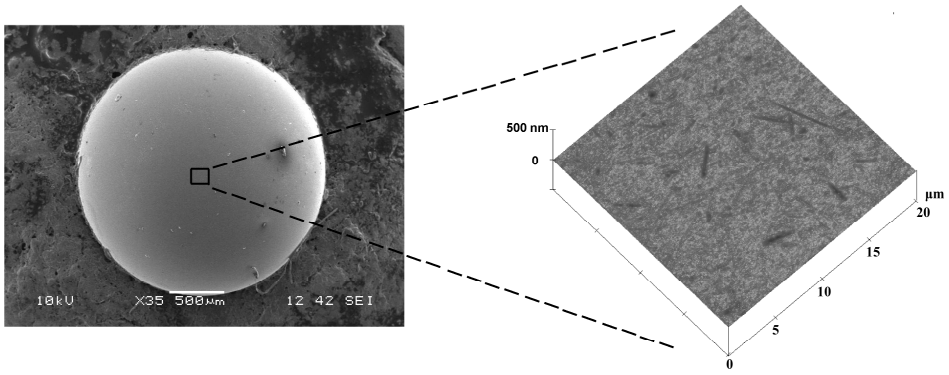

Figure 1: **(a)** SEM image of the silicon nitride probe used in the ball-on-flat microtribometer measurements. **(b)** Topography map (20 µm x 20 µm) of the silicon nitride probe surface obtained using an atomic force microscope (AFM). The RMS roughness is about 4.3 ± 0.5 nm.

on the UHMWPE and mica samples, respectively with a scan rate of 1 mm/s and a 15 mm stroke. An optical microscope was used to identify the onset of damage for each friction trace. The nominal contact areas obtained in the experiments, calculated using Hertzian analysis were on the order of 80 - 900 μm^2 and pressures on the order of 0.03 - 0.13 GPa.

3.3 Results and discussion

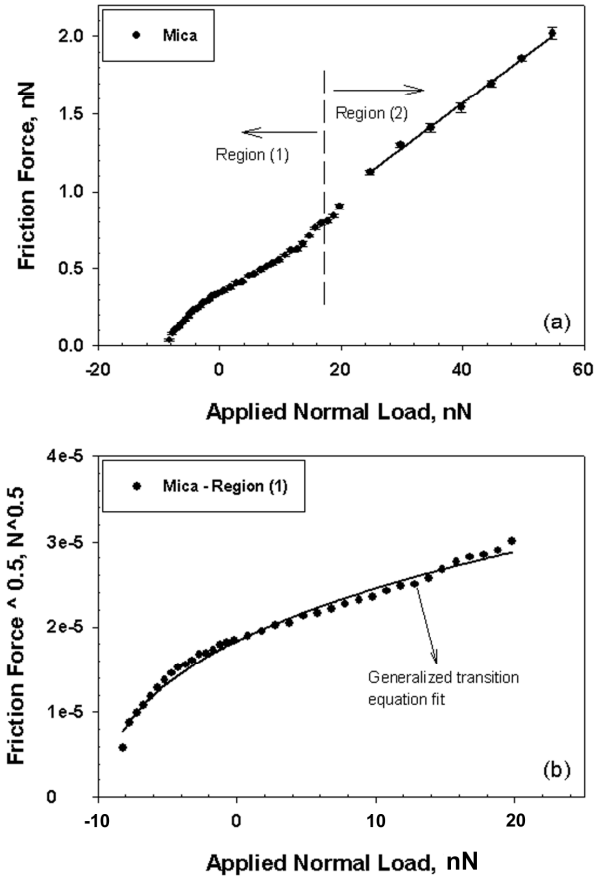

Figure 2: **(a)** AFM friction response as a function of applied normal load on mica **(b)** Generalized equation fit to region (1).

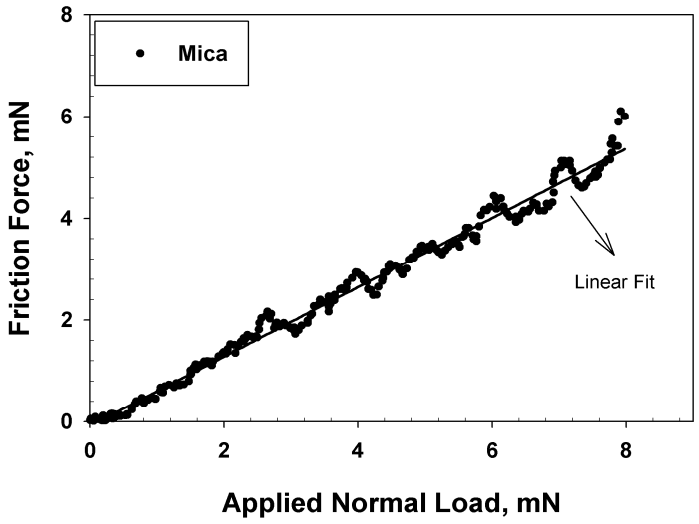

Figure 3: Microscale friction response on mica obtained using the microtribometer. Distinct contact area independent behavior seen, for which linear fit was employed according to Amontons' law.

Figure 2(a) shows a characteristic nanoscale friction response of the mica surface as a function of normal load obtained using the AFM. The friction showed an initial non-linear response (region 1) which is most evident in the adhesive regime. This region resulted in no discernible surface damage. Beyond a certain normal load (typically about 25 nN), the non-linearity is not very evident (region 2). Experiments in this regime almost always resulted in observable surface damage as shown in Figure 4(a).

The non-linearity of the friction with respect to normal load (at low loads) is strongly suggestive of contact area dependence. In the absence of surface damage (wear), the friction force is related to the interface contact area (A_r) according to Equation 2 where τ is the

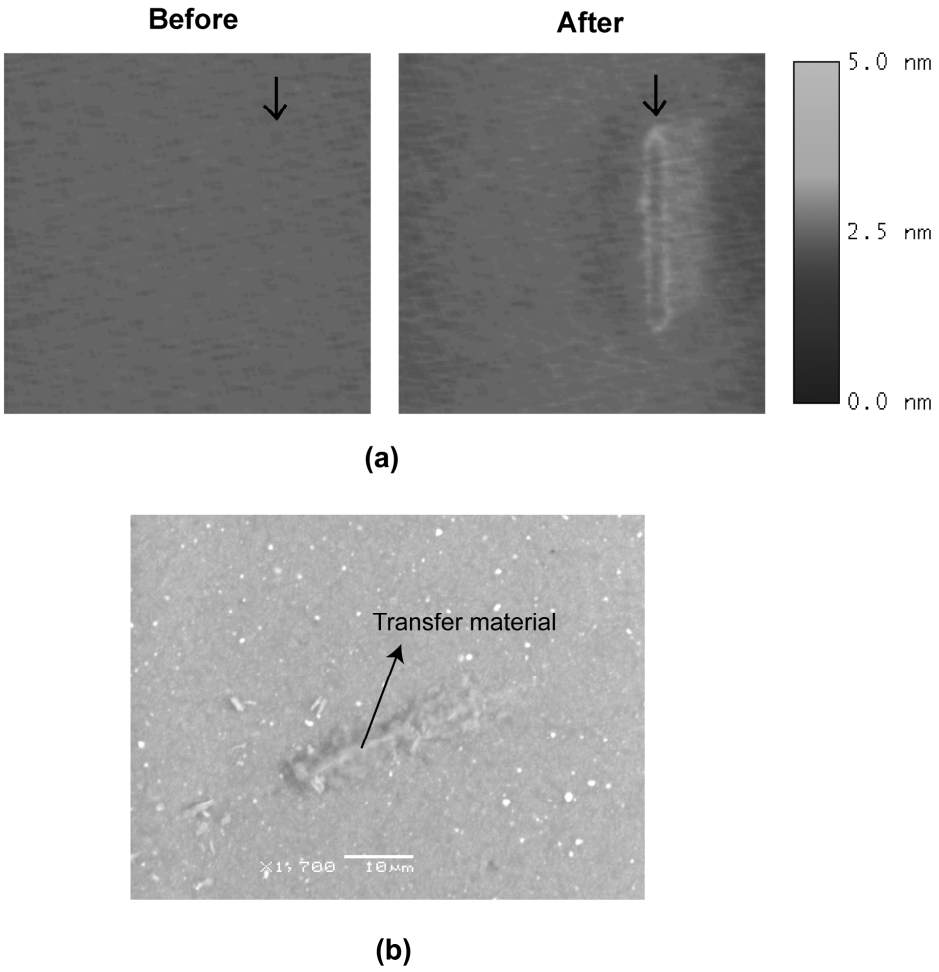

Figure 4: (a) AFM topography maps (2 μm x 2 μm area) of Mica obtained before and after AFM friction tests. The arrows indicate the region where the friction tests were performed. Considerable damage was observed beyond a normal load of 25 nN in the case of mica. (b) SEM image of the Si_3N_4 probe showing transfer layer from mica on the microscale.

interfacial shear strength, a fundamental property which may be a constant or pressure dependent [15, 16]. The non-dimensional Tabor parameter was calculated for the obtained data

to determine the appropriate contact mechanics to evaluate A_r as a function of applied normal load. The Tabor parameter is given by

$$\chi = \left(\frac{16 R \gamma^2}{9 K^2 z_0^3} \right)^{1/3} \tag{4}$$

Here R is the radius of the probe, γ is the work of adhesion, z_0 is the equilibrium spacing of the two surfaces (taken to be 0.2 nm [17]) and K is the composite elastic modulus given by

$$K = \frac{4}{3} \left[\frac{1 - \nu_1^2}{E_1} + \frac{1 - \nu_2^2}{E_2} \right]^{-1} \tag{5}$$

where $\nu_{1,2}$ and $E_{1,2}$ are the Poisson's ratio and elastic modulus of the tip and sample respectively. The elastic modulus and Poisson's ratio values for the materials involved in this study are given in table 2. The Tabor parameter obtained for mica was about 0.18. This value lies in the transition regime, indicating that the Maugis-Dugdale model [18] is most appropriate contact model to use. Carpick et.al. [19] proposed a generalized equation for the variation of contact area with applied normal load which approximates the Maugis solution very closely. Hence, Carpick's generalized equation [19] was utilized and an interfacial shear strength value was obtained.

In Carpick's analysis, the contact radius *a* is taken as the square root of the friction force, F_f and is given by

$$\frac{F_f^{0.5}}{F_0^{0.5}} = \left(\frac{\alpha + \sqrt{1 - (L / L_c)}}{1 + \alpha} \right)^{2/3} \tag{6}$$

Table 2: Mechanical properties of the materials used in this study

Sample	Elastic Modulus (GPa)	Poisson's ratio	RMS roughness (nm)
Silicon nitride	310 [9]	0.3 [9]	4.3 ± 0.5
Mica	56.5 [30]	0.1 [30]	0.108 ± 0.004
UHMWPE	2.42 ± 0.014 [a]	0.45 [9]	4.58 ± 0.18

[a] Measured using a nanoindenter at a peak load of 15 μN.

where F_0 is the friction force at zero normal load, L is the normal load and L_c is the pull-off force which can be obtained from AFM force curves. α and F_0 are free parameters which are obtained from the fit of equation 6 to the plot between square root of friction ($F_f^{0.5}$) and normal load (L) as shown in Figure 2(b). The equation appears to fit the data well, indicating that the variation of contact area with load is reasonably well described by Carpick's approximation of the Maugis-Dugdale contact model. The parameter α, obtained from the fit, is converted to the Maugis' elasticity parameter λ by the following equation as given by Carpick et.al. [19]

$$\lambda = -0.924 * \ln(1 - 1.02\alpha) \tag{7}$$

The λ value, thus obtained, is used to calculate a_0 by combining equations 8 and 9 where a_0 is the contact radius at zero normal load.

$$\hat{a}_0(\lambda) = 1.54 + 0.279 \cdot \left(\frac{2.28 \cdot \lambda^{1.3} - 1}{2.28 \cdot \lambda^{1.3} + 1} \right) \tag{8}$$

$$\hat{a}_0(\lambda) = a_0 \cdot \left(\frac{K}{\pi \gamma R^2} \right)^{1/3} \tag{9}$$

In equation 9, γ, R and K are the work of adhesion, radius of probe and composite elastic modulus respectively, as explained previously for Eq.4. One of the important requirements for the applicability of this contact model is a paraboloidal tip shape [19]. The tip shape and

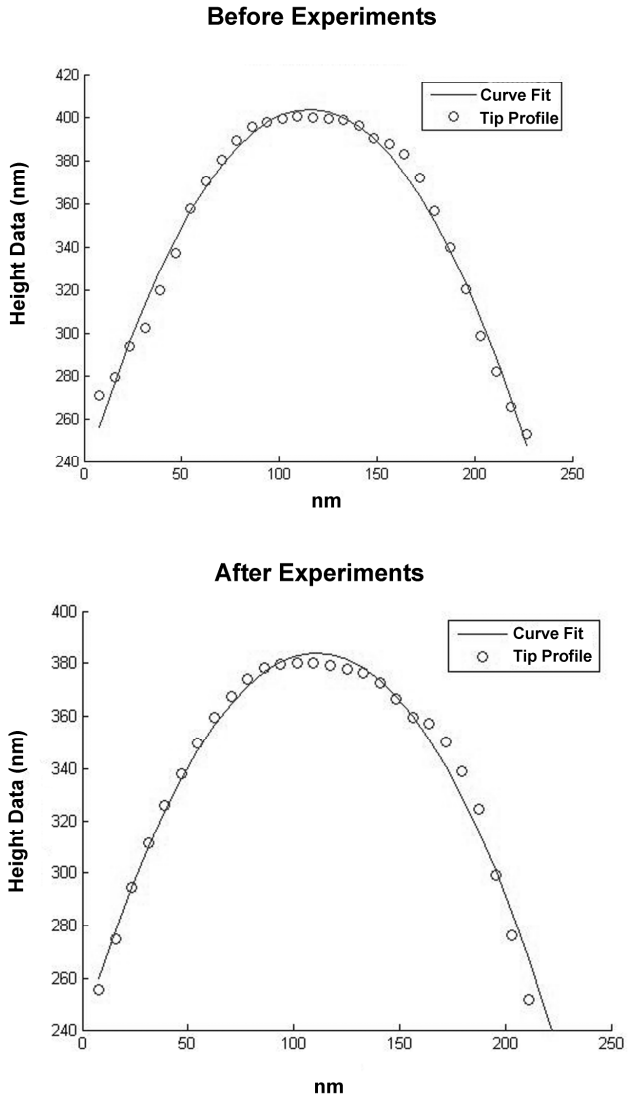

Figure 5: AFM probe profiles **(a)** before experiments and **(b)** after experiments obtained using a probe characterization sample. The curve fits indicate that the profiles are parabolic and that the probe experienced minimal wear during experiments.

radius of the probe, R, were monitored before and after the experiments using the commercial calibration sample TGT01. Figure 5 shows the tip profile of the AFM probe that we used for these experiments. The solid line represents a paraboloidal curve fit to the tip profile. The curve fit matches the tip profile quite well for both before and after experiments. Also, we note that there was negligible change in the probe radius during the course of the experiments. We also did not observe any decreasing trend in observed friction response with increasing number of trials, which suggests that transfer layers, if any, had negligible effect on our observations.

The shear strength is calculated as $F_0/\pi a_0^2$ where F_0 is obtained from the fit shown in Figure 2(b) and a_0 is obtained from equations 8 and 9. We note that in this model, τ is assumed to be a constant. Some researchers have reported a pressure dependency of τ in the case of polymers [20]. The shear strength value of 23.15 ± 5.19 MPa obtained in our experiments for the low load regime is comparable to the value of 20 MPa obtained by Homola et.al. [5] for mica surfaces under dry air atmosphere in an SFA experiment at low loads. Carpick et.al. [21] also reported the friction force on mica at low loads to be varying with contact area in accordance to JKR theory and reported a shear strength value of 0.86 GPa under UHV conditions. This value is three orders of magnitude greater than the value obtained in our study – the difference can be expected due to absence of adsorbed films and other contaminants under UHV conditions. The linear friction response in region (2) of our data (Figure 2(a)) yielded a coefficient of friction of 0.03 ± 0.002 according to Amonton's law. This value is comparable to values quoted by Liu et.al. [11] (0.001-0.13) and Berman et.al. [7] (0.015).

Figure 3 shows the microscale friction response of mica against the silicon nitride ball. Although some stick-slip behavior was observed, the friction data exhibited a linear dependence on normal load. A straight line fit yielded a coefficient of friction value of 0.72 ± 0.03 which is comparable to those reported in literature [11, 12]. Although optical and SEM analysis of the sample could not provide conclusive evidence of damage, SEM images of the probe, after experiments, showed clear evidence of material transfer from mica surface as shown in Figure 4(b). An Energy-Dispersive Spectroscopy (EDS) analysis confirmed the transfer of material from mica surface onto the probe. This suggests occurrence of some material removal from the sample which may be responsible for the linear trend in friction observed. The increase in the observed coefficient of friction values from nano to microscale has been reported by others [10, 22]. This increase has been attributed to larger amount of deformation occurring at the microscale due to the larger contact area and loads compared to nanoscale.

Figure 6(a) and 7 shows the nanoscale and microscale friction response for UHMWPE. The friction on the polymer UHMWPE, at both scales, shows non-linear dependence on normal load, which is suggestive of contact area dependence, for the applied load ranges of our experiments. Negligible surface damage was observed for the load ranges used in the AFM scale. No damage was evident on the sample surface as a result of the microscale tests. SEM analysis of the microtribometer probe also revealed no evidence of film transfer. The Tabor parameter for the nanoscale tests yielded a value of 1.63 which lies in the transition regime and hence, as described earlier for the nanoscale mica data, Carpick's generalized transition equation [19] was fit to the friction data as shown in Figure 6(b). The

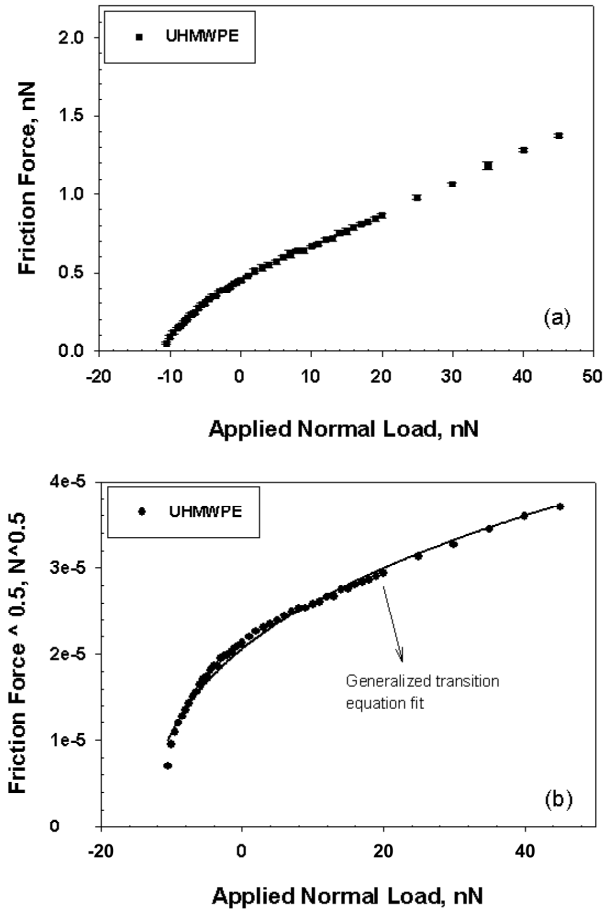

Figure 6: **(a)** AFM friction response obtained as a function of applied normal load on UHMWPE **(b)** Generalized equation fit to the data.

Tabor parameter for the microscale tests yielded a value much greater than 5. Hence, Johnson-Kendall-Robert (JKR) theory [6] was used to describe the contact behavior for the microscale UHMWPE data. In the JKR model [6], for a given material pair, the contact area is dictated by the probe radius and the work of adhesion between the probe and the sample. The real area of contact is given by

$$A_r^{\frac{3}{2}} = \frac{\pi^{\frac{3}{2}} R}{K}.\left[L + 3\pi R\gamma + \sqrt{6\pi R\gamma L + (3\pi R\gamma)^2}\right] \quad (10)$$

where γ, R and K are the work of adhesion, radius of probe and composite elastic modulus respectively, as explained previously for Eq.4 and L is the applied normal load. The work of adhesion was measured from pull-off forces (F_{PO}) performed using the microtribometer according to the relation derived from JKR analysis [6]:

$$F_{PO} = -\frac{3}{2}\pi R\gamma \quad (11)$$

Since our experiments were carried out in dry conditions, it is reasonable to assume that the adhesion component dominates over capillary contributions and that W_{12} can be estimated quite reliably from the above equation. A value of 0.0122 N/m was observed. This compared reasonably well with the value 0.055 N/m obtained using the AFM. The JKR fit to the data (Figure 6b) yielded interfacial shear strength of 3.17 ± 0.62 MPa.

Figure 7 shows the fit of equation 2 to the microscale friction response using JKR theory to describe A_r. Although the JKR fit does not represent the stick-slip like behavior, it does represent the overall trend reasonably well, despite the fact that JKR theory assumes smooth surfaces while the surfaces have a finite (albeit low) roughness. From the fit, an interfacial shear strength value of 2.27 ± 0.28 MPa was obtained. This is quite comparable to the interfacial shear strength value of UHMWPE obtained from the nanoscale measurements. By ensuring comparable experimental conditions, contact area dependence is observed at the micro and nanoscale for UHMWPE. These shear strength values are also comparable to the

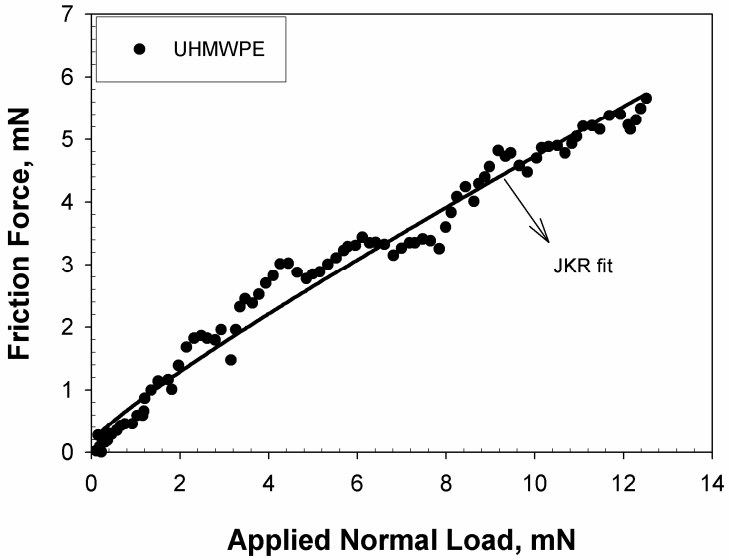

Figure 7: Microscale friction response on UHMWPE. UHMWPE shows a non-linear dependence on normal load to which a JKR fit is applied.

value of 6.95 MPa obtained from macroscale measurements in ambient conditions reported by Park et.al. [23]. As a further comparison, Gracias et.al.[16] and Pietrement et.al.[20] have reported a shear strength value of 17 MPa and 27 MPa for high density polyethylene (HDPE) in ambient air using a continuum force microscope (CFM) and modulated lateral force microscopy (MLFM) respectively.

3.4 Conclusions

We have evaluated the friction behavior of two materials, Mica and UHMWPE, at the micro and nanoscale while maintaining comparable environmental, loading and counterface

Table 3: Comparison of interfacial shear strength and friction coefficients on the two materials at the nanoscale (AFM) and microscale (tribometer)

	Interfacial shear strength (MPa)	
	AFM	**Microtribometer**
UHMWPE	3.17 ± 0.62	2.27 ± 0.28
Mica	23.15 ± 5.19	-
	Coefficient of friction	
	AFM	**Microtribometer**
UHMWPE	-	-
Mica	0.03 ± 0.002 (region 2)[a]	0.72 ± 0.03

[a] Refer to Figure 2(a)

(Si_3N_4) conditions. Table 3 provides a comparison of the interfacial shear strength and friction coefficients obtained on the two materials at both micro and nanoscale. Friction behavior on UHMWPE showed a contact area dependence on both the micro and nanoscales.Careful consideration and application of appropriate contact mechanics theories resulted in comparable values of shear strength at both scales. Friction on mica, at the nanoscale, showed initial contact area dependence up to certain loads after which behavior according to Amonton's law (i.e. friction is linearly proportional to normal force) was observed due to onset of damage at the surface. Friction on mica, at the microscale, showed no contact area dependence whatsoever, which is attributed to the occurrence of material removal during the sliding experiments.

References

1. F. P. Bowden; D. Tabor, *The Friction and Lubrication of Solids*. 1950.

2. D. Tabor; Winterto.Rh, *Proceedings of the Royal Society of London Series a-Mathematical and Physical Sciences* **1969,** 312, (1511), 435-&.

3. J. N. Israelachvili; D. Tabor, *Proceedings of the Royal Society of London Series a-Mathematical and Physical Sciences* **1972,** 331, (1584), 19-&.

4. G. Binnig; C. F. Quate; C. Gerber, *Physical Review Letters* **1986,** 56, (9), 930-933.

5. A. M. Homola; J. N. Israelachvili; P. M. McGuiggan; M. L. Gee, *Wear* **1990,** 136, (1), 65-83.

6. K. L. Johnson; K. Kendall; A. D. Roberts, *Proceedings of the Royal Society of London Series a-Mathematical and Physical Sciences* **1971,** 324, (1558), 301-&.

7. A. Berman; C. Drummond; J. Israelachvili, *Tribology Letters* **1998,** 4, (2), 95-101.

8. M. Ruths, *Langmuir* **2003,** 19, (17), 6788-6795.

9. S. P. Ho; R. W. Carpick; T. Boland; M. LaBerge, *Wear* **2002,** 253, (11-12), 1145-1155.

10. C. LaTorre; B. Bhushan, *Ultramicroscopy* **2006,** 106, (8-9), 720-734.

11. E. Liu; B. Blanpain; J. P. Celis; J. R. Roos, *Journal of Applied Physics* **1998,** 84, (9), 4859-4865.

12. J. H. Choo; H. A. Spikes; M. Ratoi; R. Glovnea; A. Forrest, *Tribology International* **2007,** 40, (2), 154-159.

13. A. Torii; M. Sasaki; K. Hane; S. Okuma, *Measurement Science & Technology* **1996,** 7, (2), 179-184.

14. J. A. Ruan; B. Bhushan, *Journal of Tribology-Transactions of the Asme* **1994,** 116, (2), 378-388.

15. R. W. Carpick; M. Salmeron, *Chemical Reviews* **1997,** 97, (4), 1163-1194.

16. D. H. Gracias; G. A. Somorjai, *Macromolecules* **1998,** 31, (4), 1269-1276.

17. R. W. Carpick; N. Agrait; D. F. Ogletree; M. Salmeron, *Langmuir* **1996,** 12, (13), 3334-3340.

18. D. Maugis, *Journal of Colloid and Interface Science* **1992,** 150, (1), 243-269.

19. R. W. Carpick; D. F. Ogletree; M. Salmeron, *Journal of Colloid and Interface Science* **1999,** 211, (2), 395-400.

20. O. Pietrement; M. Troyon, *Surface and Interface Analysis* **2001,** 31, (11), 1060-1067.

21. R. W. Carpick; N. Agrait; D. F. Ogletree; M. Salmeron, *Journal of Vacuum Science & Technology B* **1996,** 14, (2), 1289-1295.

22. B. Bhushan; J. N. Israelachvili; U. Landman, *Nature* **1995,** 374, (6523), 607-616.

23. K. D. Park; J. Kim; S. J. Yang; A. Yao; J. B. Park, *Journal of biomedical materials research, Part B: Applied Biomaterials* **2003,** 65B, (2), 272-279.

24. R. W. Carpick; D. F. Ogletree; M. Salmeron, *Applied Physics Letters* **1997,** 70, (12), 1548-1550.

25. O. Pietrement; J. L. Beaudoin; M. Troyon, *Tribology Letters* **1999,** 7, (4), 213-220.

26. O. Pietrement; M. Troyon, *Langmuir* **2001,** 17, (21), 6540-6546.

27. M. Enachescu; R. J. A. van den Oetelaar; R. W. Carpick; D. F. Ogletree; C. F. J. Flipse; M. Salmeron, *Tribology Letters* **1999,** 7, (2-3), 73-78.

28. M. A. Lantz; S. J. Oshea; M. E. Welland; K. L. Johnson, *Physical Review B* **1997,** 55, (16), 10776-10785.

29. M. Ruths; N. A. Alcantar; J. N. Israelachvili, *Journal of Physical Chemistry B* **2003,** 107, (40), 11149-11157.

30. S. Kopta; M. Salmeron, *Journal of Chemical Physics* **2000,** 113, (18), 8249-8252.

CHAPTER 4. THE EFFECT OF PROTEIN ADSORPTION ON THE FRICTION BEHAVIOR OF ULTRA-HIGH MOLECULAR WEIGHT POLYETHYLENE

Modified from a paper published in *Tribology Letters*
2006, 22(2), 181-188
K.S. Kanaga Karuppiah, Sriram Sundararajan, Zhi-Hui Xu, Xiaodong Li

4.1 Introduction

Total joint replacement (TJR) is a procedure in which damaged joints are removed and replaced with an artificial device (prosthesis). Though joint replacement procedures are mostly successful, the artificial joints can become loose and unstable during use as a result of wear [1-4], requiring expensive revision surgery to replace a failed replacement joint. Herbert et.al. [5] have reported that a revision surgery costs three to four times more hospital resources than a primary knee implant. Researchers have also shown future trends of primary knee implants and revision surgeries to be continually increasing in many regions [6, 7]. Improved durability and reliability of the joint can reduce the need for revision surgeries associated with TJRs. Tribological properties of the articulating surfaces in TJRs have been identified as critical factor affecting their durability and reliability. For example, in a hip joint, the interface between the femoral head (usually a hard material) and acetabular cup lining (usually a softer material) is critical in determining the useful life of the implant. There has been an evolution of material pairs used for this interface beginning with Charnley's work with stainless steel heads and Teflon liners [8] Today, the combination of a

UHMWPE liner and metallic or ceramic (cobalt chromium, titanium, alumina and zirconia based materials) femoral heads [9-11] are extensively used. However, the average lifetime of artificial hip joints incorporating UHMWPE is only 15-20 years. Considerable amount of research has been devoted to improving the wear life of the UHMWPE based prosthesis.

The interaction of the TJR materials with the synovial fluid, which acts as the natural lubricant for human joints and minimizes friction and wear in the joint, is an important factor affecting the tribological performance of the materials [12-15]. The synovial fluid contains various kinds of serum proteins, hyaluronic acid and lipids, with albumin constituting almost 60% of the total protein concentration [15, 16]. Proteins affect the friction and wear of UHMWPE more significantly than the other constituents [15]. The adsorption mechanism of proteins onto the polymeric surface can affect its subsequent friction behavior [17]. Tailoring the hydrophobicity of UHMWPE can affect the protein adsorption and hence the friction behavior of the polymer surface [17, 18]. Clearly, it is of importance to understand how the tribological characteristics of UHMWPE change as soon as the TJR comes in contact with the synovial fluid.

Another factor affecting the tribological performance of UHMWPE in implants is its processing. Medical grade UHMWPE stock material may undergo a variety of processing techniques during implant manufacturing [19], including molding, extrusion and milling or turning. These manufacturing processes can affect the surface morphology and mechanical properties of the polymer [20, 21], which in turn can affect its friction and wear performance.

The objective of this study is to measure the friction response of medical grade UHMWPE using atomic force/friction force microscopy (AFM/FFM) as a function of protein

adsorption and processing. FFM techniques are used because accurate determination of the probe and contact dimensions is possible, thereby allowing calculation of interfacial shear strength [22] for the material pairs used based on classical friction theory and contact mechanics. This approach enables us to understand underlying mechanisms of changes in friction response. Correlations between protein adsorption mechanism, processing technique and observed friction behavior are discussed.

4.2 Experimental Details

4.2.1 Materials

Commercially available, ram extruded GUR 1050, 2 in diameter rod-stock; medical grade UHMWPE (Poly Hi Solidur, Fort Wayne, Indiana) was cut into 0.25 in thick semi-circular pieces. One of the samples was milled to give a surface roughness (RMS) of 6.98 ± 0.85 nm over a scan area of 1 μm x 1 μm, as measured using an AFM. Another sample was heated to above its melting point (to 140 ^{0}C) in a temperature controlled oven while being pressed against a glass slide with minimal load to impart low surface roughness. The sample was allowed to cool at room temperature. Room temperature was reached in about one to two hours. The roughness of this melt sample over a scan area of 1 μm x 1 μm was 3.55 ± 0.9 nm.

4.2.2 Atomic Force Microscopy

AFM experiments in contact mode were carried out with a Dimension ™ 3100 AFM (Nanoscope IV, Veeco Instruments, Santa Barbara, CA) in controlled low humidity (10 ± 4 % RH) conditions to minimize effects of adsorbed water vapor. Standard V-shaped silicon nitride probes from Veeco with a quoted normal spring constant of 0.58 N/m and tip radius of 10-40 nm were used. The normal spring constant of the cantilever used was calibrated using the technique described by Torii et.al. [23] and found to have actual values of 0.20-0.25 N/m. The pull-off (adhesive) force between the Si_3N_4 tip and the UHMWPE was measured before and after each test from force-displacement curves.

For friction measurements, the probe was scanned perpendicular to the long axis of the cantilever. The friction response of the probe on the sample was taken to be the difference between the lateral deflection values of the forward and reverse scans of a given scan line (i.e. from the friction loop of a scan line). This method is commonly used to eliminate contributions to the lateral deflection signal from non-friction sources [24]. Normal loads were varied from 5 to 100 nN. Friction response was monitored on indexed areas on the samples before exposure to proteins. The areas were then exposed to protein solution and assessed for protein adsorption (explained in the next section) before the friction response was measured again. Friction force and adhesive force data presented are averages of six measurements at multiple sample locations. The friction force was calibrated using Ruan and Bhushan's method [25]. The radius of the tip was characterized before and after the experiments using a commercially available tip characterizer sample TGT01 (Mikromasch). The images were analyzed using commercial software (Image Metrology) to calculate the tip radius.

4.2.3 Nanoindentation measurements

Nanoindentation tests were performed on the polymer samples with a Berkovich indenter using a Hysitron Triboscope (Hysitron Inc., Minneapolis, Minnesota, USA) in conjunction with an AFM (Nanoscope Dimension^{TM} 3100, Digital Instruments, Veeco Metrology Group). Two different loading profiles were used for the test. One is a standard trapezoidal loading profile with an equal loading and unloading rate of 15 μN/s, a peak indentation load of 15 μN, and a 1 second holding segment. The other is a partial loading and unloading profile with an equal loading and unloading rate of 5 μN/s and 10 different peak indentation loads ranging from 2.5 to 25 μN. At each peak load, appropriate holding time was assigned. During indentation tests, the sample was held firmly by the vacuum chuck of AFM. The mechanical properties, namely hardness and elastic modulus, were obtained using the Oliver and Pharr method [26].

4.2.4 Protein adsorption and Fluorescence measurements

For this study, bovine serum albumin (BSA) tagged with fluorescein isothiocyanate (FITC) dye (Sigma-Aldrich, Cat. No. A9771) was dissolved in Phosphate-buffered saline (PBS) solution of pH 7.4 (1X) (Invitrogen, Cat. No. 10010-023) to make up a concentration of 7.2 mg/ml (BSA) representing 10 vol% dilution. This dilution is comparable to the protein concentration in the human synovial fluid [18]. 20 μl of the protein solution was placed on a small indexed area of each UHMWPE sample for 5 minutes, following which the samples were rinsed with de-ionized water and dried with nitrogen gas. Protein adsorption onto the samples was qualitatively measured using fluorescence microscopy. The samples were

viewed under a confocal fluorescence microscope using a FITC filter with a wavelength passband of 492 ± 9 nm. The FITC dye fluoresces at a wavelength of 495 nm and has a very short half-life. Hence, fluorescence images were collected on 4 different locations on the sample within a one-minute span. The exposure time and gain settings were kept constant for all measurements to ensure valid comparison of pixel intensity across different samples. The images were imported into ADOBE Photoshop software, where regions of interest were selected on the image and a histogram analysis of the pixels of the selected region was carried out. From the histogram, the average image intensities were calculated.

4.2.5 Contact angle measurements

Hydrophobicity of the UHMWPE before and after exposure to BSA was measured using contact angle measurements. The contact angle was measured by taking high magnification digital pictures of 8 μl water droplets on each sample using a CCD camera. The pictures were imported into an image analysis software (Scion Image) and the contact angles were measured.

4.3 Results

Figure 1 shows representative AFM topography maps of the UHMWPE samples. The melt sample displayed a lamellar type of structure that is indicative of recrystallization and has been reported in previous studies [19, 27]. Results from the nanoindentation measurements are shown in Figure 2. The plot shows the typical load penetration depth curves for both the melt and milled sample under two different loading profiles. Figure 2(a)

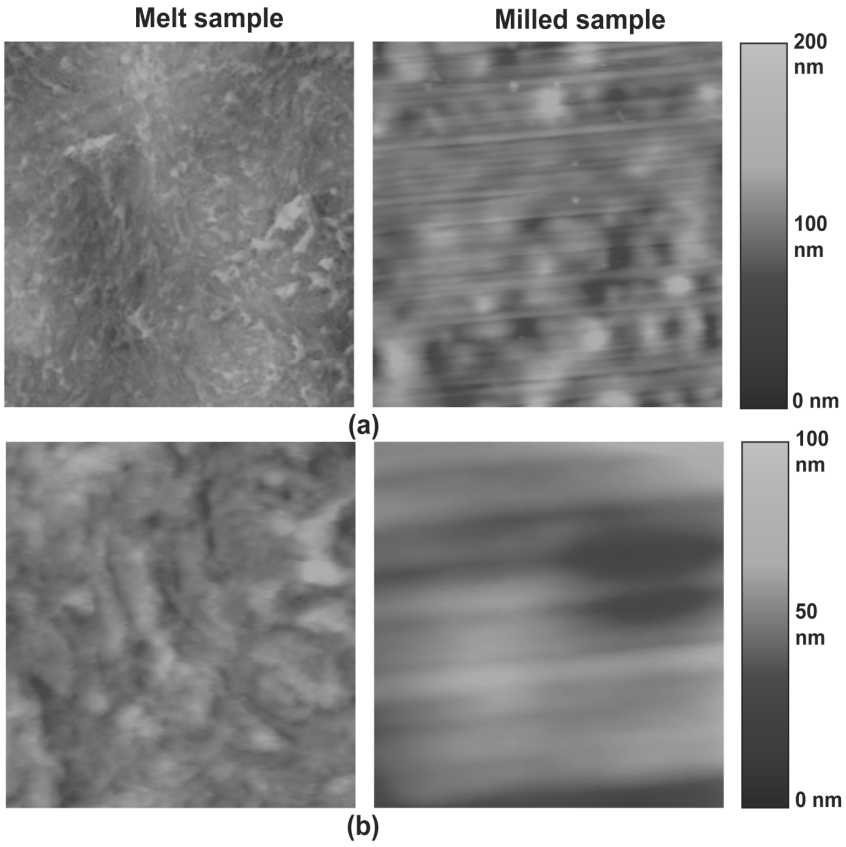

Figure 1: Topography maps of melt and milled samples **(a)** 5 μm X 5 μm and **(b)** 1 μm X 1 μm scan sizes obtained using an atomic force microscope (AFM).

shows the standard loading profile. As can be seen, the maximum load for indentation has not reached the peak load intended to apply due to the significant creep of the materials. At a penetration depth smaller than 50 nm, the milled sample shows the least penetration among the two samples and higher surface stiffness. At the end of the unloading, indentation force dropped below zero, which may indicate adhesion between indenter and the polymer. Figure 2(b) shows the curve with partial loading and unloading profile. The elastic modulus and hardness are determined from the partial unloading curves at different peak loads. The

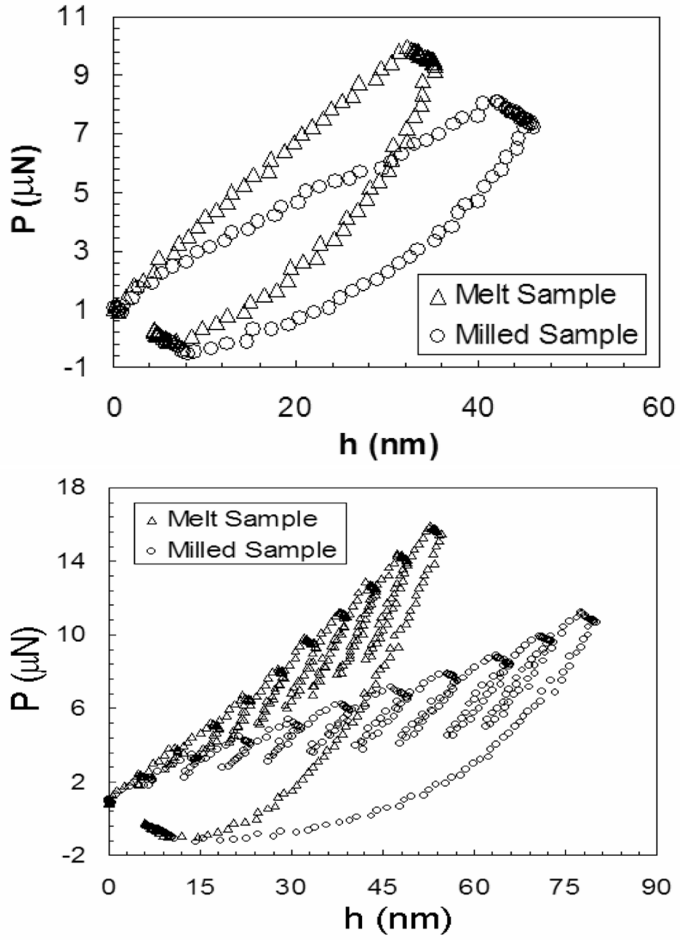

Figure 2: Load-penetration (P-h) depth curves from nanoindentation tests on both melt and milled sample with **(a)** standard loading profile **(b)** partial loading and unloading profile.

variation of elastic modulus and hardness with the indentation contact depth is plotted in Figure 3. Only data with penetration depths over 10 nm were selected in order to avoid the effects of surface roughness. Figure 3 indicates that the melt sample shows higher elastic modulus and hardness than the milled sample at all contact depths. Also, note that, for contact depth larger than 30 nm, elastic modulus is independent of contact depth whereas the hardness decreases steadily with the increase in contact depth for both the samples.

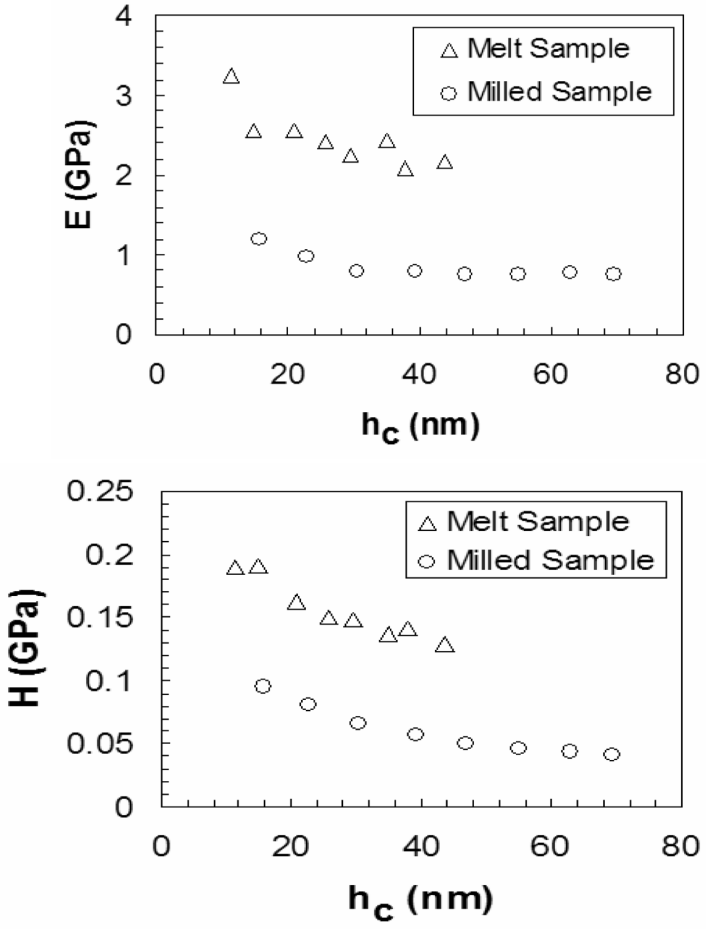

Figure 3: **(a)** Elastic modulus (E) and **(b)** hardness (H) as a function of indentation contact depth (h_c). Only data with contact depths over 10 nm were selected to avoid the influence of surface roughness.

Figure 4 shows the friction response of the UHMWPE samples before and after exposure to BSA. For all the samples, the friction force increased with increase in normal load. The melt sample showed higher friction than the milled sample. Both samples exhibited an increase in friction response upon exposure to BSA. Figure 4 shows that the magnitude of this increase was considerably larger in the case of the milled sample.

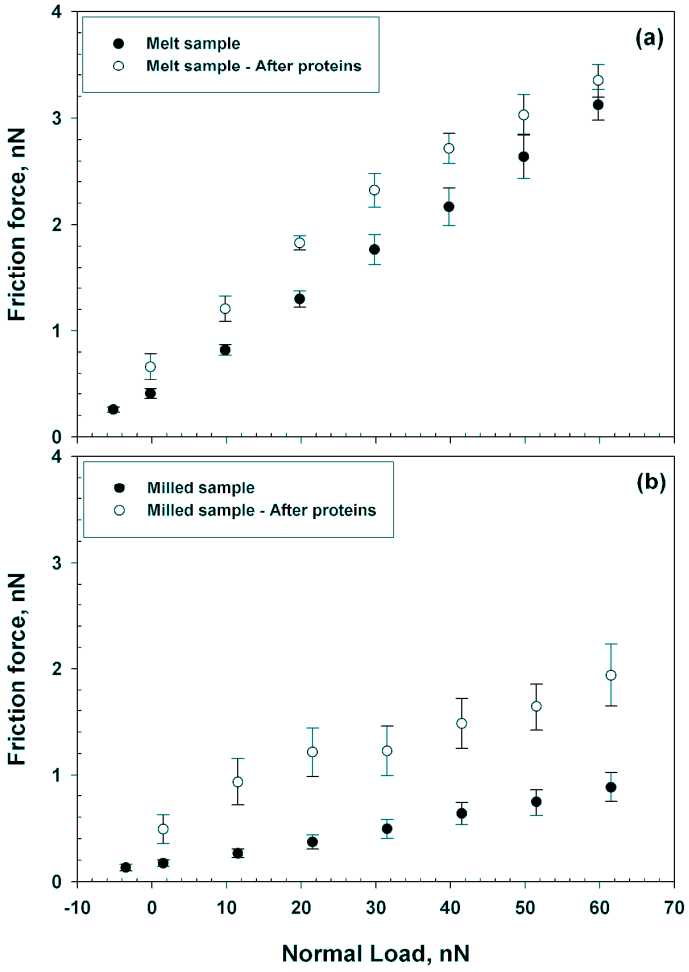

Figure 4: AFM friction response as a function of normal load before and after exposure to protein solution for **(a)** melt and **(b)** milled sample. The friction response increases upon exposure to proteins in both cases.

For the friction experiments, no discernable wear was observed up to loads of 80 nN. Permanent damage (groove depths on the order of 2 – 10 nm) was observed at loads beyond 80 nN. In the absence of wear, the predominant mechanism during the FFM experiments can be assumed to be adhesive. The adhesive friction is then given by [28]:

$$F_a = \tau_0 A_r + \beta L \quad (1)$$

where τ_0 is the interfacial shear strength, A_r is the real area of contact, β is a constant that describes the normal load dependency of the shear strength and L is the normal load. The real area of contact can be evaluated using an appropriate contact mechanics theory while τ_0 and β are typically evaluated using curve fits. In order to determine the contact theory best suited for our experimental conditions, friction force data was plotted as a function of applied normal load and a curve fit was performed using the generalized transition analysis by Carpick et.al. [29] to determine the contact parameter α. According to their analysis, the value of α reliably predicts the appropriate contact theory to use and is analogous to the Maugis criterion. Specifically, $\alpha = 1$ indicates that the Johnson-Kendall-Roberts (JKR) contact model [30] is appropriate while $\alpha = 0$ would require the use of the Derjaguin-Muller-Toporov (DMT) model [31]. For intermediate values ($0 < \alpha < 1$), the Maugis-Dugdale model [32] would provide the most accurate results. The analysis for all the samples used this study resulted in α values very close to zero. The DMT model was therefore utilized to determine the contact area for the experiments presented in this paper. According to the DMT model, for a given material pair, the contact area is dictated by the probe radius and the work of adhesion between the probe and the sample. The real area of contact is given by

$$A_r = \pi \left[\frac{3R^*}{4E^*} . \left[L + 2\pi R^* W_{12} \right] \right]^{\frac{2}{3}}, \quad (2)$$

where R^* is the composite radius and E^* is the composite modulus given by

$$E^* = \left(\frac{1 - \upsilon_1^2}{E_1} + \frac{1 - \upsilon_2^2}{E_2} \right)^{-1} \quad (3)$$

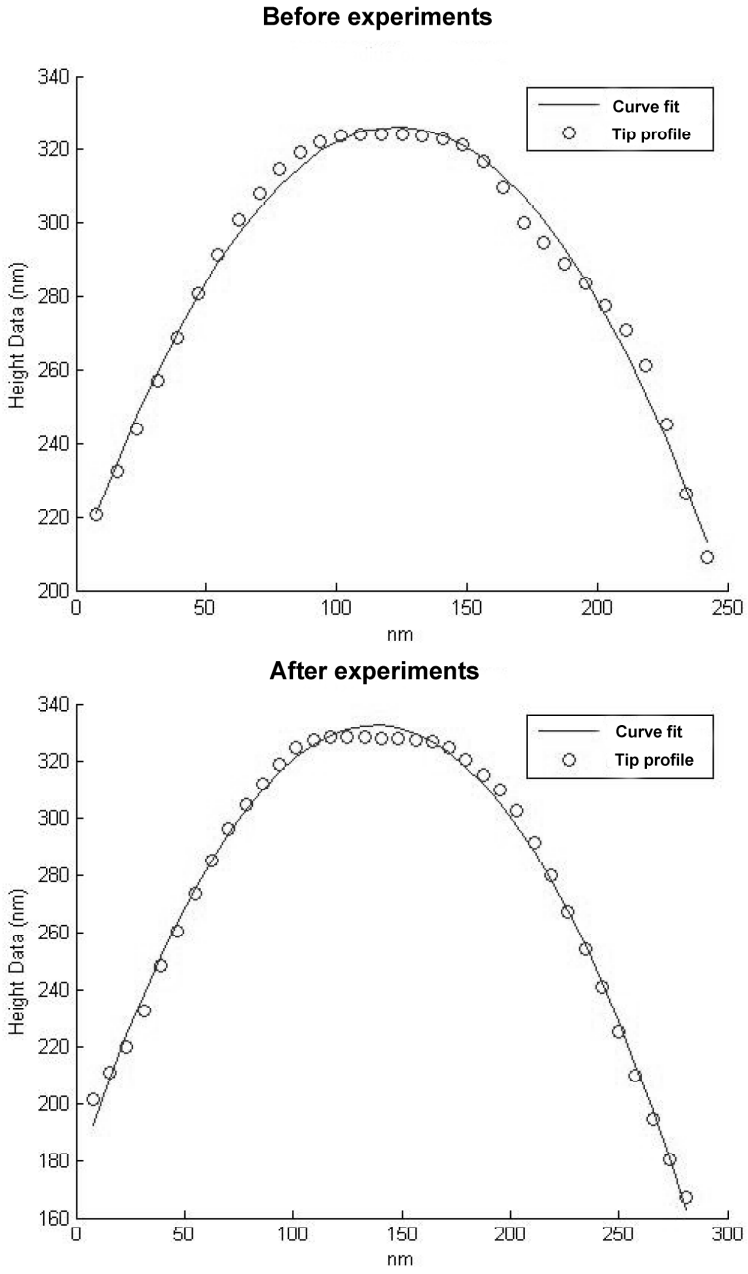

Figure 5: AFM probe profiles **(a)** before experiments and **(b)** after experiments obtained using a probe characterization sample. The curve fits clearly indicate that the profiles are parabolic and that the probe experienced negligible distortion during experiments.

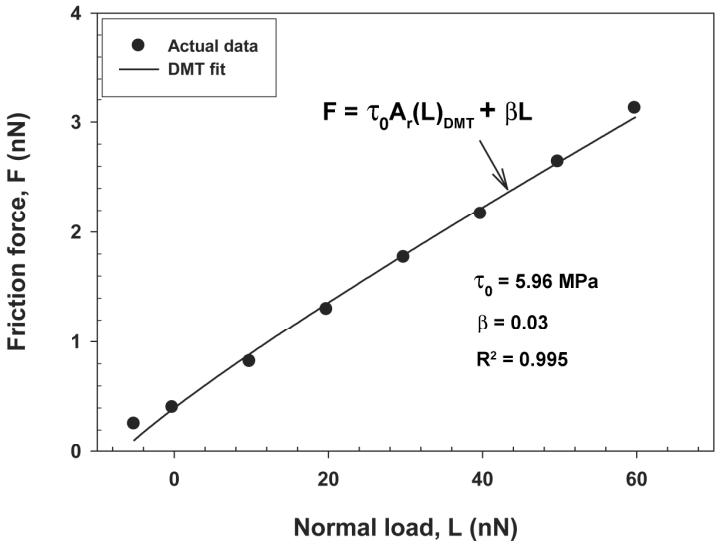

Figure 6: Example of friction force data and curve fit based on DMT contact mechanics-based calculation of the real area of contact (A_r). The data fits the theory quite well. The interfacial shear strength (τ_0) and load dependency parameter (β) are obtained from the fit. Data shown here is for the melt sample.

The contact-depth independent elastic modulus values obtained from the nanoindentation experiments (Table 1) and an assumed value of Poisson's ratio of 0.36 were utilized for these calculations. The work of adhesion (W_{12}) was measured from pull-off forces (F_{PO}) for various samples from the following equation derived from the DMT analysis:

$$F_{PO} = -2\pi R^{*} W_{12} \tag{4}$$

Since the AFM experiments were carried out in dry conditions, it is reasonable to assume that the adhesion component dominates over capillary contributions and that W_{12} can be estimated quite reliably from the above equation. It is noted that the DMT analysis assumes

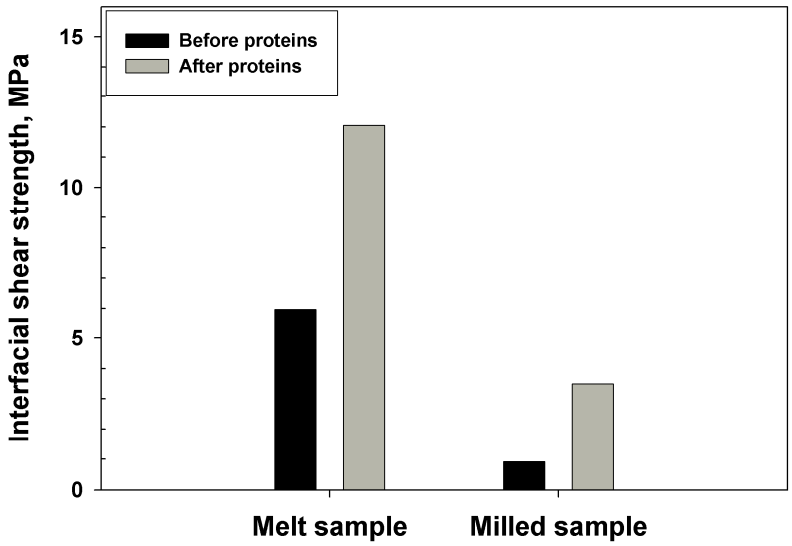

Figure 7: Interfacial shear strength (τ_0) values before and after exposure to proteins on melt and milled samples. The interfacial shear strengths of the samples increase upon exposure to proteins.

that no wear occurs during contact and that the probe has a parabolic profile. As discussed earlier, no discernable wear was observed on the samples up to loads of 80 nN. The probe radius was closely monitored before and after each experiment using the probe characterization sample. Figure 5 shows that the probe does indeed exhibit a parabolic profile. The probe shape was not significantly altered during experiments, thus allowing the use of the DMT model to calculate A_r.

The parameters τ_0 and β can then be obtained by fitting Eq. 1 to the friction force data as shown in Figure 6. The figure shows that the DMT-based equation gives a very good fit, which was characteristic of the friction data for all the samples. The shear strength values (τ_0) obtained for the various samples are shown in Figure 7. The obtained values for τ_0 and β

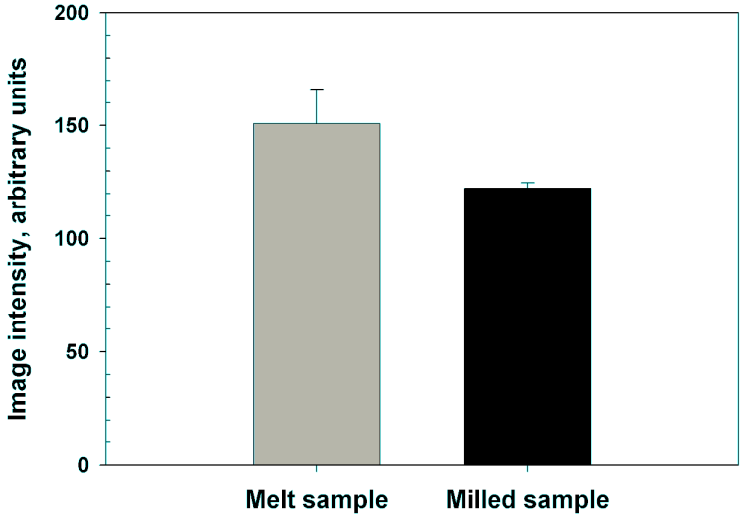

Figure 8: Results from fluorescence measurements on melt and milled samples after exposure to protein solution. The melt sample shows higher levels of protein adsorption.

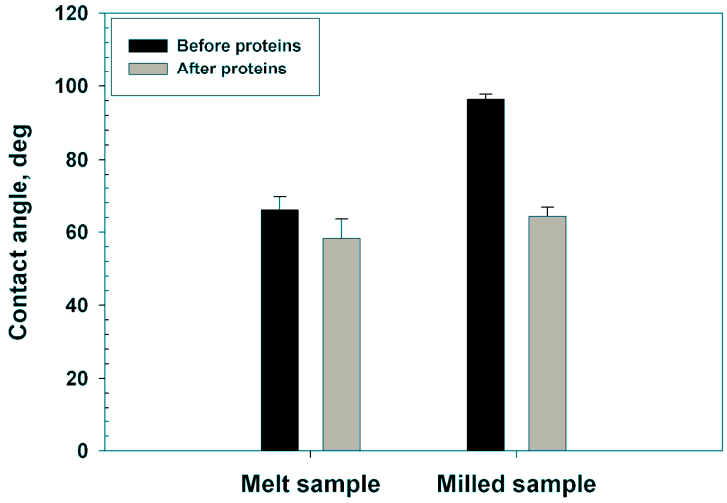

Figure 9: Contact angle measurements before and after exposure to proteins on both melt and milled samples. Protein adsorption renders the surfaces more hydrophilic.

are also listed in Table 1. The measured interfacial shear strength of the UHMWPE samples prior to protein adsorption was comparable to those measured using macroscale torsion tests (1-7 MPa) [33]. Exposure to proteins resulted in a 300% increase in the shear strength in the case of the milled sample whereas the increase in the shear strength was about 100% for the melt sample. The values of β obtained are comparable to values reported for high density and low density polyethylene (0 – 0.05) [34]. Values of β obtained for our UHMWPE samples imply that the melt samples exhibit a slightly higher normal load dependency compared to the milled samples, which displayed values closer to zero (Table 1). In both the milled and melt samples, the β values decreased upon exposure to proteins.

Results of the fluorescence measurements for both the samples are shown in Figure 8. The melt sample showed a higher image intensity indicating higher levels of protein adsorption compared to the milled sample. The contact angle data for the two samples are shown in Figure 9. The milled sample was initially significantly more hydrophobic than the melt sample. In both cases, adsorption of BSA rendered the surfaces more hydrophilic. The reduction in contact angle was very significant in the case of the milled sample as compared to the melt sample.

4.4 Discussion

Table 1 provides a comparison of all surface characteristics of the samples measured and the effect of protein adsorption on the parameters. The data shows that protein adsorption tend to increase the friction behavior and interfacial shear strength of UHMWPE. Widmer et.al. [17] showed that hydrophobic polyethylene surfaces exhibit higher friction

Table 1: Comparison of surface characteristics for the two samples. Measured values indicated are average ± standard deviation.

Sample	RMS roughness [a] (nm)	Elastic modulus[b] (GPa)	Hardness[b] (GPa)	Contact angle (deg)	Interfacial shear strength[c], τ_0 (MPa)	β^c
Melt sample	3.55±0.90	2.10±0.08	0.151±0.003	66.1±3.57	5.96	0.03
Melt sample - After proteins	3.28±0.28	-		58.3±5.24	12.04	0.01
Milled sample	6.98±0.85	0.90±0.07	0.073±0.005	96.3±1.43	0.919	0.005
Milled sample - After Proteins	7.78±0.75	-		64.3±2.53	3.50	0

[a]Measured using AFM over a 1 μm x 1 μm scan area
[b]Measured using a nanoindenter at 15 μN peak load
[c]Calculated from fit of Eq. 1 (according to DMT contact mechanics) to FFM data

than hydrophilic ones. They used optical waveguide lightmode spectroscopy (OWLS) to show that proteins adsorbed onto hydrophobic surfaces occupy more surface area than those that adsorb onto hydrophilic surfaces. They therefore proposed that proteins denature during adsorption onto a hydrophobic surface. The denaturing of proteins upon adsorption on hydrophobic surfaces has been reported in relation to other applications [35, 36] as well. Denatured proteins occupy large surface area, with hydrophobic parts undergoing adsorption, exposing hydrophilic regions. Our contact angle data supports the idea that the proteins denature upon adsorption onto the hydrophobic UHMWPE surfaces or that denatured

proteins adsorb preferentially onto the hydrophobic surfaces. The data therefore indicates that a denatured protein layer forms a high shear strength layer which increases the adhesive friction response. An increase in the interfacial shear strength may have implications for adhesive wear mechanisms. However higher friction in most cases does not necessarily imply higher wear and one should evaluate wear behavior independently from friction experiments. Protein adsorption has been previously reported to increase the wear rates of UHMWPE [12, 37] as well as decrease them [38, 39]. The effect of the denatured layer on the adhesive wear response is the focus of the authors' present research. The melt sample showed higher protein adsorption but lower increase in friction upon exposure to protein as compared to the milled sample. This suggests that the conformation of the adsorbed proteins affects the friction performance more significantly than the quantity of adsorbed proteins.

It is also clear that the surface treatment plays a crucial part in affecting the interfacial shear strength of the samples and the protein adsorption. The melting and reforming process can affect the degree of crystallinity of the sample [27]. Our melt sample exhibited lower contact angle and hence higher surface energy which is suggestive of higher degree of crystallinity [40]. The higher surface energy of the melt sample reduces the extent of protein denaturation (or adsorption of denatured proteins) compared to the more hydrophobic milled sample and leads to the relatively lower increase in shear strength upon protein adsorption. The melt sample also exhibited almost twice the elastic modulus and hardness of the milled sample, which is also indicative of increased crystallinity [34]. As a result, the milled sample exhibited a 300% increase in the shear strength values compared to the melt sample which

showed a 100% increase. The data therefore suggest that controlling the crystallinity of UHMWPE can affect its surface tribological and mechanical behavior.

Surface topography (roughness) can affect the lateral (friction) force response measured using an atomic force microscope [41]. This is especially true in the case of sharp changes in topography and an order of magnitude difference in roughness levels. The difference in roughness levels between the milled and melt sample (Table 1) is quite small. Protein adsorption also did not cause any significant change in topography or roughness of the samples. Hence it is reasonable to assume the observed differences in friction force were caused by material-based effects (at the surface) rather than topography or roughness. Residual stresses (such as the compressive stresses imparted by milling) may also have a role in the protein adsorption mechanism and observed interfacial shear strength behavior and warrants further investigation.

4.5 Conclusions

This paper studied the effect of protein adsorption on the friction response of UHMWPE subjected to two different surface treatments (milling and melting). Both the samples showed increase in the friction response and interfacial shear strength upon exposure to bovine serum albumin (BSA) proteins. The increase in frictional response of UHMWPE upon exposure to BSA is attributed to the formation of an adsorbed layer of denatured proteins on the surface. The results indicate that changing the surface energy of the sample affects the adsorption mechanism and hence the magnitudes of the resulting increase in

friction response. Changing the crystallinity of UHMWPE can affect its surface energy and friction behavior.

References

[1] A.O. El-Warrak, M.L. Olmstead, B. von Rechenberg and J.A. Auer, Veterinary and Comparative Orthopaedics and Traumatology 14 (2001) 115.

[2] E. Ingham and J. Fisher, Proceedings of the Institution of Mechanical Engineers Part H-Journal of Engineering in Medicine 214 (2000) 21.

[3] M.A. McGee, D.W. Howie, K. Costi, D.R. Haynes, C.I. Wildenauer, M.J. Pearcy and J.D. McLean, Wear 241 (2000) 158.

[4] P.A. Revell, N. Alsaffar and A. Kobayashi, Proceedings of the Institution of Mechanical Engineers Part H-Journal of Engineering in Medicine 211 (1997) 187.

[5] C.K. Hebert, R.E. Williams, R.S. Levy and R.L. Barrack, Clinical orthopaedics and related research (1996) 140.

[6] T. Dixon, M. Shaw, S. Ebrahim and P. Dieppe, Annals of the rheumatic diseases 63 (2004) 825.

[7] C. Mehrotra, L. Remington Patrick, S. Naimi Timothy, W. Washington and R. Miller, Public health reports (Washington, DC : 1974) 120 (2005) 278.

[8] J. Charnley, Journal of Bone and Joint Surgery-British Volume 42 (1960) 28.

[9] B. Cales, Clinical Orthopaedics and Related Research (2000) 94.

[10] K.S. Katti, Colloids and Surfaces B-Biointerfaces 39 (2004) 133.

[11] G. Willmann, Orthopedics 21 (1998) 173.

[12] M. Chandrasekaran and N.L. Loh, Wear 250 (2001) 237.

[13] D. Mazzucco and M. Spector, Clinical Orthopaedics and Related Research (2004) 17.

[14] Y. Nakanishi, T. Murakami, H. Higaki and H. Miyagawa, JSME International Journal, Series C: Mechanical Systems, Machine Elements and Manufacturing 42 (1999) 481.

[15] Y. Sawae, T. Murakami and J. Chen, Wear 216 (1998) 213.

[16] D.A. Swann, Bulletin de la Societe belge d'ophtalmologie 223 Pt 1 (1987) 59.

[17] M.R. Widmer, M. Heuberger, J. Voros and N.D. Spencer, Tribology Letters 10 (2001) 111.

[18] M.P. Heuberger, M.R. Widmer, E. Zobeley, R. Glockshuber and N.D. Spencer, Biomaterials 26 (2005) 1165.

[19] S.M. Kurtz, O.K. Muratoglu, M. Evans and A.A. Edidin, Biomaterials 20 (1999) 1659.

[20] A. Bellare and R.E. Cohen, Biomaterials 17 (1996) 2325.

[21] S.P. Ho, L. Riester, M. Drews, T. Boland and M. LaBerge, Proceedings of the Institution of Mechanical Engineers Part H-Journal of Engineering in Medicine 217 (2003) 357.

[22] M. Enachescu, R.J.A. van den Oetelaar, R.W. Carpick, D.F. Ogletree, C.F.J. Flipse and M. Salmeron, Physical Review Letters 81 (1998) 1877.

[23] A. Torii, M. Sasaki, K. Hane and S. Okuma, Measurement Science & Technology 7 (1996) 179.

[24] B. Bhushan, Handbook of micro/nano tribology, 2nd ed Ed.(CRC Press, Boca Raton, 1999).

[25] J.-A. Ruan and B. Bhushan, Journal of Tribology 116 (1994) 378.

[26] W.C. Oliver and G.M. Pharr, Journal of Materials Research 7 (1992) 1564.

[27] M.B. Turell and A. Bellare, Biomaterials 25 (2004) 3389.

[28] R.W. Carpick and M. Salmeron, Chemical Reviews 97 (1997) 1163.

[29] R.W. Carpick, D.F. Ogletree and M. Salmeron, Journal of Colloid and Interface Science 211 (1999) 395.

[30] K.L. Johnson, K. Kendall and A.D. Roberts, Proceedings of the Royal Society of London Series a-Mathematical and Physical Sciences 324 (1971) 301.

[31] B.V. Derjaguin, V.M. Muller and Y.P. Toporov, Journal of Colloid and Interface Science 53 (1975) 314.

[32] D. Maugis, Journal of Colloid and Interface Science 150 (1992) 243.

[33] K.D. Park, J. Kim, S.J. Yang, A. Yao and J.B. Park, Journal of biomedical materials research, Part B: Applied Biomaterials 65B (2003) 272.

[34] D.H. Gracias and G.A. Somorjai, Macromolecules 31 (1998) 1269.

[35] W. Norde and C.E. Giacomelli, Journal of Biotechnology 79 (2000) 259.

[36] P. Ying, Y. Yu, G. Jin and Z. Tao, Colloids and Surfaces, B: Biointerfaces 32 (2003) 1.

[37] V.D. Good, I.C. Clarke, G.A. Gustafson, B. Downs, L. Anissian and K. Sorensen, Acta Orthopaedica Scandinavica 71 (2000) 365.

[38] J.R. Cooper, D. Dowson and J. Fisher, Clinical Materials 14 (1993) 295.

[39] M. Kernick and C. Allen, Wear 203 (1997) 537.

[40] N. Yui, Y. Suzuki, H. Mori and M. Terano, Polymer Journal 27 (1995) 614.

[41] S. Sundararajan and B. Bhushan, Journal of Applied Physics 88 (2000) 4825.

CHAPTER 5. FRICTION AND WEAR BEHAVIOR OF ULTRA-HIGH MOLECULAR WEIGHT POLYETHYLENE AS A FUNCTION OF POLYMER CRYSTALLINITY

Modified from a paper published in *Acta Biomaterialia*
2008, 4, 1401-1410
K.S. Kanaga Karuppiah, Angela L. Bruck, Sriram Sundararajan, Jun Wang, Zhiqun Lin, Zhi-Hui Xu, Xiaodong Li

5.1 Introduction

Total joint replacement (TJR) is a procedure in which osteoarthritic joints, such as the knee or hip, are surgically replaced with an artificial device (prosthesis). Researchers have estimated that the demand for TJR is expected to increase dramatically in the next 25 years [1-3]. Though these procedures are common and generally successful, the life-span of a hip TJR with UHMWPE is often limited in patients, typically only 15-20 years. Upon use, the joints can become unstable and fail from material wear [4]. In a hip prosthesis, a metallic femoral head component articulates with a polymer lined acetabular cup that is embedded into the former hip socket. Ultra-high molecular weight polyethylene (UHMWPE) paired with a metal (cobalt chrome or Titanium alloys) or ceramic (alumina or zirconia) are the most common combination of materials used in Total Hip Replacements (THR) [5-11]. Low friction and resistance to cracking make the polymer especially advantageous for enduring stresses occurring in the hip joint. However, the polymeric nature of UHMWPE makes it susceptible to wear [5], releasing tiny particles into the joint capsule, causing osteolysis which leads to aseptic loosening and eventual failure of the implant [12, 13].

Tribological properties of the articulating metal on UHMWPE surfaces in TJRs have been recognized as critical factors affecting their durability and reliability [5, 6, 8, 9, 14-16]. Specifically, the characteristics of the softer, polymeric material have become an important area of study to reduce the problem of material wear in hip replacements, without compromising its low-friction and high impact strength advantage. It has been documented that adhesive, abrasive, and fatigue are the primary mechanisms of wear in polymers [17]. Studies have shown that a polymer's resistance to wear is directly related to its mechanical properties, which have been linked to the polymer's physical morphology, such as crystallinity [18]. Energy caused by viscoelastic deformation is adsorbed by cold drawing and orientation hardening in the semicrystalline polymers, where the chains in amorphous regions disentangle, followed by the lamellar structures in crystalline regions unfolding (i.e., decrease in the number of chain folds) with tilting and slipping of the chains [18]. Hence, a higher degree of crystallinity should give higher elastic modulus, and elongation to break. Researchers have shown increase in yield strength and elastic modulus of cross-linked UHMWPE with an increase in crystallinity [6, 7]. Kang et al [5] showed that a higher degree of crystallinity in cross-linked UHMWPE resulted in higher tensile strength with lower creep deflection, but also higher wear rate. Increases in elastic modulus, yield strength, as well as microhardness have also been established through increasing crystallinity in UHMWPE independent of cross-linking [12]. Studies compared mechanical properties of virgin, rod-stock UHMWPE to a pressure-induced high crystallinity UHMWPE, called Hylamer™, without the effects of cross-linking and confirmed higher mechanical properties such as yield stress and elastic modulus corresponded to higher crystallinity; however, this material did not

show significantly higher wear resistance [5]. The relationships between friction, wear, and crystallinity remain unclear. Thermal processing affects the morphology, crystallinity and mechanical properties of a polymer, all of which can affect its tribological performance [19, 20]. Understanding how morphology and crystallinity affect friction and wear behavior should prove useful in the pursuit of developing a superior joint material.

The objective of this study is to measure the tribomechanical properties of medical grade UHMWPE as a function of crystallinity at both the microscale and nanoscale. Adjusting thermal treatment between two similar polymer samples gives the variance in crystallinity that is needed for the study. All other processing methods are carefully controlled so that conclusions drawn can be directly correlated with the difference in degree of crystallinity between the samples.

5.2 Materials and Methods

5.2.1 Materials

Commercially available, ram extruded GUR 1050, rod-stock; medical grade UHMWPE (Poly Hi Solidur, Fort Wayne, Indiana) was cut into two 30 x 30 mm^2 square pieces, 2 mm thick. Samples were soaked in methanol and held in an ultra-sonic bath for over an hour to remove any residue. They were then air-dried with nitrogen. Differential Scanning Calorimetry (DSC) gave a peak melt transition temperature of 140 ^{0}C for rod-stock UHMWPE. Samples were separately heated in a vacuum oven (Isotemp Vacuum Oven, model 285A, Fisher Scientific) to 200 ^{0}C and held at this temperature for 3 hours to ensure thorough melting of each sample. After melting the first sample, the oven temperature was

reduced to 110 ^{0}C, the recrystallization temperature, where the sample remained for 48 hours in order to allow chains of PE to fold and form crystalline lamellae. After melting, the second sample was rapidly quenched by a liquid nitrogen quench to minimize recrystallization. Both samples were clamped with low pressure against a clean quartz plate while heating to impart low, consistent surface roughness. Prior to all friction and wear tests, UHMWPE samples were rinsed with methanol and blow-dried with nitrogen.

5.2.2 Differential Scanning Calorimetry (DSC)

A Perkin-Elmer DSC (Pyris 1) was used to characterize the melting point and percentage crystallinity of the polymer samples after thermal treatment. 10 mg of the sample was used for all DSC runs. The samples underwent a heating cycle from room temperature to 200 ^{0}C at a rate of 10 ^{0}C/min and also a cooling cycle from 200 ^{0}C to room temperature at a rate of 10 ^{0}C/min. The melting point was calculated from the crossover point of the tangents drawn to the horizontal and vertical portion of the melting peak. The percentage of crystallinity was calculated from the ratio of the area under the melting peak to the enthalpy of melting of a 100 % crystalline sample—291 J/g [21].

5.2.3 Nanoindentation

Nanoindentation was performed on the UHMWPE samples with a Berkovich indenter using a Hysitron Triboscope (Hysitron Inc., Minneapolis, Minnesota, USA) in conjunction with an Atomic Force Microscope (NanoScope Dimension^{TM} 3100, Digital Instruments, Veeco Metrology Group). Two different loading profiles were used for the test. One was a

trapezoidal loading profile with a peak indentation force of 25 μN (loading time 2.5 seconds, holding time 1 second, and unloading time 0.5 second, respectively). The other was a partial loading and unloading profile with an equal loading and unloading rate of 10 μN/s and ten different peak indentation loads ranging from 5 to 50 μN. During indentation tests, the sample was held firmly on the vacuum chuck of the AFM. The mechanical properties, namely hardness and elastic modulus, were analyzed from the unloading curve of nanoindentation using the Oliver and Pharr method [22]. A common Poisson's ratio 0.36 of polymer was used to calculate the elastic modulus.

5.2.4 Microtribometer

Microscale friction was obtained using a custom-built reciprocating microtribometer. Four ball-on-flat tests were conducted on each sample using a smooth, spherical Si_3N_4 probe (radius ~ 1.2 mm) (Figure 1) over a single stroke (length 20 mm) at a rate of 1 mm per second with a linear increase in the normal load (0 – 200 mN).

Reciprocating wear tests were completed on each sample using the microtribometer and a smooth, spherical Si_3N_4 probe of radius ~ 1.2 mm (Figure 1) in controlled low humidity (<15 % RH). A 125 mN constant normal load was applied to the samples for one thousand cycles of 20 mm stroke lengths at a speed of 5 mm per second. A dry scratch test was preformed using a conical diamond probe (radius ~ 100 μm) over a single stroke (length 20 mm) at 1 mm per second with a linear increase in normal load (0 – 750 mN). A profilometer was used to measure depth and width of the tracks from all wear tests.

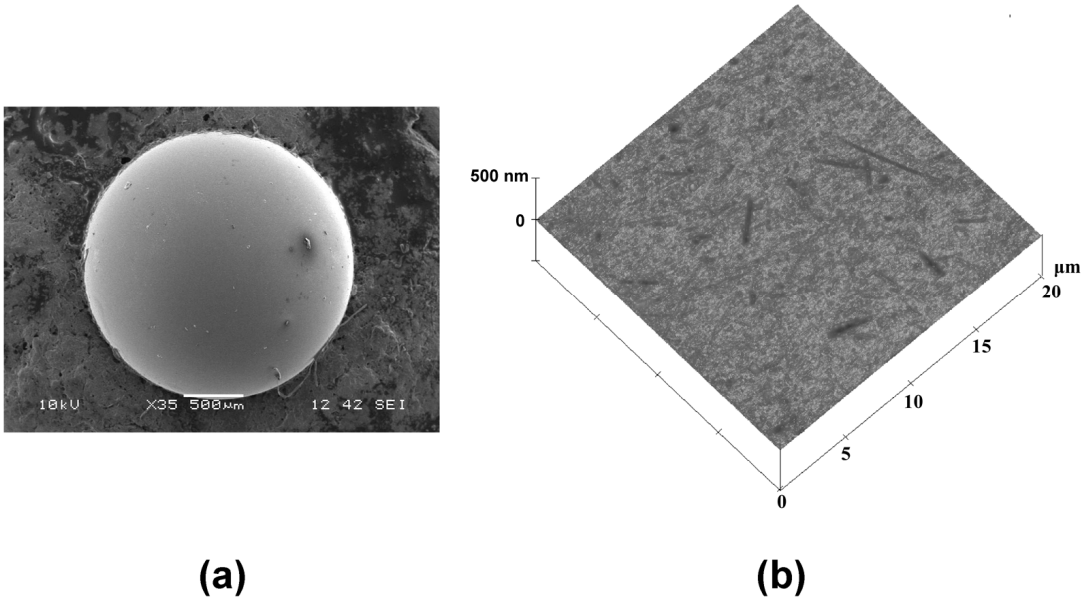

Figure 1. **(a)** Scanning electron microscope (SEM) image and **(b)** 20 µm x 20 µm topography map of spherical Si_3N_4 probe used for tribometer experiments.

5.2.5 Atomic Force Microscopy (AFM)

Since the crystalline and amorphous regions were actually in the range of nanometers, AFM was used to look at the effect of lamellar structure on the tribological properties. Experiments in contact mode were carried out with a Dimension ^{TM} 3100 AFM (Nanoscope IV, Veeco Instruments, Santa Barbara, CA) in controlled low humidity (6 ± 2 % RH) conditions to minimize effects of adsorbed water vapor. Standard V-shaped silicon nitride probes from Veeco with a quoted normal spring constant of 0.58 N/m and tip radius of 10-40 nm were used. The normal spring constant of the cantilever used was calibrated to have an actual value of 0.35 N/m using the reference lever method [23]. In order to do a comparison across the scales, we have ensured similar contact conditions and experimental conditions.

Friction force data presented are averages of five measurements at multiple sample locations. The friction force was calibrated using Ruan and Bhushan's method [24]. The radius of the tip was characterized before and after the experiments using a commercially available tip characterizer sample TGT01 (Mikromasch). The images were analyzed using SPIP software (Image Metrology) to calculate the tip radius. The tip profiles were generated using a MATLAB code.

5.2.6 Scanning Electron Microscopy (SEM)

A JEOL JSM-606LV scanning electron microscope was used to image the microtribometer wear tracks from both the cyclic wear and the scratch tests. The sample chamber was low-vacuum and accelerating voltages of 1-2 kV at ranges of 10-200x magnification were used. These images were used to measure wear widths and scratch lengths. SEM was also used to image the Si_3N_4 probes to confirm a spherical shape (Figure 1) and to check for polymer film transfer after reciprocating wear tests. A conductive, gold layer (~ 200 Å thick) was sputter-coated onto the probes before imaging. Low accelerating voltage, 1-2 kV, was used.

5.2.7 Optical Microscopy

An Olympus BX51WI (Leeds Precision Instruments, Inc.) Twin Epi-Flourescence Optical Pathway (Prairie Technologies) microscope was used to image the wear tracks from the diamond probe scratch test.

5.3 Results

The sample held at 110 ^{0}C for 48 hrs showed a degree of crystallinity of 55.1 % and a melting temperature of 140 °C. The sample which was immediately quenched in liquid nitrogen had 45.6 % crystallinity and a melting temperature of 135 °C. This data indicate that the first sample resulted in a higher degree of crystallinity. Crystallinity measurements were performed on top surface layer (<0.5 mm), intermediate layer and the core of the sample.

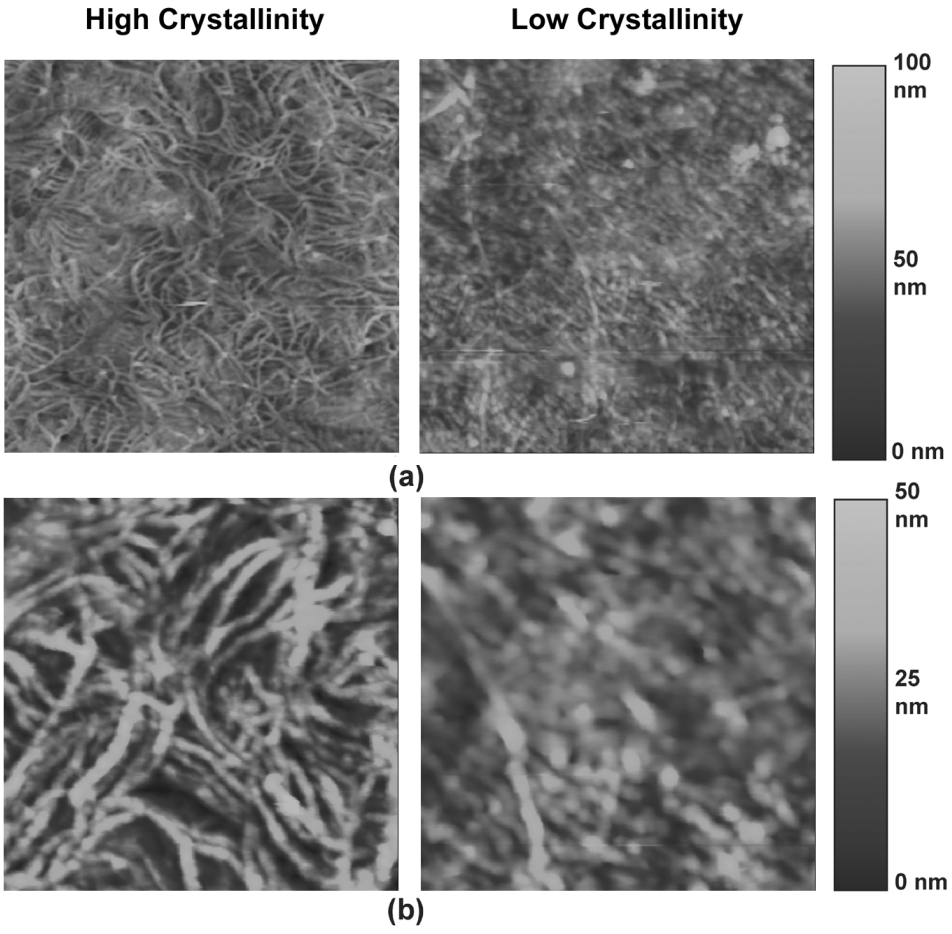

Figure 2. Topography maps of high crystallinity and low crystallinity samples at **(a)** 5 μm X 5 μm and **(b)** 1 μm X 1 μm scan sizes obtained using an AFM.

They showed no significant variation in the crystallinity values. Topography images of both samples were taken using the AFM and are shown in Figure 2. The surface of the higher crystallinity (HC-PE) sample displayed a distinct lamellar type of structure that is indicative of crystalline regions in semicrystalline polymers [9]. The lower crystallinity (LC-PE) sample did not display a comparable lamellar structure at this scale for the given imaging conditions. We note that LC-PE may have a thinner lamellar structure that is not well-resolved by our AFM imaging. For the purposes of this study, we therefore assumed based on our observations that the lamellae are relatively thicker and evident on the HC-PE than on the LC-PE. We note that by using permanganic acid etching [25], one could improve the resolution of thin lamellae. The final surface root-mean square roughness (*RMS* roughness) of the HC-PE and LC-PE samples were 4.58 ± 0.18 nm and 3.18 ± 0.18 nm (1 μm x 1 μm scan) respectively, as measured using the AFM. The difference in roughness levels between the two samples is small and, hence, can be considered to have negligible impact on the observed difference in the tribological behavior at either scale. Physical parameters of UHMWPE as a function of crystallinity are shown in Table 1.

Figure 3 (a) shows the typical load penetration depth curves of nanoindentation tests on two UHMWPE samples with different crystallinity using the same trapezoidal loading profile with nominal peak indentation force of 25 μN. Indentation on the HC-PE has a higher peak load and shallower penetration depth compared with the LC-PE sample. The average elastic modulus and hardness of five indentations for the two samples are listed in Table 1. Clearly, the HC-PE has a higher elastic modulus and hardness than LC-PE. We note that the

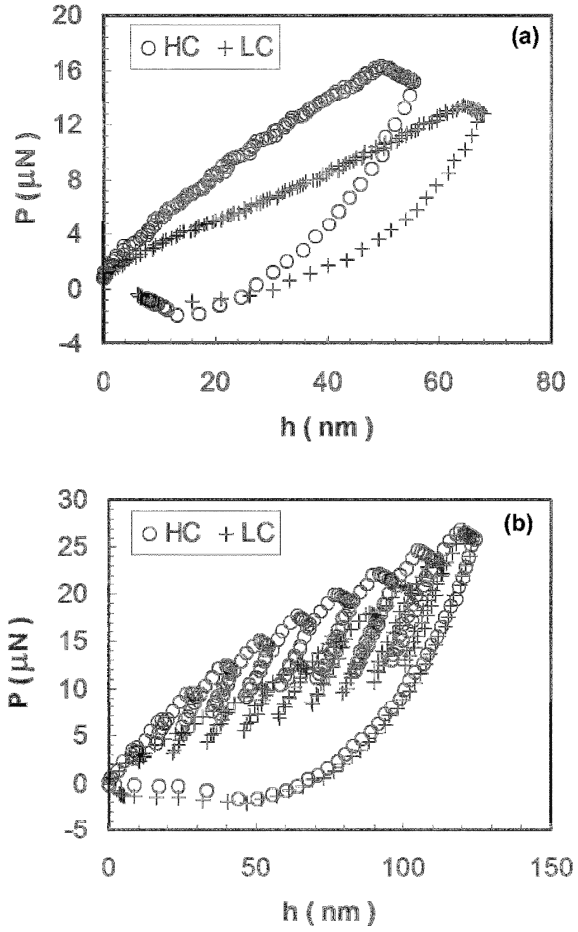

Figure 3. Load-penetration depth (P-h) curves from nanoindentation tests on both low crystallinity and high crystallinity samples with trapezoidal loading profile **(a)** and partial loading and unloading profile **(b)**.

maximum penetration depths for nanoindentations on both samples are over 10 times deeper than the surface roughness, thus negating any roughness effects on the results. Figure 3 (b) shows the typical load penetration depth curves of nanoindentation tests with partial loading and unloading profile with nominal peak indentation forces ranging from 5-50 μN. The

Table 1. Summary of physical parameters of UHMWPE as a function of crystallinity

Sample	Crystallinity %	RMS surface roughness (nm)	Elastic Modulus[a] (GPa)	Hardness[a] (GPa)
HC-PE	55.1	4.58 ± 0.18	2.42 ± 0.014	0.25 ± 0.03
LC-PE	45.6	3.18 ± 0.18	1.71 ± 0.03	0.14 ± 0.004

[a]Measured using nanoindentation at a peak load of 25 μN.

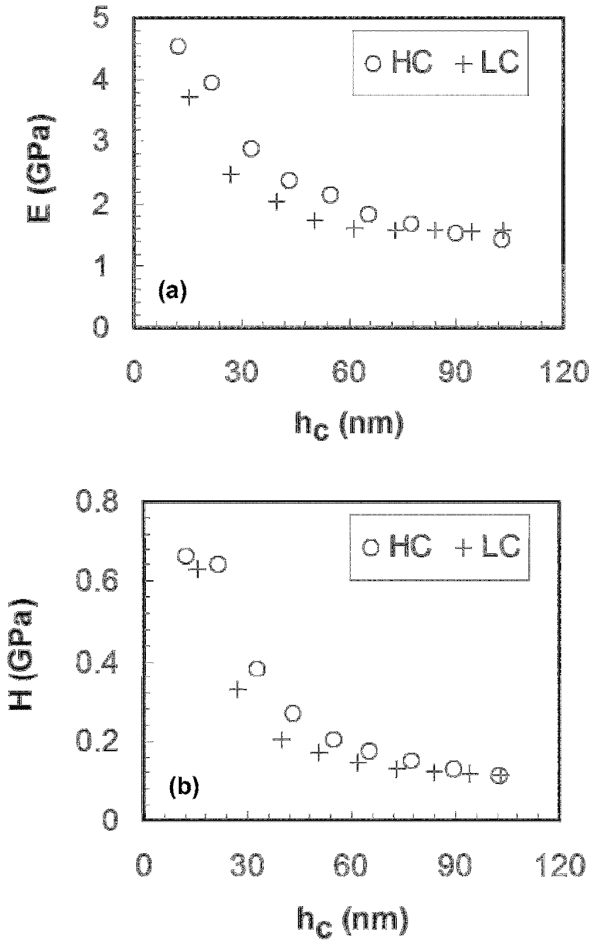

Figure 4. Elastic modulus (*E*) **(a)** and **(b)** hardness (*H*) as a function of indentation contact depth (h_c).

elastic modulus and hardness are determined from the partial unloading curves at different peak loads. The variations of average elastic modulus and hardness with the average indentation contact depth of five indentations for the two UHMWPE samples are shown in Figure 4. As can be seen, both elastic modulus and hardness of HC-PE and LC-PE decrease with an increase of the indentation contact depth. For contact depth less than 80 nm, the elastic modulus and hardness of HC-PE are higher than LC-PE. For contact depth larger than 80 nm, both samples give almost the same elastic modulus and hardness. For accurate determination mechanical properties of polymeric and viscoelastic materials using nanoindentation test, the creep effect, which often results in bulging "nose" in the unloading curve, must be accounted for before applying Oliver and Pharr method. This can be done by either introducing a sufficiently long holding segment [26] or using a sufficiently fast unloading rate [27]. In this study, both appropriate holding segment and fast unloading rate have been employed to reduce the creep effect on the measured mechanical properties. No bulging "nose" is observed in the nanoindentation unloading curves, which indicates that creep effect has been effectively eliminated.

The friction responses of the UHMWPE at the microscale and nanoscale are shown in Figure 5. For both of the samples across scales the friction force increased with an increase in normal load. The data indicates that HC-PE results in a lower friction response than LC-PE at both the micro and nanoscale.

Optical microscopy showed that the friction experiments completed with the Si_3N_4 probe on the tribometer had no visible wear prior to 75 mN on either sample. Friction coefficients for each sample at the microscale were calculated for two regions, before and

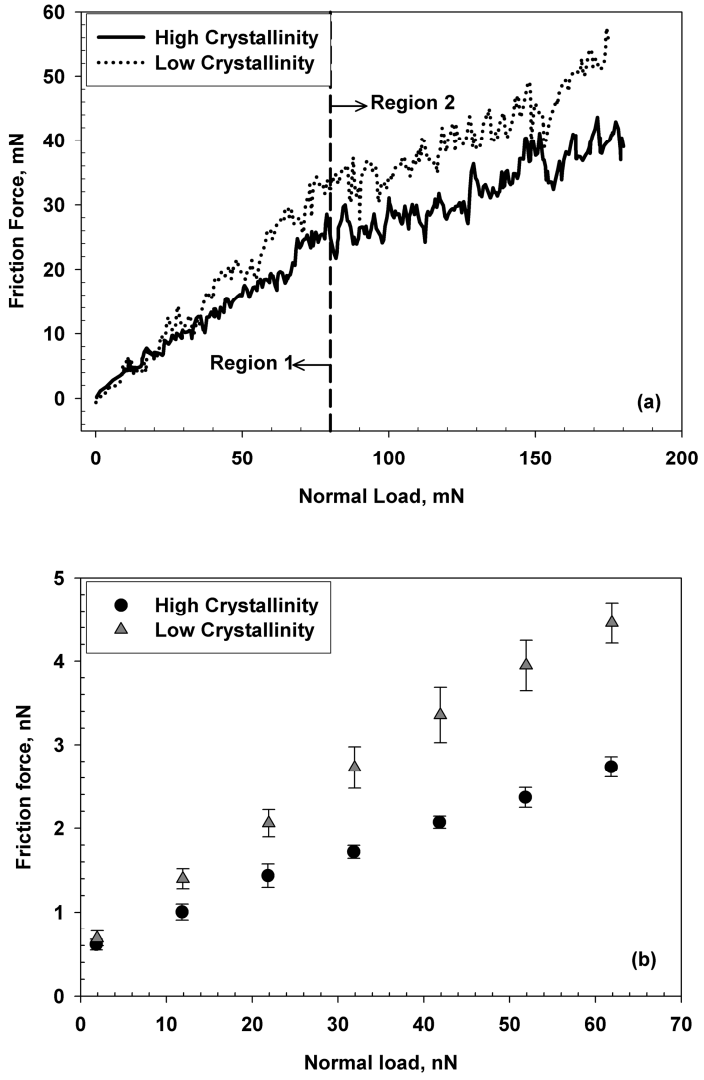

Figure 5. **(a)** Microscale (tribometer) and **(b)** nanoscale (AFM) friction response as a function of normal load for both the high crystallinity and low crystallinity samples. Friction response is higher for the low crystallinity sample in both cases.

after the observed onset of damage, as shown in Figure 5a. Linear fits in region 1 showed friction coefficients for HC-PE and LC-PE to be 0.31 and 0.42, respectively. Fits from region 2 gave a coefficient of 0.17 for HC-PE and 0.23 for LC-PE. Four such measurements

were taken on each sample and an average value of the coefficient of friction is reported in table 2. For the AFM friction experiments, no discernable wear was observed up to loads of 60 nN. Friction increased with increase in normal load in a slightly non-linear fashion. This non-linearity is attributed to the contact area dependence of friction that is observed in AFM experiments at the nanoscale [14, 28, 29]. In the absence of wear, the mechanism in AFM experiments can be assumed to be adhesive in nature. The adhesive friction is then given by [30]

$$F = \tau_0 A_r + \beta L \quad (1)$$

where τ_0 is the interfacial shear strength, A_r is the real area of contact, β is a factor for friction

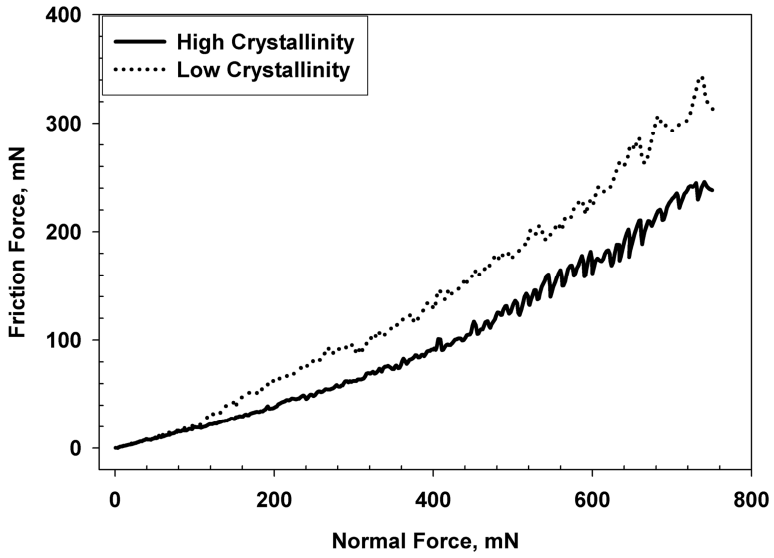

Figure 6. Microscale (tribometer) friction response of UHMWPE using a diamond probe as a function of normal load for both the high crystallinity and low crystallinity samples. Friction response is higher for the low crystallinity sample.

Table 2. Summary of friction coefficients and wear measurements as a function of UHMWPE crystallinity

Sample	Microscale Coefficient of friction (before damage)[a]	Microscale Coefficient of friction (after damage)[a]	Interfacial Shear Strength (MPa)[b]	β[b]	Wear depth[c] (μm)	Wear width[c] (μm)	Scratch depth[d] (μm)	Scratch width[d] (μm)	Scratch depth[e] (nm)
HC-PE	0.28 ± 0.02	0.15 ± 0.02	8.27	0.0098	0.12 ± .030	85.0 ± 5.9	0.46 ± .01	85.2 ± .01	3.98 ± .99
LC-PE	0.39 ± 0.03	0.22 ± 0.01	7.13	0.036	0.21 ± .016	113.5 ± 9.3	0.52 ± .01	102.3 ± .01	6.55 ± .37

[a]Measured using a Si_3N_4 probe on the microtribometer over a normal load range of 0 to 180 mN.
[b]Calculated from fit of equation 1 (according to DMT contact mechanics) to AFM data in Figure 5.
[c]Measured using a Si_3N_4 probe on the microtribometer for 1000 reciprocating, 20 mm cycles at an applied load of 125 mN.
[d]Abrasive wear using a diamond probe on the tribometer for a 0-750 mN ramped-load scratch test. Depth measurements shown represent those at maximum load, 750 mN.
[e]Measured using AFM at a normal load of 80 nN and 40 cycles.

dependency on the applied normal load, L. In order to determine the appropriate contact mechanics theory to be employed for A_r, the Tabor parameter was calculated. Based on the Tabor parameter values (HC-PE – 0.82 and LC-PE – 1.03), Derjaguin-Muller-Toporov (DMT) [31] model was chosen to be appropriate. Upon fitting equation 1 to the plots shown in Figure 5, τ_0 and β were calculated and are tabulated in Table 2. HC-PE showed higher interfacial shear strength than LC-PE.

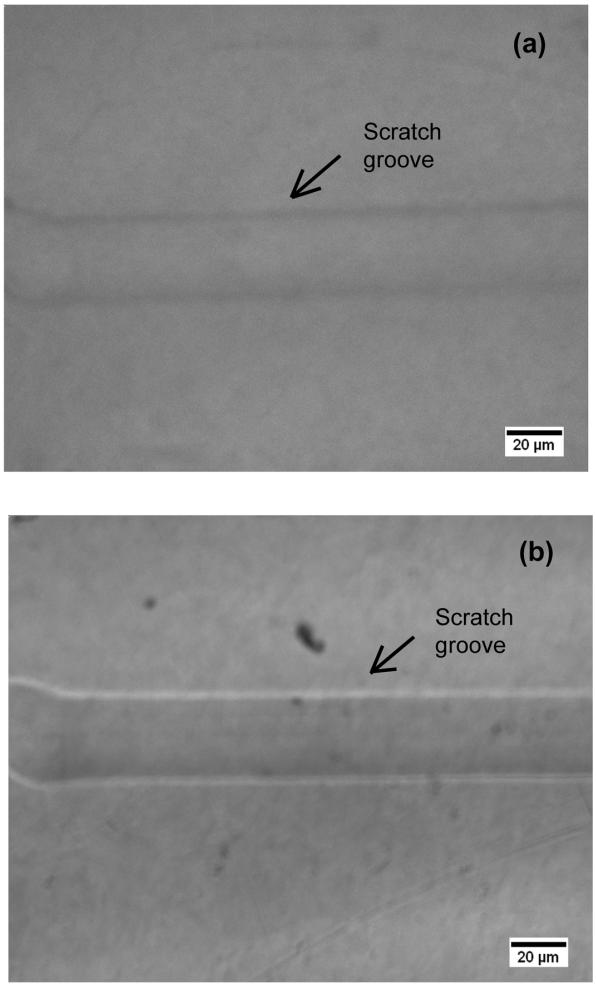

Figure 7. Optical images of dry scratch tests with diamond probe preformed with the microtribometer on **(a)** high crystallinity and **(b)** low crystallinity.

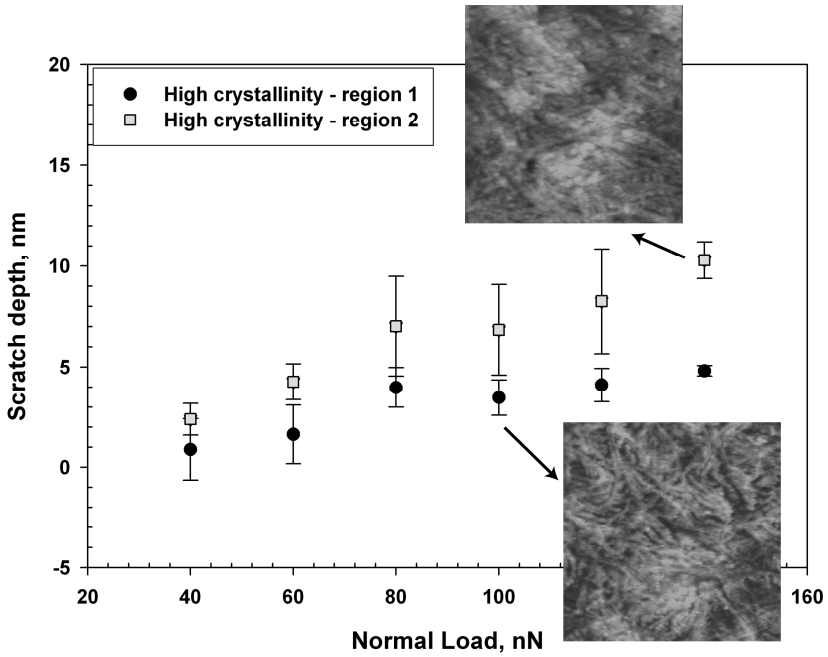

Figure 8. AFM scale scratch depth measurements on two different regions of HC-PE. Region 1 corresponds to HC-PE showing a qualitatively more defined crystalline lamellar structure than region 2.

Microscale ramped-load scratch tests using the diamond probe caused damage in the early stages of the tests for both samples. For both samples, the rate of friction response to normal load was non-linear as shown in Figure 6, corresponding to deeper probe penetration into the sample at higher loads. Using an optical microscope and SEM the damage onset for the LC-PE sample occurred at lower normal load (between 50-70 mN) than for the HC-PE sample (between 90-100 mN). LC-PE exhibited higher scratch depth at all applied normal loads, as was measured with a profilometer. The scratch depth and width at the maximum load of 750 mN (Figure 7) were measured on both samples and are reported in Table 2 below. The LC-PE sample exhibited a scratch depth that was about 100 nm larger than that

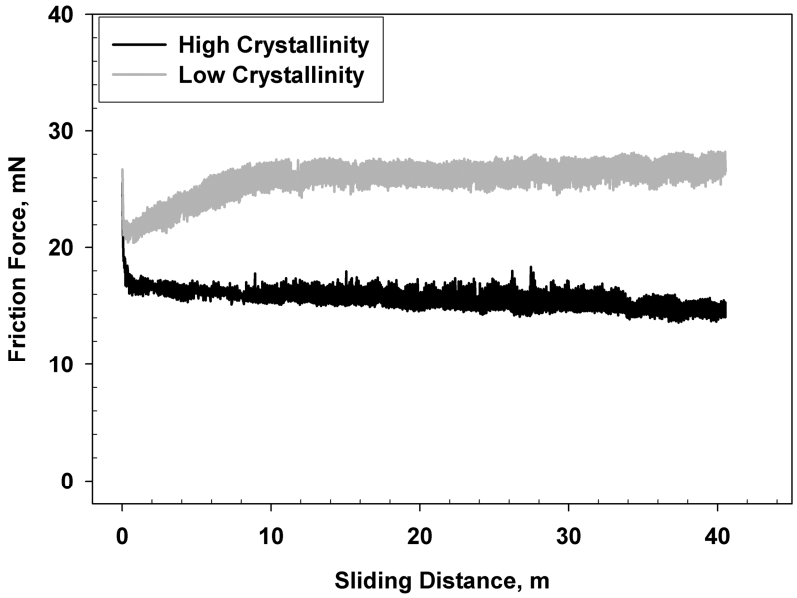

Figure 9. Microscale (tribometer) friction response of Si_3N_4 probe (radius ~1.2mm) on high crystallinity and low crystallinity samples and a function of sliding distance in a dry, reciprocating wear test with a constant load of 125 mN

of the HC-PE sample. In the case of AFM scratch tests, LC-PE exhibited higher scratch depth than HC-PE at all applied normal loads at certain locations and comparable scratch depths in other locations as shown in Figure 8. This was attributed to a variance in lamellar structure at the surface (inset of Figure 8). Since, UHMWPE is a semicrystalline polymer, there were certain regions where the lamellar structure was pronounced and other regions where it was not so pronounced for the given imaging conditions. In the latter regions, the scratch depths of HC-PE were comparable to the LC-PE. This suggests that at the scale of the AFM tests, the observed wear resistance is directly proportional to the degree of lamellar

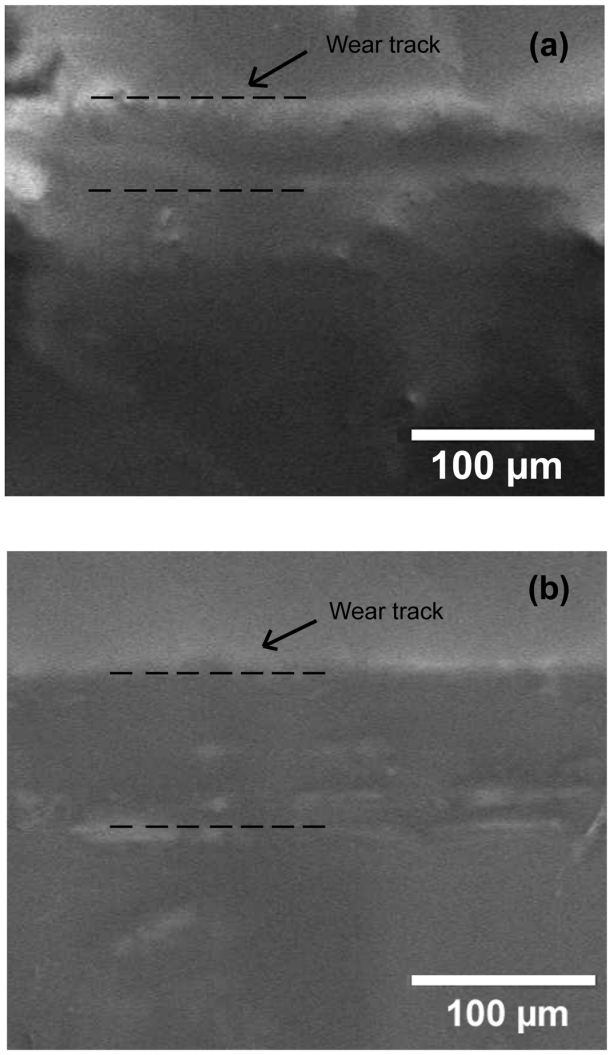

Figure 10. SEM images of tracks from reciprocating wear tests with Si_3N_4 probe (radius ~1.2mm) performed using the microtribometer on **(a)** high crystallinity and **(b)** low crystallinity.

structure at the surface. It also suggests that the thermal processing employed does not create a uniform lamellar structure in the case of the HC sample.

The dry-sliding, reciprocating wear test performed using the microtribometer with a spherical Si_3N_4 probe showed the LC-PE friction response to level-off at around 27 mN compared to the lower friction response of HC-PE, which leveled-off at about 15 mN (Figure 9). The profilometer revealed wear depth measurements of 0.21 ± .016 μm and 0.12 ± .030 μm, respectively. These are consistent with the LC-PE exhibiting more damage than the HC-PE. SEM images of the wear tracks are shown in Figure 10. SEM images of the probes taken after wear tests revealed no polymer film transfer. The results of the tribological tests are summarized in Table 2. The data shows that the wear resistance of UHMWPE increases with an increase in crystallinity, resulting in higher hardness and elastic modulus [32], hence, enhanced resistance to surface damage.

5.4 Discussion

After completing DSC, the thermal treatment performed proved to be effective in controlling differences in crystallinity. Turell et al observed that at the nanoscale, lamellar structure of semicrystalline UHMWPE can be identified [9]. In a comparison between images of the slowly cooled and nitrogen quenched samples, the lamellar morphology is much more apparent in the former sample. Turell pointed out that the size of lamellae is increased with slow cooling and annealing, and decreased by quenching, which accounts for the differences in detail of the crystalline structures. In the present study, AFM images confirm that the UHMWPE samples indeed display different crystalline morphology, and that the slowly cooled (and predicted higher crystallinity) sample demonstrated a more evident presence of lamellae. As anticipated, the slowly cooled sample resulted in a higher degree of

crystalline volume and the quenched sample came out with a significantly lower crystalline volume. Rod-stock control UHMWPE and methods of high compression moulding [20] and annealing [6] of the polymer below its melting temperature have proven to prepare samples with crystallinities as high as 60-75%. However, in order to control the surface roughness parameter, it was necessary in the current study to melt the UHMWPE samples to eliminate variations from milling effects.

Mechanical properties of semicrystalline polymers depend on many variables, including the degree of crystallinity and operating temperature [18]. Results of nanoindentation show a 41.5 % higher elastic modulus and a 78.6 % higher hardness value for HC-PE over LC-PE. The lower wear of HC-PE in cyclic and abrasive scratch tests can be linked to higher mechanical properties, hence increased wear resistance.

HC-PE showed a slightly lower coefficient of friction than LC-PE. Ho et al. observed similar correlation on UHMWPE and suggested that the increase in coefficient of friction with decreased crystallinity could be due to the decreased storage modulus caused by the decreased crystallinity [20]. Friction responses of the diamond scratch test performed by the microtribometer indicate that as wear depth increases, coefficient of friction will increase as well. LC-PE experienced a higher friction response than HC-PE, corresponding with deeper wear tracks. Wear profiles of diamond scratching on each sample revealed ploughed grooves and lipped edges characteristic of deformation from abrasive wear. SEM images confirm the occurrence of ribbon-like debris that is often observed in the case of abrasive wear on the low crystallinity sample (Figure 11).

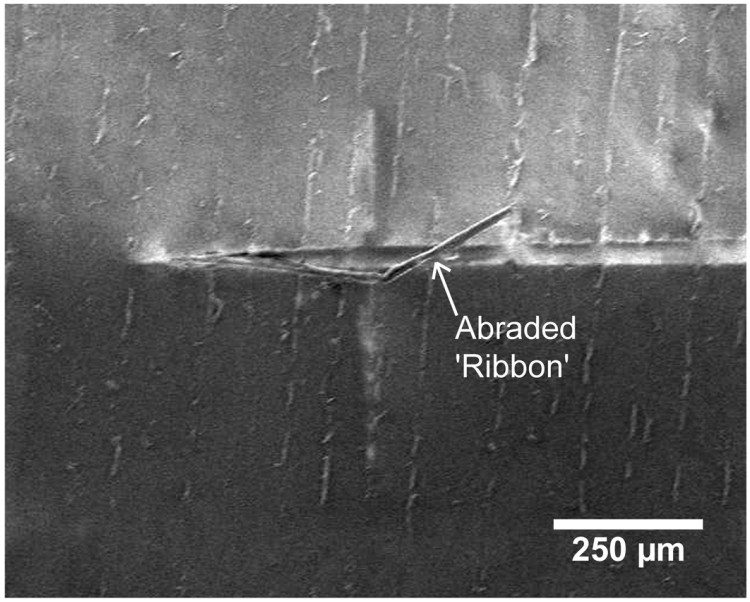

Figure 11. SEM image of wear ribboning occurring on the low crystallinity sample at the initial onset of deformation during scratch test with diamond probe.

During reciprocating wear after the initial static friction response, friction dropped dramatically for both samples as shown in Figure 9. In the case of the LC-PE sample, the friction response increased until the sliding distance reached about 10 m, at which point the friction response appeared to level-off at around 27 mN. It can be expected that the probe continued to groove the sample until it reached a maximum level of deformation at that load, causing friction to become nearly steady. Friction response of HC-PE only showed a decreasing trend, even with the occurrence of plastic deformation. Though the plot seems to level-off at around 15 mN, a slight downward slope remains, even after 1000 cycles.

Wear depths showed that LC-PE had deeper tracks than HC-PE, indicating that that higher crystallinity is more resistance to wear from fatigue mechanisms. Kang et al [5] also showed lower microscale wear of a slowly cooled, higher crystalline sample of cross-linked

UHMWPE compared to a quenched sample, attributed to the formation of larger lamellae and mechanical reinforcement. Comparing the effects of cyclic stress on the experimental samples, it is reasonable to conclude that long term stress on a higher crystallinity UHMWPE cup lining would lead to less friction *in vivo* than that of a lower crystallinity lining.

5.5 Conclusions

The results indicate that increasing the surface crystallinity of UHMWPE decreases the friction response of the polymer at both the microscale and nanoscale, even for the small difference in crystallinity achieved between our samples. Increased crystallinity also resulted in an increase in scratch and wear resistance which is attributed to increase in hardness and elastic modulus. On the nanoscale, the degree of lamellar structure appeared to affect the observed wear resistance, with the wear resistance being higher in regions of more pronounced lamellae than in less pronounced regions. Although the experiments were performed in air, this study suggests that increasing the crystallinity of UHMWPE may be beneficial to the durability of a total joint replacement that uses this polymer. Evaluation of wear behavior as a function of polymer crystallinity in the presence of a lubricating medium is currently being conducted.

References

[1] Dixon T, Shaw M, Ebrahim S, Dieppe P. Trends in hip and knee joint replacement: socioeconomic inequalities and projections of need. Annals of the Rheumatic Diseases 2004;63:825-830.

[2] Kurtz S, Mowat F, Ong K, Chan N, Lau E, Halpern M. Prevalence of primary and revision total hip and knee arthroplasty in the United States from 1990 through 2002. Journal of Bone and Joint Surgery-American Volume 2005;87A:1487-1497.

[3] Mehrotra C, Remington PL, Naimi TS, Washington W, Miller R. Trends in total knee replacement surgeries and implications for public health, 1990-2000. Public Health Reports 2005;120:278-282.

[4] Bradford L, Baker DA, Graham J, Chawan A, Ries MD, Pruitt LA. Wear and surface cracking in early retrieved highly cross-linked polyethylene acetabular liners. Journal of Bone and Joint Surgery-American Volume 2004;86A:1271-1282.

[5] Kang PH, Nho YC. The effect of gamma-irradiation on ultra-high molecular weight polyethylene recrystallized under different cooling conditions. Radiation Physics and Chemistry 2001;60:79-87.

[6] Bergstrom JS, Rimnac CM, Kurtz SM. Prediction of multiaxial mechanical behavior for conventional and highly crosslinked UHMWPE using a hybrid constitutive model. Biomaterials 2003;24:1365-1380.

[7] Kurtz SM, Villarraga ML, Herr MP, Bergstrom JS, Rimnac CM, Edidin AA. Thermomechanical behavior of virgin and highly crosslinked ultra-high molecular weight polyethylene used in total joint replacements. Biomaterials 2002;23:3681-3697.

[8] Zhou J, Chakravartula A, Pruitt L, Komvopoulos K. Tribological and nanomechanical properties of unmodified and crosslinked ultra-high molecular weight polyethylene for total joint replacements. Journal of Tribology-Transactions of the Asme 2004;126:386-394.

[9] Turell MB, Bellare A. A study of the nanostructure and tensile properties of ultra-high molecular weight polyethylene. Biomaterials 2004;25:3389-3398.

[10] Lancaster JG, Dowson D, Isaac GH, Fisher J. The wear of ultra-high molecular weight polyethylene sliding on metallic and ceramic counterfaces representative of current femoral surfaces in joint replacement. Proceedings of the Institution of Mechanical Engineers Part H-Journal of Engineering in Medicine 1997;211:17-24.

[11] Derbyshire B, Fisher J, Dowson D, Hardaker C, Brummitt K. Comparative-study of the wear of UHMWPE with zirconia ceramic and stainless-steel femoral heads in artifical hip joints. Medical Engineering & Physics 1994;16:229-236.

[12] Simis KS, Bistolfi A, Bellare A, Pruitt LA. The combined effects of crosslinking and high crystallinity on the microstructural and mechanical properties of ultra high molecular weight polyethylene. Biomaterials 2006;27:1688-1694.

[13] Muratoglu OK, et al. Gradient crosslinking of UHMWPE using irradiation in molten state for total joint arthroplasty. Biomaterials 2002;23:717-724.

[14] Kanaga Karuppiah KS, Sundararajan S, Xu ZH, Li XD. The effect of protein adsorption on the friction behavior of ultra-high molecular weight polyethylene. Tribology Letters 2006;22:181-188.

[15] Kurtz SM, Rimnac CM, Pruitt L, Jewett CW, Goldberg V, Edidin AA. The relationship between the clinical performance and large deformation mechanical behavior of retrieved UHMWPE tibial inserts. Biomaterials 2000;21:283-291.

[16] Czel G, Zsoldos G. Acetabular cup deformation and strength improvement by physical crosslinking. Materials Science, Testing and Informatics, vol. 473-474. 2005. p.441-446.

[17] Bhushan B. Principles and Applications of Tribology. New York: John Wiley & Sons, Inc., 1999.

[18] Sperling LH. Introduction to Physical Polymer Science. Hoboken, New Jersey: John Wiley & Sons, Inc., 2006.

[19] Bellare A, Cohen RE. Morphology of rod stock and compression-moulded sheets of ultra-high-molecular-weight polyethylene used in orthopaedic implants. Biomaterials 1996;17:2325-2333.

[20] Ho SP, Joseph PF, Drews MJ, Boland T, LaBerge M. Experimental and numerical modeling of variable friction between nanoregions in conventional and crosslinked UHMWPE. Journal of Biomechanical Engineering-Transactions of the Asme 2004;126:111-119.

[21] Oral E, Malhi AS, Muratoglu OK. Mechanisms of decrease in fatigue crack propagation resistance in irradiated and melted UHMWPE. Biomaterials 2006;27:917-925.

[22] Oliver WC, Pharr GM. An Improved Technique for Determining Hardness and Elastic-Modulus Using Load and Displacement Sensing Indentation Experiments. Journal of Materials Research 1992;7:1564-1583.

[23] Torii A, Sasaki M, Hane K, Okuma S. A method for determining the spring constant of cantilevers for atomic force microscopy. Measurement Science & Technology 1996;7:179-184.

[24] Ruan JA, Bhushan B. Atomic-Scale Friction Measurements Using Friction Force Microscopy .1. General-Principles and New Measurement Techniques. Journal of Tribology-Transactions of the Asme 1994;116:378-388.

[25] Olley RH, Hosier IL, Bassett DC, Smith NG. On morphology of consolidated UHMWPE resin in hip cups. Biomaterials 1999;20:2037-2046.

[26] Briscoe BJ, Fiori L, Pelillo E. Nano-indentation of polymeric surfaces. Journal of Physics D-Applied Physics 1998;31:2395-2405.

[27] Cheng YT, Cheng CM, Ni WY. Methods of obtaining instantaneous modulus of viscoelastic solids using displacement-controlled instrumented indentation with axisymmetric indenters of arbitrary smooth profiles. Materials Science and Engineering a-Structural Materials Properties Microstructure and Processing 2006;423:2-7.

[28] Carpick RW, Agrait N, Ogletree DF, Salmeron M. Measurement of interfacial shear (friction) with an ultrahigh vacuum atomic force microscope. Journal of Vacuum Science & Technology B 1996;14:1289-1295.

[29] Enachescu M, van den Oetelaar RJA, Carpick RW, Ogletree DF, Flipse CFJ, Salmeron M. Observation of proportionality between friction and contact area at the nanometer scale. Tribology Letters 1999;7:73-78.

[30] Carpick RW, Salmeron M. Scratching the surface: Fundamental investigations of tribology with atomic force microscopy. Chemical Reviews 1997;97:1163-1194.

[31] Derjaguin BV, Muller VM, Toporov YP. Effect of Contact Deformations on Adhesion of Particles. Journal of Colloid and Interface Science 1975;53:314-326.

[32] Gracias DH, Somorjai GA. Continuum force microscopy study of the elastic modulus, hardness and friction of polyethylene and polypropylene surfaces. Macromolecules 1998;31:1269-1276.

CHAPTER 6. FRICTION AND WEAR BEHAVIOR OF ULTRA-HIGH MOLECULAR WEIGHT POLYETHYLENE AS A FUNCTION OF CRYSTALLINITY IN THE PRESENCE OF THE PHOSPHOLIPID DPPC (DIPALMITOYL PHOSPHATIDYLCHOLINE)

Modified from a paper submitted to *Journal of Biomedical Materials Research Part B*

Angela L. Bruck, K.S. Kanaga Karuppiah, Sriram Sundararajan, Jun Wang, Zhiqun Lin

6.1 Introduction

For the past forty years, ultra-high molecular weight polyethylene (UHMWPE) has been the primary material used for the articulating cup of artificial hip joints.[1-9] Its viscoelasticity, low friction, and low wear resemble properties of cartilage lining natural human joints more than any other biocompatible material. However, it has been found that polymeric wear particles from the UHMWPE in artificial hip joints have been the major factor limiting the life of an implant, causing osteolysis and loosing of the joint,[5,10] requiring revision surgery. Much attention has been on the tribological behavior of UHMWPE in an effort to reduce its wear. Many studies conducted have focused on altering the physical and chemical properties of UHMWPE to increase wear resistance, such as gamma-irradiated cross-linking [11] and orientating crystalline [12] structure, which have correlated with decreases in wear. Others have focused on the environment of the joint interface *in vivo*.

Healthy, human joints are lubricated by synovial fluid and can achieve remarkably low friction behavior, with coefficients as small as 0.002-0.006.[13,14] Synovial fluid is a complex plasma solution mostly of proteins, hyaluronic acid, and lipids and is sealed by the

joint capsule, comprising of a membrane-lined fibrous layer of connective tissue.[15] With the growing industry for total joint replacements, research to establish which constituent of the synovial fluid is responsible for the highest lubricating contribution has received growing attention. Sawae et al. compared friction of UHMWPE in the presence of albumin (major protein component of synovia) versus hyaluronic acid (HA) and found albumin caused higher friction than HA.[4] Gispert et al. also compared friction between albumin and HA, as well as a solution of albumin and HA combined. There were no consistent results as to the individual contributions to friction and lubrication, but it was clear that the combination of albumin and HA in a lubricating solution caused the lowest friction response and wear rate.[16]

Surface active phospholipids (SAPL) have been reported to act as a boundary lubricant in human joints [13,17,18] by adsorbing phosphate head groups onto the surface of the joint, and leaving fatty-acid tails to create a hydrophobic monolayer.[13] It has been shown that in osteoarthritic joints, the synovial fluid does not lubricate as well as in healthy joints [19,20] and this is often attributed to a deficiency of SAPL.[14] Investigations on the tribological influence of phospholipids on UHMWPE have correlated decreasing friction and wear in the presence of phospholipids.[21] The most abundant lipid in synovial fluid is DPPC (dipalmitoyl phosphatidylcholine), making up 45 % of the total volume weight of lipids,[18] and is one of the most common phospholipids studied on UHMWPE. DPPC dissolved in propylene glycol and ethanol on UHMWPE have shown lower friction values when compared to control lubricant without DPPC.[13] Mazzucco et al. reported a lubricant of DPPC in phosphate buffered solution (PBS) to have the lowest coefficient of friction between polyethylene and cobalt chrome surfaces, when compared to HA and protein dissolved in PBS.[21] It is

hypothesized that the presence of phospholipids between articulating surfaces would also reduce wear by reducing interfacial contact, though further studies are needed to confirm this theory.

SAPL have an affinity for hydrophilic surfaces due to their ionic phosphate heads.[13] UHMWPE is considered a hydrophobic polymer (contact angle ~80-100 degrees), which has low wettability and the potential to resist adsorption of the lipid. Gispert et al. showed a marked change in contact angle and surface tension on UHMWPE using separate solutions of saline with HA and bovine serum albumin (BSA) compared to saline alone. The presence of HA in saline increased the contact angle whereas BSA decreased the angle.[16] The effect of crystalline morphology at the surface on the water contact angle of polypropylene was examined by Yui et al. and found to correlate well: higher crystallinity at the surface gave lower contact angles, confirming that crystalline regions of polypropylene contain more surface energy than amorphous regions.[22] Molecular simulations have shown similar trend in polyethylene.[23] One potential for increasing adsorption of SAPL onto UHMWPE is to increase the crystallinity of the material. The authors have studies the effect of crystallinity on the friction and wear behavior of UHMWPE in dry conditions and found that increased crystallinity resulted in lower friction and wear.[24]

In the present study, friction and wear behavior of UHMWPE as a function of crystallinity in the presence of a DPPC-ethanol lubricant was investigated. Two UHMWPE samples with different crystallinities were made using specific thermal treatments. Friction and wear tests were done with a custom-built ball-on-flat microtribometer under separate

lubricant of a pure ethanol control and a solution of DPPC phospholipids dissolved in ethanol.

6.2 Experimental Details

6.2.1 Materials

Commercially available, ram extruded GUR 1050, rod-stock; medical grade UHMWPE (Poly Hi Solidur, Fort Wayne, Indiana) was cut into two 30 mm square pieces, 2 mm thick. Samples were soaked in methanol and held in an ultra-sonic bath for over an hour to remove any residue. They were then air-dried with nitrogen. Differential Scanning Calorimetry (DSC) gave a peak melt transition temperature of 140 ^{0}C for rod-stock UHMWPE. Two samples with significant difference in crystallinity were desired. Separately, samples were heated in a vacuum oven to 200 ^{0}C. To create a high crystallinity polymer, the first sample was held at this temperature for 3 hours to ensure thorough melting; the oven temperature was then reduced to 110 ^{0}C, the recrystallization temperature, where the sample remained for 60 hours in order to allow time for lamellar folding into a crystalline state. The second sample was held for 5 hours at 200 ^{0}C, to give sufficient time for thorough melting and disordering of the chains. After holding the second sample for 5 hours, it was rapidly cooled by a liquid nitrogen quench to freeze amorphous entanglements and minimize recrystallization. Both samples were clamped with low pressure against a clean quartz plate while heating to impart low, consistent surface roughness. All UHMWPE samples were rinsed with methanol and air-dried with nitrogen before further treatment or testing.

6.2.2 Differential Scanning Calorimetry (DSC)

A Perkin-Elmer DSC (Pyris 1) was used to characterize the melting point and percentage crystallinity of the polymer samples after thermal treatment. 10 mg of the sample was used for all DSC runs. The samples underwent a heating cycle from 25 ^{0}C to 200 ^{0}C at a rate of 10 ^{0}C/min and also a cooling cycle from 200 ^{0}C to 25 ^{0}C at a rate of 10 ^{0}C/min. The melting point was calculated from the crossover point of the tangents drawn to the horizontal and vertical portion of the melting peak. The percentage of crystallinity was calculated from the ratio of the area under the melting peak to the enthalpy of melting of a 100 % crystalline sample (291 J/g) [25]. The crystallinity values reported have a calculated uncertainty of 1.3%.

6.2.3 Phospholipids

The phospholipids used in this study were synthetic, 99% pure L–α-Phosphatidylcholine, dipalmitoyl (DPPC), P0763 by Sigma-Aldrich Chemical Company. The DPPC was dissolved into ethyl alcohol at a concentration of 0.5 mg/ml, corresponding to the approximate concentration of DPPC found in human synovial fluid.[21] Sodium azide (~ 0.01%) was added to prevent microbial growth. The liquid was then vortex mixed for 3-4 minutes and ultrasonicated for 30 minutes at a temperature of 43 °C to create a homogeneous solution. The DPPC-ethanol solution was used as a lubricant in friction and wear tests of the polymer samples; prior to lubricated tests, samples were covered and soaked in the solution for ~ 3 hours before testing. Polymer samples were also tested in pure ethanol which served as the control sample for the present study. Throughout testing, surfaces were submerged in the solution.

6.2.4 Friction and wear tests

Microscale friction was obtained using a custom-built reciprocating microtribometer in a ball-and-flat configuration. Four tests were conducted on each sample using a smooth, spherical Si_3N_4 probe (radius ~ 1.2 mm) over a single stroke (length 15 mm) at a rate of 1 mm per second with a linear increase in the normal load (0 – 200 mN). Reciprocating wear tests were completed on each sample using the microtribometer and a smooth, spherical Si_3N_4 probe (radius ~ 1.2 mm). A 140 mN constant normal load was applied to the samples for one thousand cycles of 15 mm stroke lengths at a speed of 5 mm per second. Dry-sliding friction and wear tests were complete in dry conditions, (<15 % humidity). Lubricated friction and wear tests were done in ambient conditions. A profilometer was used to measure depth and width of the tracks from all wear tests.

6.2.5 Atomic Force Microscopy (AFM)

An AFM was used to measure surface roughness of the polymer samples. Experiments in contact mode were carried out with a Dimension ^{TM} 3100 AFM (Nanoscope IV, Veeco Instruments, Santa Barbara, CA) in controlled low humidity (6 ± 2 % RH) conditions to minimize effects of adsorbed water vapor. Standard V-shaped silicon nitride probes from Veeco with a quoted normal spring constant of 0.58 N/m and tip radius of 10-40 nm were used. The normal spring constant of the cantilever used was calibrated to have an actual value of 0.35 N/m.

6.2.6 Scanning Electron Microscopy (SEM)

A JEOL JSM-606LV scanning electron microscope was used to image the microtribometer wear tracks from both the cyclic wear and the scratch tests. The sample chamber was low-vacuum and accelerating voltages of 1-2 kV at ranges of 10-200x magnification were used. These images were used to measure wear widths and scratch lengths. SEM was also used to image the Si_3N_4 probes to confirm a spherical shape (Figure 1) and to check for polymer film transfer after reciprocating wear tests. A conductive, gold layer (~ 200 Å thick) was sputter-coated onto the probes before imaging. Low accelerating voltage, 1-2 kV, was used.

6.2.7 Optical Microscopy

An Olympus BX51WI (Leeds Precision Instruments, Inc.) with Twin Epi-Flourescence Optical Pathway (Prairie Technologies) microscope used to image the wear tracks and probes.

6.2.8 Contact angle measurements

Hydrophobicity of the UHMWPE before and after exposure to DPPC was measured using contact angle measurements. Contact angles were measured using analysis of high magnification digital images from a CCD camera of 10 μl water droplets on each sample before and after soaking in the phospholipids solution.

6.3 Results

Differential scanning calorimetry (DSC) revealed that the two heat treated samples of UHMWPE had different crystallinities. Melting temperatures peaked at 134.5 °C for the nitrogen quenched sample and 139.5 °C for the slowly cooled sample. The peak melt transition temperature generally defines the point at which the largest lamellae of a polymer completely melt, and is characteristic of the degree of crystallinity in the bulk polymer.[26] The crystallinity percentages of the samples were calculated from the heat of enthalpy measured over that of a 100% crystalline sample, 291 J/g.[25] Heat of enthalpy for the quenched sample was 129.7 J/g and 162.5 J/g for the slowly cooled sample, giving crystallinities of 44.6 % and 55.8 %, respectively as tabulated in Table 1. Crystallinity measurements were performed on top surface layer (<0.5 mm), intermediate layer and the core of the sample. They showed no significant variation in the crystallinity values.

Topography maps of the two polymer samples taken by the AFM after heat treatment showed comparable surface roughness on both samples. HC-PE gave an RMS roughness of

Table 1. Physical and surface properties of UHMWPE samples as a function of crystallinity and exposure to DPPC.

Sample	Degree of crystallinity (%)[a]	RMS surface roughness (nm)[b]	Contact angle (degrees)[c]
Dry HC-PE	55.8	7.27 ± 0.96	59.4
Dry LC-PE	44.5	5.70 ± 0.93	88.2
HC-PE with DPPC	--	11.03 ± 3.3	76.8
LC-PE with DPPC	--	5.81 ± 0.76	45.4

[a]Crystallinity percentage was calculated from enthalpy values taken from DSC over 100% crystalline sample.
[b]Surface roughness measurements were taken on a 5 µm x 5 µm scan using AFM.
[b]Contact angle were measured using magnified digital images in Adobe Photoshop.

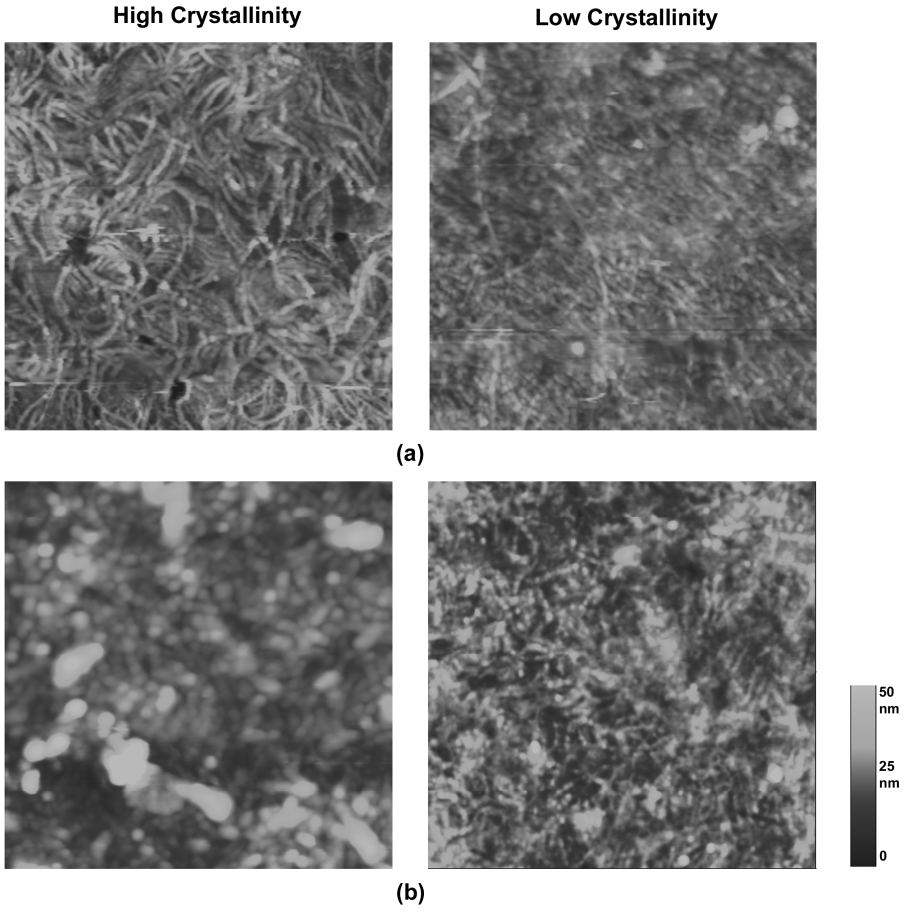

Figure 1. Topography maps of high crystallinity and low crystallinity samples from a 5 µm x 5 µm scan obtained using an atomic force microscope (AFM) **(a)** before and **(b)** after lipids.

7.27 ± 0.96 nm and LC-PE gave an RMS roughness of 5.70 ± 0.93 nm for 5 µm x 5 µm scans as shown in Table 1. The sample with higher crystallinity (HC-PE) displayed lamellar structure when examined with AFM (Figure 1), which is typical of recrystallization.[9] Lamellae were not as evident in the lower crystallinity (LC-PE) sample, and it is unlikely that spherulites were formed while quenching the sample. Roughness values after the polymer samples were exposed to the lipid solution were measured at 11.03 ± 3.33 nm and 5.81 ±

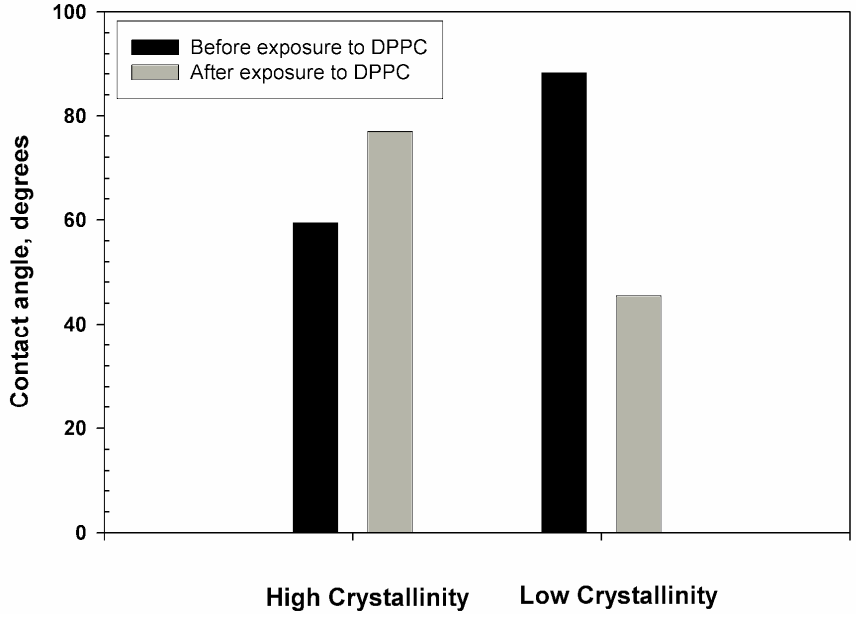

Figure 2. Plot of water contact angles on both high and low crystallinity samples of UHMWPE before and after exposure to phospholipid solution. Contact angles were measured from magnified digital images of water droplets on sample surfaces

0.76 nm for the HC-PE and LC-PE samples respectively. Roughness increased 50 % more for the HC-PE sample when compared to the LC-PE.

Figure 2 shows results of the contact angle measurements performed on the polymer surfaces before and after exposure to DPPC. Before exposure to phospholipids, LC-PE gave a contact angle of 88.2° and HC-PE was 59.4°. After being soaked in the DPPC solution, the contact angle of LC-PE decreased considerably to 45.4° and HC-PE increased to 76.8°.

Representative ramped-load friction responses of Si_3N_4 on UHMWPE are shown in Figure 3. The friction response of Si_3N_4 on LC-PE in both control and DPPC lubricated conditions was slightly higher than that of HC-PE. The presence of DPPC corresponded with

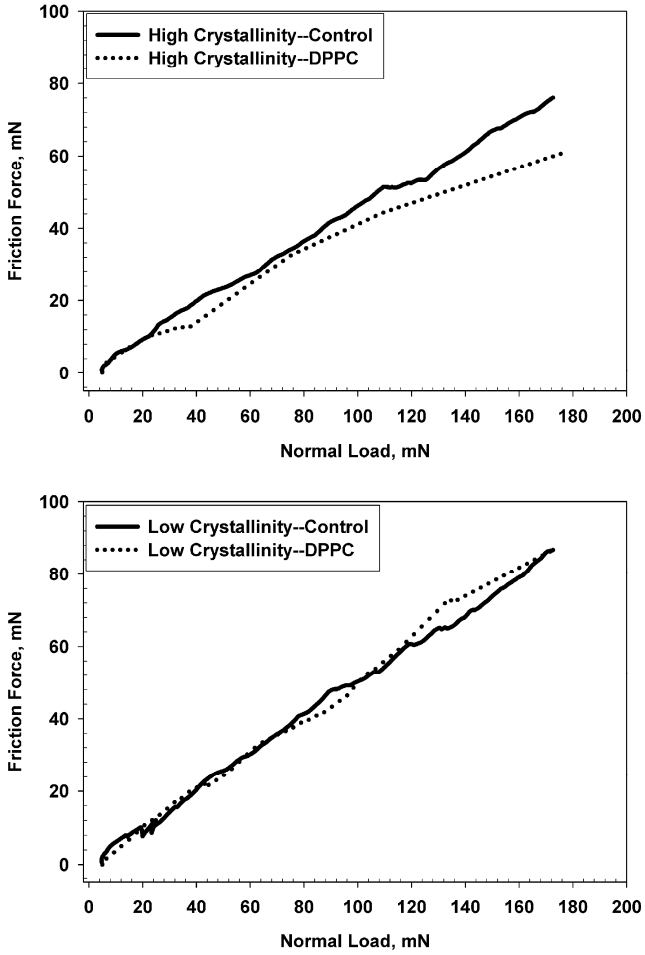

Figure 3. Friction response of ramped-load friction tests performed by microtribometer of Si_3N_4 on **(a)** high and **(b)** low crystallinity UHMWPE in the ethanol control and DPPC-ethanol solution.

a 17 % reduction in friction coefficient of HC-PE and a 10 % increase in friction coefficient of LC-PE for ramped-load friction experiments. Friction response of reciprocating wear tests (Figure 4) after 1000 cycles (a sliding distance of 30 m) in DPPC dissolved in ethanol

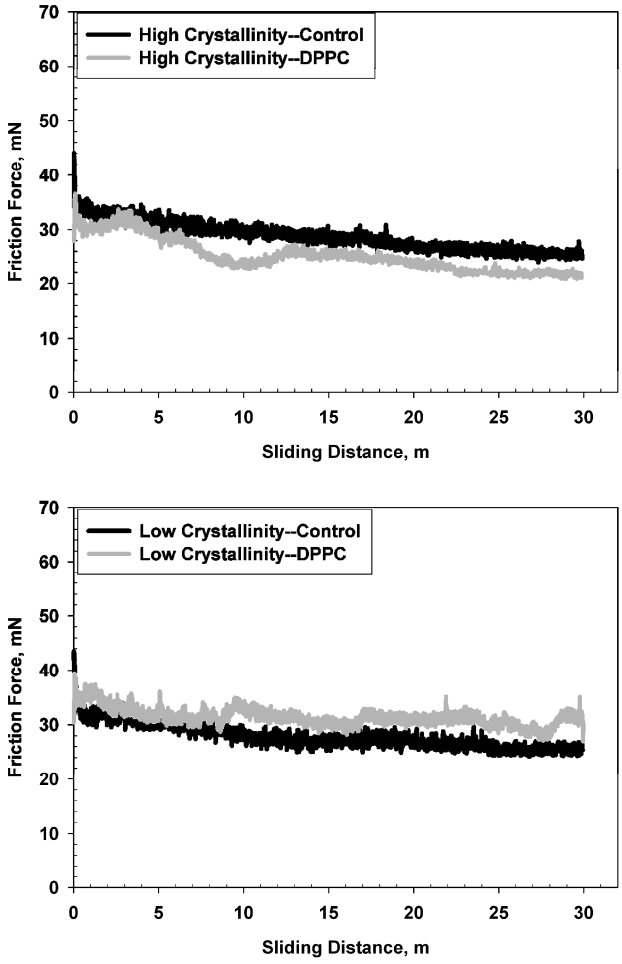

Figure 4. Friction response of reciprocating wear tests performed by microtribometer of Si_3N_4 on **(a)** high and **(b)** low crystallinity UHMWPE in the ethanol control and DPPC-ethanol solution.

showed a 17 % reduction in friction for HC-PE and a 22 % increase for LC-PE when compared to control tests.

6.4 Discussion

AFM topography images after exposure to lipids revealed the presence of particulate-like structures on both samples (Figure 1). The HC-PE sample had a considerably higher density of these structures on the surface. Since both samples had been rinsed and nitrogen dried after being submerged in the DPPC-ethanol solution for friction and wear testing, it can be expected that these structures represent surface-adsorbed entities. Rahamim et al. [27] identified phospholipids on the surface of a temporomandibular joint using electron microscopy. They found the phospholipids to be spherical, granular bodies ranging from 170-280 nm in diameter, and homogenously distributed on the surface.[27] Our AFM topography images showed that the adsorbed structures on the surfaces were similar in size and shape. Given that the samples were only exposed to the phospholipid solution, rinsed and nitrogen-dried, it can be reasonably assumed that the particles represent DPPC adsorption to UHMWPE. The images illustrate a strong presence of globules scattered throughout the HC-PE sample, but are barely noticeable on the LC-PE sample. This indicates that the HC-PE sample adsorbed significantly more DPPC than the LC-PE sample.

As mentioned earlier, surface tension is one factor that determines wettability of a surface, and can correlate with adsorption onto a surface.[28-30] Yui et al. showed that higher crystalline structure correlates with increased surface energy of a polymer using a method of comparing contact angle measurements on crystalline versus amorphous regions of polypropylene.[22] In our case, contact angle measurements were taken from magnified digital images of droplets on the surfaces. Contact angle measurements on dry UHMWPE samples before lipid testing indicated that HC-PE had higher surface energy and would be more likely to adsorb the DPPC. Hills et al. showed that on healthy, bovine cartilage saline beads up, but

on osteoarthritic cartilage deficient in SAPL, it will wet the surface.[14] His argument was that as the polar phosphate heads adsorbed to a hydrophilic surface, its fatty acid-chained tails create a hydrophobic monolayer surface.[31] The hydrophobicity of the new layer is dictated by the degree of adsorption onto the adsorbate, or its surface coverage.[29,31] Contact angle measurements of the samples taken after exposure to the DPPC solution indicated that HC-PE became more hydrophobic, whereas LC-PE became more hydrophilic, agreeing with early statements of higher phospholipids adsorption onto the HC-PE sample.

Wear behavior was also affected by the addition of DPPC into the tribological environment, Based on profilometer depth measurements, the HC-PE sample showed higher wear resistance than LC-PE in the control and DPPC-lubricated reciprocating tests (Table 2). The presence of DPPC in the lubricant corresponded with decrease in wear depth only for the higher crystallinity sample. After wear tests were completed, optical and SEM images of the

Table 2. Summary of friction coefficients and wear measurements as a function of UHMWPE crystallinity and exposure to DPPC.

Sample	Coefficient of friction[a]	Wear depth[b] (nm)	Film transfer
HC-PE with control	0.4348 ±.0012	165.9 ± 13.2	None
LC-PE with control	0.497 ±.0063	174.7 ± 13.8	Yes
HC-PE with DPPC	0.3624 ±.012	100.6 ± 32.1	Yes
LC-PE with DPPC	0.5478 ±.059	193.0 ± 38.7	Traces

[a]Calculated from the friction response of a Si_3N_4 probe on the microtribometer for ramped load friction tests of 0-200 mN.
[b]Measured using a profilometer on wear tracks from a Si_3N_4 probe on the microtribometer for 1000 reciprocating, 20 mm cycles at an applied load of 125 mN.

probes were analyzed to check for film transfer. Film transfer did not occur for HC-PE in the ethanol control (Figure 5(a)). Film transfer appeared in the case of HC-PE lubricated with DPPC in ethanol (Figure 5(b)), indicating adhesive wear. Optical images of the probe used in LC-PE tests on ethanol showed evidence of particles in the contact vicinity, and this material was interpreted as film transfer. SEM images of the probe used in phospholipid lubricant tests on LC-PE (Figure 5(b)) showed a slight presence of material on the surface of the probe which could not be seen with the optical microscope, therefore, it can be said that film transfer was negligible.

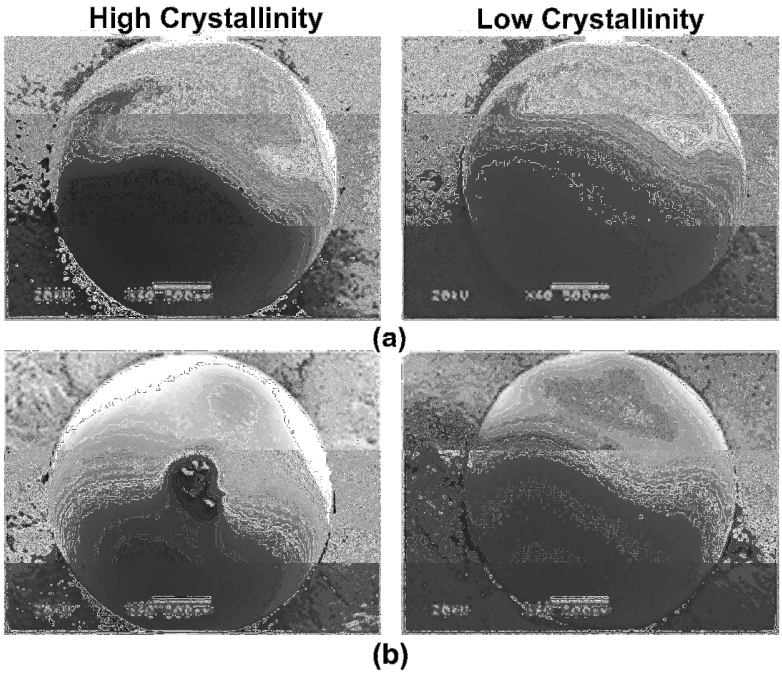

Figure 5. SEM images of the polymer contact regions on probes after reciprocating wear tests on high and low crystallinity UHMWPE in the **(a)** ethanol control **(b)** and DPPC-ethanol solution.

Friction results correspond well with trends found in literature that shows SAPL such as DPPC to reduce friction behavior.[13,17,21,32-34] Ozturk et al. showed a greater reduction in friction coefficient with an increase in DPPC concentration, and suggested that mixed or elastohydrodynamic lubrication occurred.[17] Friction tests show that articulating surfaces containing the phospholipid DPPC act as a releasing agent, much like Teflon®.[14] Hills and Thomas further explain that the nature of surfactants cause non-polar moieties to point outward, imparting hydrophobic surfaces less conducive to adhesion.[32] DPPC also acts as an effective boundary lubricant because of its ideal structure for monolayer cohesion;[32] a boundary lubricant is most successful when there is a strong cohesion within the bilayer, preventing asperity penetration from the counterface.[13] Bell et al. speculated that a bilayer created from SAPL acted as a boundary lubricant, illustrating that reduction of wear increased with SAPL concentration.[35] Saikko et al. also showed that DPPC as a boundary lubricant was highly effective in reducing wear volume.[36] The current study had results consistent with earlier findings that wear volume is reduced in the presence of phospholipids, particularly for the HC-PE sample. Based on the DPPC adsorption coverage seen on the sample, it's lowered friction and increased wear resistance, it is possible that DPPC operated as a boundary lubricant for the higher crystallinity sample. The same cannot necessarily be concluded for the low crystallinity sample which showed only a small reduction in friction and no increase in wear resistance, incidentally a result of the poor adsorption as evidenced in Figure 1. Saikko et al. went on to note that the phospholipids did not prevent film transfer, which can be characteristic of adhesive wear, and they concluded that phospholipids are

effective in reducing wear particle generation, but not transfer of the polymer.[36] Our results reveal a similar phenomenon.

6.5 Conclusions

Contact angles measurements and topography maps of the two UHMWPE samples confirmed that higher crystallinity UHMWPE is more likely to adsorb SAPL than low crystallinity UHMWPE. Friction response analyses support that friction decreases in the presence of a lubricated film of the phospholipid DPPC. Wear resistance appeared to increase as a function of lipid adsorption, which corresponded with increased degree of crystallinity of the polymer. Therefore, increasing crystallization is a mode of escalating adsorption of SAPL to UHMWPE, lending a more wear-resistant load bearing material for total joint replacements.

References

1. Kang PH, Nho YC. The effect of gamma-irradiation on ultra-high molecular weight polyethylene recrystallized under different cooling conditions. Radiation Physics and Chemistry 2001;60(1-2):79-87.

2. DesJardins J, Aurora A, Tanner SL, Pace TB, Acampora KB, LaBerge M. Increased total knee arthroplasty ultra-high molecular weight polyethylene wear using a clinically relevant hyaluronic acid simulator lubricant. Proceedings of the Institution of Mechanical Engineers Part H-Journal of Engineering in Medicine 2006;220(H5):609-623.

3. Brown SS, Clarke IC. A review of lubrication conditions for wear simulation in artificial hip replacements. Tribology Transactions 2006;49(1):72-78.

4. Sawae Y, Murakami T, Chen J. Effect of synovia constituents on friction and wear of ultra-high molecular weight polyethylene sliding against prosthetic joint materials. Wear 1998;216(2):213-219.

5. Greenbaum ES, Burroughs BB, Harris WH, Muratoglu OK. Effect of lipid absorption on wear and compressive properties of unirradiated and highly crosslinked UHMWPE: An in vitro experimental model. Biomaterials 2004;25(18):4479-4484.

6. Bergstrom JS, Rimnac CM, Kurtz SM. Prediction of multiaxial mechanical behavior for conventional and highly crosslinked UHMWPE using a hybrid constitutive model. Biomaterials 2003;24(8):1365-1380.

7. Kurtz SM, Villarraga ML, Herr MP, Bergstrom JS, Rimnac CM, Edidin AA. Thermomechanical behavior of virgin and highly crosslinked ultra-high molecular weight polyethylene used in total joint replacements. Biomaterials 2002;23(17):3681-3697.

8. Zhou J, Chakravartula A, Pruitt L, Komvopoulos K. Tribological and nanomechanical properties of unmodified and crosslinked ultra-high molecular weight polyethylene for total joint replacements. Journal of Tribology-Transactions of the Asme 2004;126(2):386-394.

9. Turell MB, Bellare A. A study of the nanostructure and tensile properties of ultra-high molecular weight polyethylene. Biomaterials 2004;25(17):3389-3398.

10. Simis KS, Bistolfi A, Bellare A, Pruitt LA. The combined effects of crosslinking and high crystallinity on the microstructural and mechanical properties of ultra high molecular weight polyethylene. Biomaterials 2006;27(9):1688-1694.

11. Rohrl S, Nivbrant B, Mingguo L, Hewitt B. In vivo wear and migration of highly cross-linked polyethylene cups - A radiostereometry analysis study. Journal of Arthroplasty 2005;20(4):409-413.

12. Ohta M, Hyon SH, Tsutumi S. Control of crystalline orientation to enhance the wear resistance of ultra-high molecular weight polyethylene crystallization cups for artificial joints. Wear 2003;255:1045-1050.

13. Gale LR, Coller R, Hargreaves DJ, Hills BA, Crawford R. The role of SAPL as a boundary lubricant in prosthetic joints. Tribology International 2007;40(4):601-606.

14. Hills BA, Crawford RW. Normal and prosthetic synovial joints are lubricated by surface-active phospholipid - A hypothesis. Journal of Arthroplasty 2003;18(4):499-505.

15. Gartner LP, Hiatt JL. Color Textbook of Histology. Philadelphia, Pennsylvania: W.B.Saunders Company; 2001.

16. Gispert MP, Serro AP, Colaco R, Saramago B. Friction and wear mechanisms in hip prosthesis: Comparison of joint materials behaviour in several lubricants. Wear 2006;260(1-2):149-158.

17. Ozturk HE, Stoffel KK, Jones CF, Stachowiak GW. The effect of surface-active phospholipids on the lubrication of osteoarthritic sheep knee joints: Friction. Tribology Letters 2004;16(4):283-289.

18. Jones CF, Stoffel K, Ozturk HE, Stachowiak GW. The effect of surface active phospholipids on the lubrication of osteoarthritic sheep knee joints: Wear. Tribology Letters 2004;16(4):291-296.

19. Reimann I. Pathological Human Synovial-Fluids - Viscosity and Boundary Lubricating Properties. Clinical Orthopaedics and Related Research 1976(119):237-241.

20. Swann DA, Bloch KJ, Swindell D, Shore E. The Lubricating Activity of Human Synovial-Fluids. Arthritis and Rheumatism 1984;27(5):552-556.

21. Mazzucco D, Scott R, Spector M. Composition of joint fluid in patients undergoing total knee replacement and revision arthroplasty: correlation with flow properties. Biomaterials 2004;25(18):4433-4445.

22. Yui N, Suzuki Y, Mori H, Terano M. Surface-Properties of Polypropylene Films as Biomaterials. Polymer Journal 1995;27(6):614-622.

23. Hirvi JT, Pakkanen TA. Molecular dynamics simulations of water droplets on polymer surfaces. Journal of Chemical Physics 2006;125(14).

24. Kanaga Karuppiah KS, Bruck AL, Sundararajan S, Wang J, Lin Z, Xu Z-H, Li X. Friction and wear behavior of ultra-high molecular weight polyethylene as a function of polymer crystallinity. Acta Biomaterialia Accepted - Corrected proof available online.

25. Nevoralova M, Baldrian J, Pospisil J, Chodak I, Horak Z. Structure modification of UHMWPE used for total joint replacements. Journal of Biomedical Materials Research Part B-Applied Biomaterials 2005;74B(2):800-807.

26. Sperling LH. Introduction to Physical Polymer Science. Hoboken, New Jersey: John Wiley & Sons, Inc.; 2006. 845 p.

27. Rahamim E, Better H, Dagan A, Nitzan DW. Electron microscope and biochemical observations of the surface active phospholipids on the articular surfaces and in the synovial fluid of the temporomandibular joint: A preliminary investigation. Journal of Oral and Maxillofacial Surgery 2001;59(11):1326-1332.

28. Tretinnikov ON. Wettability and microstructure of polymer surfaces: stereochemical and conformational aspects. Zeist, Netherlands: Elsevier; 2000. 111-128 p.

29. Shaw DJ. Introduction to Colloid and Surface Chemistry. 4th Ed; 1992.

30. Adamson AW. Physical Chemistry of Surfaces. New York: Interscience Publishers; 1960.

31. Hills BA. Boundary lubrication in vivo. Proceedings of the Institution of Mechanical Engineers Part H-Journal of Engineering in Medicine 2000;214(H1):83-94.

32. Hills BA, Thomas K. Joint stiffness and 'articular gelling': Inhibition of the fusion of articular surfaces by surfactant. British Journal of Rheumatology 1998;37(5):532-538.

33. Schmidt TA, Gastelum NS, Nguyen QT, Schumacher BL, Sah RL. Boundary lubrication of articular cartilage - Role of synovial fluid constituents. Arthritis & Rheumatism 2007;56(3):882-891.

34. Murakami T, Higaki H, Sawae Y, Ohtsuki N, Moriyama S, Nakanishi Y. Adaptive multimode lubrication in natural synovial joints and artificial joints. Proceedings of the Institution of Mechanical Engineers Part H-Journal of Engineering in Medicine 1998;212(H1):23-35.

35. Bell J, Tipper JL, Ingham E, Stone MH, Fisher J. The influence of phospholipid concentration in protein-containing lubricants on the wear of ultra-high molecular weight polyethylene in artificial hip joints. Proceedings of the Institution of Mechanical Engineers Part H-Journal of Engineering in Medicine 2001;215(H2):259-263.

36. Saikko V, Ahlroos T. Phospholipids as boundary lubricants in wear tests of prosthetic joint materials. Wear 1997;207(1-2):86-91.

CHAPTER 7. SURFACE STRESS GENERATION DURING FORMATION OF ALKANETHIOL SELF-ASSEMBLED MONOLAYER (SAM)

Modifired from a paper published in *Mechanics Research Communications*
2008, 35, 43-49
P. Shrotriya, K.K.S. Karuppiah, R. Zhang, A. Chandra, S. Sundararajan

7.1 Introduction

Self-assembled monolayers (SAM) are being increasingly investigated for applications in chemical and biological sensors and modifying tribo-chemical properties of surfaces for applications to micro electro mechanical systems (MEMS) (Ulman, 1991). Surface stress generation associated with formation of SAM is intriguing phenomena and has led to the rise of novel sensing mechanism for chemical and biological species (Berger et al., 1997, 1998; Godin et al., 2003, 2001, 2004; Raiteri et al., 2000; Tabard-Cossa et al., 2005).

Cantilever deflection based chemical sensors are on the rise ever since Thundat et al. (1994) reported the deflection of atomic force microscope cantilevers due to changes in relative humidity and thus opened a myriad of possibilities for the use of atomic force microscope cantilever deflection technique for chemical and biological sensing. Berger et al. (1997) reported the generation of compressive stresses on an AFM cantilever during the formation of alkanethiol self-assembled monolayer on the cantilever's surface. They showed a surface stress on the order of 0.1–0.5 N/m and also reported that the magnitude of surface stress increased linearly with the carbon chain backbone of the monolayer. Since the first

report by Berger et al. (1997), SAMs have been used as test system for almost all cantilever based sensing techniques (Godin et al., 2004; Raiteri et al., 2000; Ji et al., 2000; Stevenson et al., 2002). This is because they are relatively easy to prepare, form well-ordered close packed films and offers limitless possibilities of variations in chain length, end group and ligand attachments (Ulman, 1991). One of the commonly studied SAMs are alkanethiol SAMs (HS-$(CH2)_{n_1}$CH3). Godin et al. (2004) have shown that the kinetics of formation of self assembled monolayers on gold-coated cantilevers and the resulting structure are dependent on the structure of the gold grain itself and also the rate at which the SAM reaches the surface. They showed a surface stress value on the order of 0.5–15 N/m. The surface stress generated was also shown to be dependent for different surface density (coverage) of the monolayer on the substrate. All of the previous studies have primarily measured surface stress generation due to SAM formation on micro-scale domains (μm x μm). An interesting question that remains unanswered is whether similar surface stress generation will be associated with SAM formation on larger surfaces (mm x mm)? Will the magnitude of surface stress generation be of the same order as the size of domain is increased? In addition, the mechanistic understanding of the mechanism governing surface stress generation remains largely unaddressed.

In this study, the surface stress generated during the formation of self assembled monolayers is investigated using a combined experimental and computational approach. Curvature interferometry is used to measure the surface stress generation associated with SAM formation on large domains. A multiscale model based on long range interaction of adatom induced elastic field is developed to predict the surface stress generation. To the best

of our knowledge, this is the first report on a quantitative comparison and reasonable agreement between experimental measurement and computational predictions of surface stress generation.

7.2 Experimental details

7.2.1 Materials

Specimens were prepared by depositing a thin layer of gold on cleaved mica surfaces. Gold wire (product #12201) was purchased from Ernest F. Fullam, Inc., NY and used as received. Hi-grade Mica (25 x 25 mm) sheets were purchased from Ted Pella Inc., CA and were cleaved repeatedly until a smooth surface (examined visually) was obtained. Final thickness of mica sheets was about 150 μm. The mica sheets were loaded in a thermal evaporator and were coated with 200 nm of gold. The mica sheets coated with gold were kept in a clean room until use. Octadecanethiol ($C_{18}H_{38}S$) was purchased from Sigma Aldrich. A 2 mM ethanolic solution of the octadecanethiol was prepared and used for vapor phase deposition of alkanethiol on gold-coated mica surfaces.

7.2.2 Curvature interferometry setup

Curvature change of the specimen during formation of alkanethiol SAM layers was monitored to determine the surface stress development. Recently invented curvature interferometry technique (Wang et al., 2006) was used to measure the surface stress change. The interferometry setup is showed in Fig. 1. In this setup, two laser beams are reflected twice from a substrate at points A, B and C, D, respectively. As a result, the beams develop a

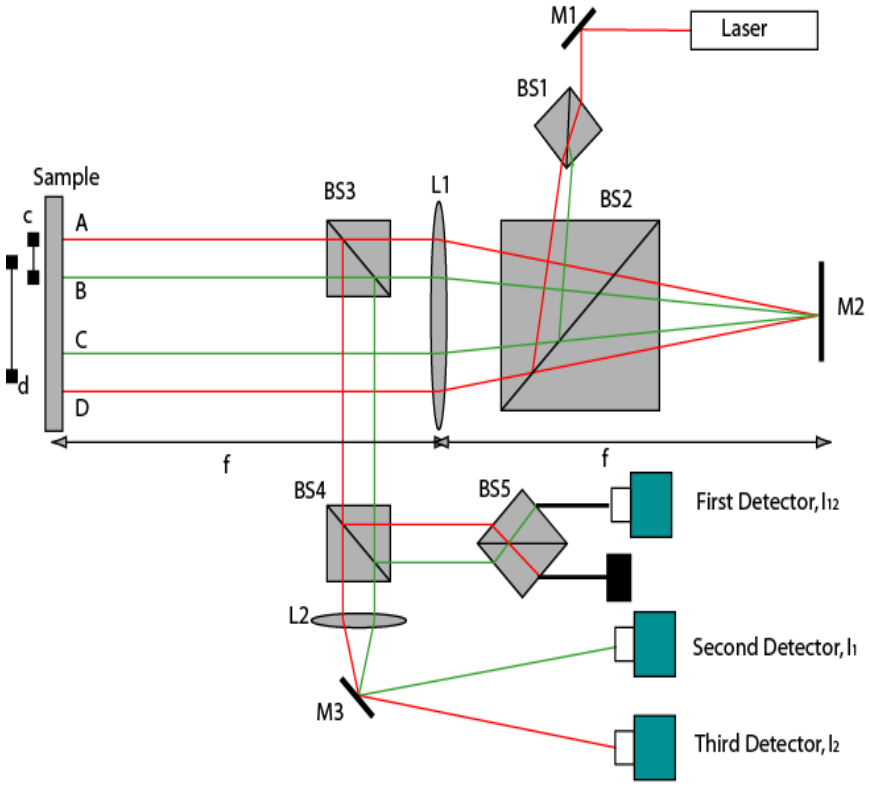

Figure 1: Schematic representation of curvature interferometer

path difference proportional to curvature of substrate and intensity of the interfered beam (measured by photodetector (I12)) may be utilized to infer the substrate curvature.

After repeated reflections from the sample surface, the two beams accumulate a path length difference, D, proportional to the curvature, κ, of the sample, such that $\kappa = 1/R = \Delta/(2cd)$. The optical path length difference, Δ, corresponds to a phase difference of $2\pi\Delta/\lambda$ between the two beams, where λ is the wavelength of the laser. The phase difference can be obtained by measuring the interference between the two beams reflected from positions C and D. Stoney equation (Stoney, 1909) is used to determine the surface stress change, *f*, associated measured curvature of the specimen,

$$f = \frac{Et^2\Delta}{12cd(1-\nu)}, \tag{1}$$

where E and ν are the Young's modulus and Poisson's ratio, respectively, t is the sample thickness, c, d, κ, and Δ are the same as defined earlier.

7.2.3 Procedure

Atomic force microscope (AFM) was used to determine the roughness and grain size of gold film on specimens. For the SAM formation, a small plexiglass chamber with a liquid well was constructed and the sample is placed over the well. Plexiglass chamber was placed in the interferometer such that the laser beams are directed onto the sample. Alkanethiol SAM formation is initiated by injecting 1 ml of the 2 mM ethanolic solution of octadecanethiol into the well. The intensities of the interfered beam (I12) as well as of each beam (I1 and I2) are monitored throughout the SAM formation to measure the surface stress change. Data acquisition is only stopped after the intensity values after the intensities reach a stable value, a period of approximately 1–2 h.

7.3 Results and discussion

AFM scan of gold film surface for a scan size of 500 x 500 nm is shown in Fig. 2. Root mean square roughness of the gold surface was 1.92 ± 0.08 nm for the 500 nm scan size. As shown in Fig. 2, grain sizes in the gold film varied from about 60 to 80 nm. Given the long time duration of experiment and relatively small magnitude of expected surface stress change, the stability and resolution of curvature interferometer was characterized to

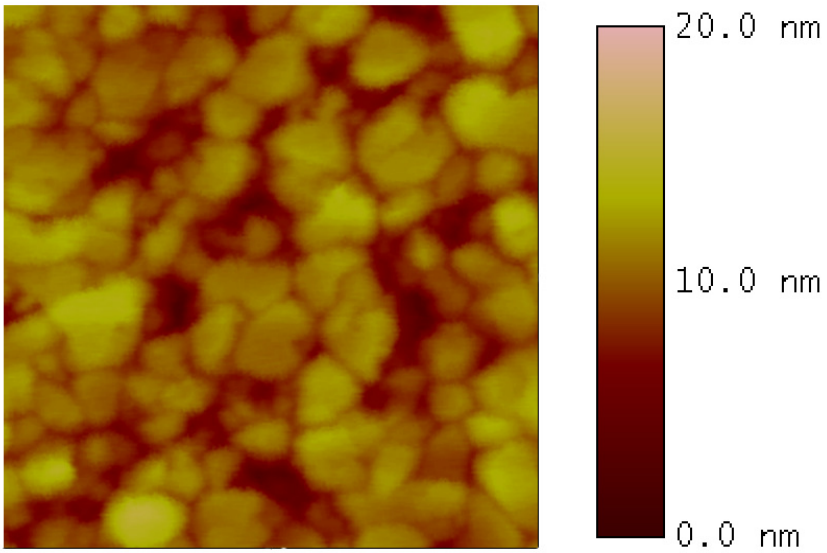

Figure 2: AFM scan of thermally evaporated gold film (500 nm x 500 nm scan size)

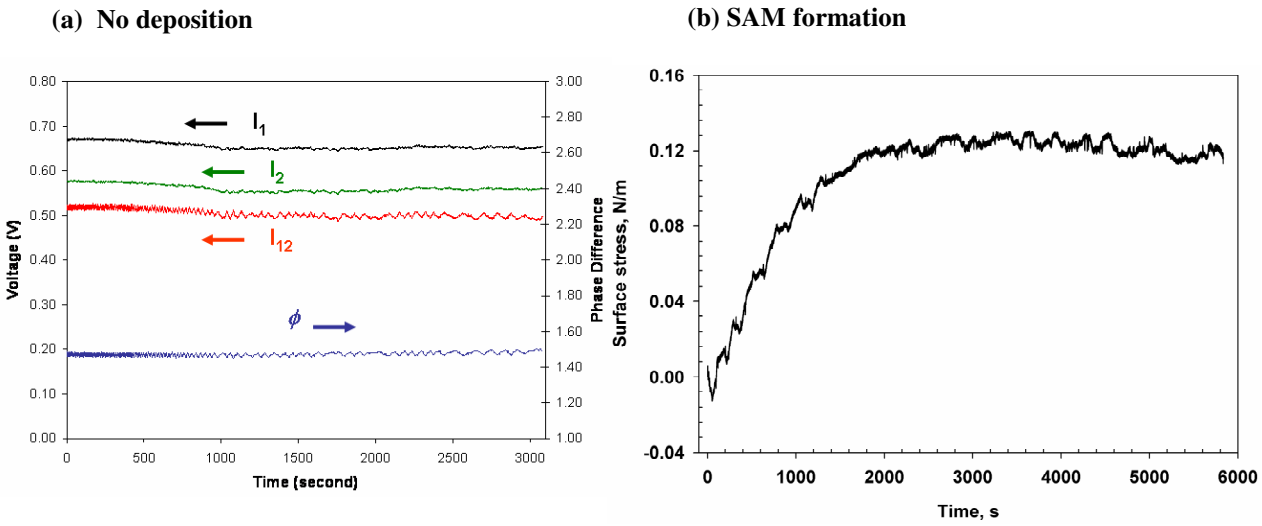

Figure 3: Interferometric measurements: (a) Stability of curvature measurement during no deposition on sample surfaces; (b) Surface stress measured during formation of alkanethiol SAM on gold coated surface

ensure accurate measurement. Before the SAM deposition experiment, curvature of sample was monitored for a period of approximately 1 h to characterize the stability of interferometric measurements. Measured intensity of the interfered and individual beam as well as the calculated phase difference during no deposition on sample surface is shown in Fig. 3a. In the first 20 min of switching the laser on, intensity of individual beams show some variations however the calculated phase difference is stable throughout the hour with variations of only ±1% about the mean value.

After the initial characterization run, sample was exposed to alkanethiol solution and associated surface stress change is plotted in Fig. 3b as a function of time. As shown in Fig. 3b, the specimen undergoes a initial tensile surface stress change before the compressive surface stress development. Initial tensile surface stress development has been previously reported by other researchers (Berger et al., 1997) as well and is thought to be associated with knocking off of surface adsorbed species by individual alkanethiol molecules. After the initial knock-off phase, the alkanethiol molecules get adsorped on the surface and arrange into self-assembled monolayers. At around 40 min, the monolayer formation reaches saturation indicated by stable value of surface stress change. Plot of surface stress change closely resembles a langmuir adsorption isotherm. The surface stress change associated with the formation of octadecanethiol on gold-coated mica substrate is about 0.12– 0.15 N/m which is comparable to previously reported values obtained by other researchers for micro scale domains (Berger et al., 1997; Godin et al., 2004).

Two different mechanisms (Berger et al., 1997; Godin et al., 2004) have been proposed to explain the development of compressive surface stress: either due to entropic

interactions induced repulsion between individual alkanethiol molecules or due to long range interaction between elastic fields induced by individual chains in the gold substrate. SAM formation is associated with three phases associated with increasing surface coverage: (1) initially at low surface coverages, alkanethiol molecules are adsorbed at isolated locations and lie flat on the surface (2) at intermediate surface coverage, the alkanethiol chain still lie flat on the surface but are arranged in groups parallel to each other and (3) finally near saturation coverage, the competition between thiol group absorption on surface and inter chain repulsion leads to formation of close packed self-assembled monolayers (Ulman, 1991; Godin et al., 2004). At low and intermediate surface coverage, the alkanethiol chains are isolated and are not arranged in ordered fashion. Hence, entropic interactions between the chains during the initial part of SAM formation are limited and may not contribute to surface stress generation during the initial phase. Experimental results show that even under a fairly low coverage a significant surface stress develops during the adsorption processes. This suggests that large scale interaction between elastic field induced by adsorbed chains plays a significant part in the surface stress development. Near saturation coverages, the chains form ordered structures and entropic interactions are expected to play an important part in the surface stress generation. In the current paper, the surface stress development due to long range interactions of induced elastic field is investigated. We are in the process of developing models for quantifying the entropic interactions between the chains.

Following Kukta et al. (2003), the elastic field induced by an adsorbed alkanethiol molecule is approximated by a force dipole acting on the surface. Strength of the adsorbed molecules induced force dipole is expressed as function of surface strain and adsorbed

molecules interact with each other through their elastic fields. Atomistic calculations may be utilized to compute the energy change induced due to adsorption of alkanethiols from comparison between energies of a system with molecules on the surface (U) and the same system with the molecules removed (U^r). Absorption induced energy change is modeled as a quadratic function of surface strain ($\bar{\varepsilon}_{22}$) as:

$$\psi(\bar{\varepsilon}) = U - U^r = \psi^0 + D^0\bar{\varepsilon}_{22} + \frac{1}{2}F^0\bar{\varepsilon}_{22}^{\ 2}, \tag{2}$$

where $\psi(\bar{\varepsilon})$ is the adatom energy, D^0 is the strength of the force dipole induced due to atom adsorption and F^0 determines dependence of induced force dipole on the surface strain to first order. For a two-dimensional geometry, the surface stress change due to molecule adsorption is expressed as: (Kukta et al., 2003)

$$\Delta\tau(\rho) = -\frac{3\rho D^0}{3 - \pi^2\rho^2 C F^0}, \tag{3}$$

where $C = (1-\nu)/\pi\mu$ is a positive constant related to substrate Poisson's ratio (ν) and the shear modulus (μ); ρ is the density of molecules on the surface. Embedded atom method based empirical potential (Foiles et al., 1986) was utilized to compute the adsorption induced energy change in gold surface. To the best of our knowledge, there are no reported potentials for interaction between gold atoms and alkanethiol atoms. Therefore, an indirect approach based on residual charges on Au atoms is utilized to approximate the alkanethiol adsorption. During the chemisorption of alkanethiol molecules and formation of Au–S bonding, some electrons flow from Au substrate into the alkanethiol chains. Beardmore et al. (1997) modeled the head-group interaction for alkanethiols (S–CH3) on Au (111) using density

functional theory. Residual atomic charges of (3 x +0.17e) were computed for the nearest Au atoms for each adsorption site (Beardmore et al., 1997). These residual charges are used to augment charge of nearest Au ions in the EAM force field in order to simulate the formation of Au–S bonding. Augmentation of Au ion charge leads to increased pairwise repulsive interactions and consequently, compressive surface stress on the gold surface.

For the atomistic calculation of energy change due to adsorption of a line of alkanethiol molecules, a simulation cell that includes 87480 gold atoms with approximate dimensions of 23 nm x 3 nm x 21 nm is utilized. As discussed before, alkanethiol adsorption is simulated by augmenting the charge of Au ions that are closest to each adsorption site. In order to determine the energy change as a function of surface strain, molecular statics simulations are performed to determine the equilibrium energy for both initial (U^r) and augmented charge ensembles (U) for different levels of imposed strains (0, ±0.25% and ±0.5%). For each simulation, conjugate gradient algorithm is used to minimize the total energy. Energy change is fitted to the quadratic function of imposed strain field to determine the induced dipole dependence on surface strain shown in Eq. (2). Adatom induced energy change were computed for five different residual charge values (0.11–0.55e). Surface strain dependence of adatom induced energy change and the associated fit for a residual charge of 0.11e is shown in Fig. 4a. Values of D^0 and F^0 determined from curve fitting were used to predict the surface stress change as a function of coverage density following Eq. (3).

Predicted surface stress change for all five residual charge values is shown in Fig. 4b. Values of D^0 for all the five cases was found to be negative indicating that residual charge act as a dilatation center and according to Eq. (3), generates compressive surface stress.

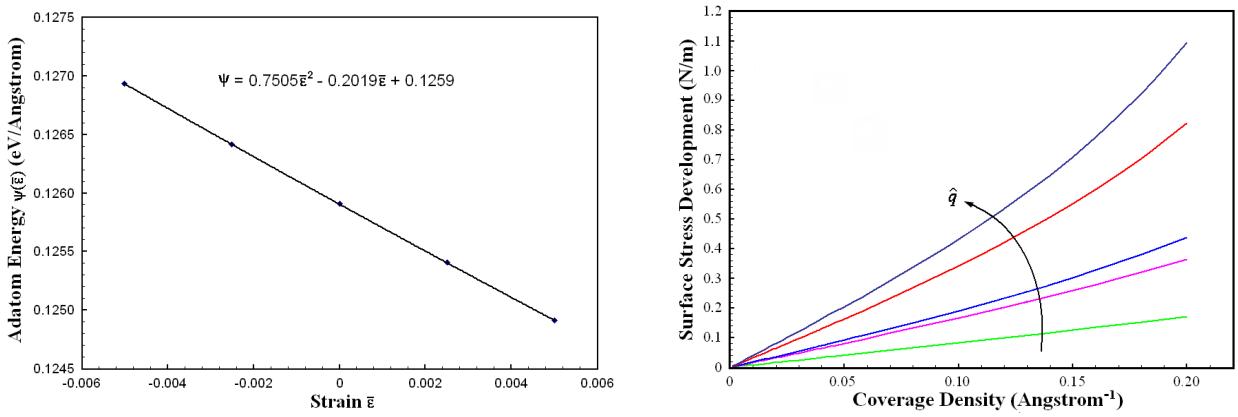

Figure 4: Surface stress prediction: (a) Surface strain dependence of adsorbate induced energy change for a residual charge of 0.11e on nearest Au atoms; (b) Predicted surface stress change due to long range interactions of dipoles corresponding to different residual charges (**— 0.11e, — 0.22e, — 0.33 e, — 0.44e, — 0.55e)**

Magnitudes of predicted compressive surface stress development are of the same order of magnitude (0.1–1.0 N/m) and indicates that long range interactions of induced elastic field play an important part in surface stress development during alkanethiol adsorption process. However, there are some points that need to be noted. Residual charges are only an approximation of S–Au bond and *ab initio* quantum calculation are required to develop accurate charge distribution and S–Au interaction for the purpose of surface stress prediction.

7.4 Conclusions

High resolution measurement of surface stress associated with alkanethiol SAM formation on macroscale domains (25 mm x 25 mm) are preformed using curvature

interferometry. Surface stress of 0.12–0.15 N/m was measured for octadecanethiol monolayers formation on gold coated mica substrates. Magnitude of surface stress measurement on macroscale domain compares well with previously reported measurement on micron sized domains. A multiscale approach based on long range interaction of adsorbate induced elastic fields is presented to quantify the surface stress development.

References

Beardmore, K.M., Kress, J.D., Bishop, A.R., GronbechJensen, N., 1997. Ab-initio calculations of the gold–sulfur interaction for alkanethiol monolayers. Synthetic Metals 84 (1–3), 317–318.

Berger, R., Delamarche, E., Lang, H.P., Gerber, C., Gimzewski, J.K., Meyer, E., Guntherodt, H.J., 1997. Surface stress in the selfassembly of alkanethiols on gold. Science 276 (5321), 2021–2024.

Berger, R., Delamarche, E., Lang, H.P., Gerber, C., Gimzewski, J.K., Meyer, E., Guntherodt, H.J., 1998. Surface stress in the selfassembly of alkanethiols on gold probed by a force microscopy technique. Applied Physics A – Materials Science & Processing 66, S55–S59.

Foiles, S.M., Baskes, M.I., Daw, M.S., 1986. Embedded-atom-method functions for the Fcc metals Cu, Ag, Au, Ni, Pd, Pt, and their alloys. Physical Review B 33 (12), 7983–7991.

Godin, M., Tabard-Cossa, V., Grutter, P., Williams, P., 2001. Quantitative surface stress measurements using a microcantilever. Applied Physics Letters 79 (4), 551–553.

Godin, M., Laroche, O., Tabard-Cossa, V., Beaulieu, L.Y., Grutter, P., Williams, P.J., 2003. Combined in situ micromechanical cantilever-based sensing and ellipsometry. Review of Scientific Instruments 74 (11), 4902–4907.

Godin, M., Williams, P.J., Tabard-Cossa, V., Laroche, O., Beaulieu, L.Y., Lennox, R.B., Grutter, P., 2004. Surface stress, kinetics, and structure of alkanethiol self-assembled monolayers. Langmuir 20 (17), 7090–7096.

Ji, H.F., Finot, E., Dabestani, R., Thundat, T., Brown, G.M., Britt, P.F., 2000. A novel self assembled monolayer (SAM) coated microcantilever for low level caesium detection. Chemical Communications (6), 457–458.

Kukta, R.V., Kouris, D., Sieradzki, K., 2003. Adatoms and their relation to surface stress. Journal of the Mechanics and Physics of Solids 51 (7), 1243–1266.

Raiteri, R., Butt, H.J., Grattarola, M., 2000. Changes in surface stress at the liquid/solid interface measured with a microcantilever. Electrochimica Acta 46 (2–3), 157–163.

Stevenson, K.A., Mehta, A., Sachenko, P., Hansen, K.M., Thundat, T., 2002. Nanomechanical effect of enzymatic manipulation of DNA on microcantilever surfaces. Langmuir 18 (23), 8732–8736.

Stoney, G.G., 1909. The tension of metallic films deposited by electrolysis. Proceedings of the Royal Society of London. Series A, Containing Papers of a Mathematical and Physical Character 82 (553), 172–175.

Tabard-Cossa, V., Godin, M., Beaulieu, L.Y., Grutter, P., 2005. A differential microcantilever-based system for measuring surface stress changes induced by electrochemical reactions. Sensors and Actuators B – Chemical 107 (1), 233–241.

Thundat, T., Warmack, R.J., Chen, G.Y., Allison, D.P., 1994. Thermal and ambient-induced deflections of scanning force microscope cantilevers. Applied Physics Letters 64 (21), 2894 2896.

Ulman, A., 1991. An Introduction to Ultrathin Organic Films: From Langmuir–Blodgett to Self-Assembly. Academic Press, New York, 442.

Wang, J., Shrotriya, P., Kim, K.S., 2006. Surface residual stress measurement using curvature interferometry. Experimental Mechanics 46 (1), 39–46.

CHAPTER 8. ACTIVE FRICTION MODULATION OF SELF-ASSEMBLED MONOLAYER FILMS USING EXTERNAL ELECTRIC FIELDS

Modified from a paper submitted to *Nanoletters*

K.S. Kanaga Karuppiah, Sriram Sundararajan, Yibo Zhou, Keith L. Woo

8.1 Introduction

Self-assembled monolayers (SAMs) are organic molecules which form monomolecular layers spontaneously when a solid substrate is immersed into a solution containing the molecules.[1, 2] SAMs have been widely used in molecular electronics,[3-7] biosensors,[8-14] microfabrication[8-12] and as molecular lubricants for passive tribological control to minimize adhesion and friction in micro/nano-electromechanical systems (MEMS/NEMS).[13-15] Alkanethiols are the most commonly studied SAMs [16] – they are relatively easy to prepare, form well-ordered close-packed films and have been extensively investigated for tribological performance.[17-22] Researchers have studied various factors affecting their tribological behavior such as chain length,[23, 24] terminal group chemistry,[19, 25-28] pressure,[29] humidity,[30] packing density,[31] and temperature.[30, 32] A powerful and robust means of tribological control involves "active" strategies characterized by the feature that, by some external stimuli, the tribological system (surface, lubricant or coating) is altered as desired. For example, researchers have investigated using an electric field or electric current across an interface [33-37] as well as using temperature sensitive polymer films[38] to modulate

friction at an interface on the macroscale. Liu et al.[39] have suggested that friction and wear characteristics of Langmuir-Blodgett (LB) films can be controlled and improved using external electric fields. However Lahann et al.[40] suggest that electric fields will have negligible effect on close-packed alkanethiol systems and developed a switching surface with loosely packed SAMs. They postulated that in order to obtain a SAM system for conformational switching, sufficient spatial freedom for each molecule to do so must be established. They realized a low-density SAM using thiols of (16-mercapto)hexadecanoic acid (MHA) because of its established self-assembly on gold surfaces and its hydrophobic chain and hydrophilic end-group combination.

In this paper, we report our preliminary investigations on the possibility of using external electric fields as a means to actively control the friction response of a low density MHA film via atomic force microscopy experiments. To the authors' knowledge, this represents one of the first studies performed to investigate friction response of alkanethiol SAM systems in the presence of an external electric field.

8.2 Experimental Section

8.2.1 Materials

(16-mercapto)hexadecanoic acid, 4,4'-dimethoxytrityl chloride, dithioerythritol, chlorotrityl chloride and silver nitrate were purchased from Sigma Aldrich (St.Louis, MO) and used as received. Gold wires (99.99%) were purchased from Ernest F. Fullam Inc. (New

York). Gold-coated (coating thickness ~ 200 nm) conductive silicon probes were purchased from Novascan Technologies Inc. (Ames, IA).

8.2.2 Substrate preparation

Glass slides were cleaned using the following procedure: a 2% RBS-35®detergent solution with 18.2 Mohm water was heated to boiling on a temperature bath and the glass slides were soaked in the boiling solution for 10 minutes. Then, the glass slides were rinsed with running 18.2 Mohm water for two complete cycles of the water purifier, following which, the glass slides were dried in a laminar flow hood and stored in a desiccant chamber until further use. Cleaned glass slides were coated with 15 nm of Cr (adhesion layer) followed by 200 nm of gold in an e-beam evaporator.

[(16-mercapto) hexadecanoic acid (2-chlorophenyl)diphenylmethylester] (16-MHAE) was synthesized as outlined by Lahann et al.[40] The synthesis is a three-step protocol - In the first step, 16-mercaptohexadecanoic acid's thiol group is protected, the second step involves conversion of the end-group carboxylic acid into an ester and the third step deprotects the thiol group to enable deposition on a surface.

SAMs of MHAE were prepared by immersing the gold coated substrates in a 1mM ethanolic solution of the 16-MHAE for 24 hours at room temperature. After removal from the solution, the substrates were cleaned with anhydrous ethanol, deionized water several times and then dried under a filtered stream of N_2. Removal of the ester end group was performed by incubating the substrates in a 50% trifluoroacetic acid in anhydrous ethanol for 2 minutes followed by rinsing it with ethanol and deionized water several times and dried under a

filtered stream of N_2. This process is expected to result in surfaces covered with a low density SAM system with a carboxylic end group. The substrates were stored in ambient conditions until further use. These substrates showed no significant oxidative degradation and have been shown to be chemically stable under ambient conditions.[41]

8.2.3 Instrumentation

X-ray photoelectron spectroscopy (XPS) measurements were performed using a Perkin-Elmer model 5500 employing Al $K\alpha_1$ radiation and an escape angle of 45° between sample and analyzer. Ellipsometry measurements were carried out using an automated optical system (MultiSkop, Optrel GbR, Berlin, Germany).

Friction and pull-off force experiments were carried out using a Dimension 3100 (Nanoscope IV, Veeco Instruments, Santa Barbara, CA) AFM under a nitrogen atmosphere (10 ± 2 % relative humidity) to minimize effects of adsorbed water vapor. Commercially available rectangular Si cantilevers (made conductive by a 200 nm gold coating throughout) were used for all measurements. The normal spring constant of the cantilever used was calibrated using the reference lever technique described by Torii et al.[42] AFM force-displacement curves provided the pull-off (adhesive) force, between the Si tip and the sample.

Friction force scans were performed at 90^0 scan angle on a 1 μm scan area with a scanning speed of 2 Hz. The friction response of the tip on a sample was taken to be the difference between the lateral deflection values of forward and reverse scans of a given scan line (i.e. from the friction loop of a scan line). The friction value thus noted is a measure of

the friction force. This method is commonly used to eliminate contributions from non-friction sources.[43] Friction force data presented are averages of six measurements at multiple sample locations. To help ensure that the observed friction response was not affected by change in tip radius, the radius of the tip was characterized before and after the experiments using a commercially available tip characterizer sample TGT01 (Mikromasch). The images are then analyzed using commercial software (Image Metrology) to calculate the tip radius. The tip profiles are generated using a MATLAB code.[44] Using this methodology, we found that the tip radius did not change appreciably during our experiments.

In order to study friction of the SAM system in the presence of an electric field, the probe/cantilever was connected to ground while a positive or negative bias (with respect to the ground) was applied to the metallic sample holder as shown in Figure 1. The SAM

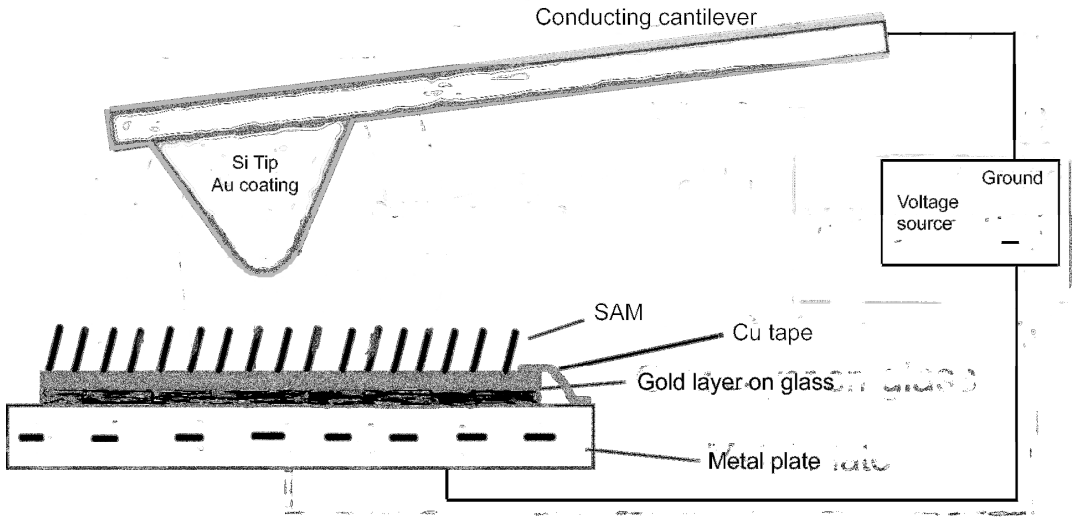

Figure 1. Schematic of the experimental setup for providing a bias between the grounded atomic force microscope (AFM) probe and the SAM sample. The cantilever and probe are made of conductive silicon with a 200 nm gold coating.

substrate was attached to the sample holder using a conductive copper tape. This arrangement results in the contact area between the probe and sample being completely enclosed in an electric field during application of bias.

8.3 Results and Discussion

XPS was used to confirm the complete cleavage of the ester group by tracking the presence and absence of chlorine before and after treatment with trifluoroacetic acid (TFA). The Cl-2p peak (~ 200 eV BE) present before treatment did not show up after treatment indicating the cleavage of the ester group. Also, the intensities of S2p and Au4f increased after treatment as they were initially attenuated because of the presence of the bulky ester group before treatment. Figure 2 shows a comparison of the intensity of C1s, S2p, Au4f and Cl2p peaks before and after treatment with trifluroacetic acid. Lee et al.[31] have shown a

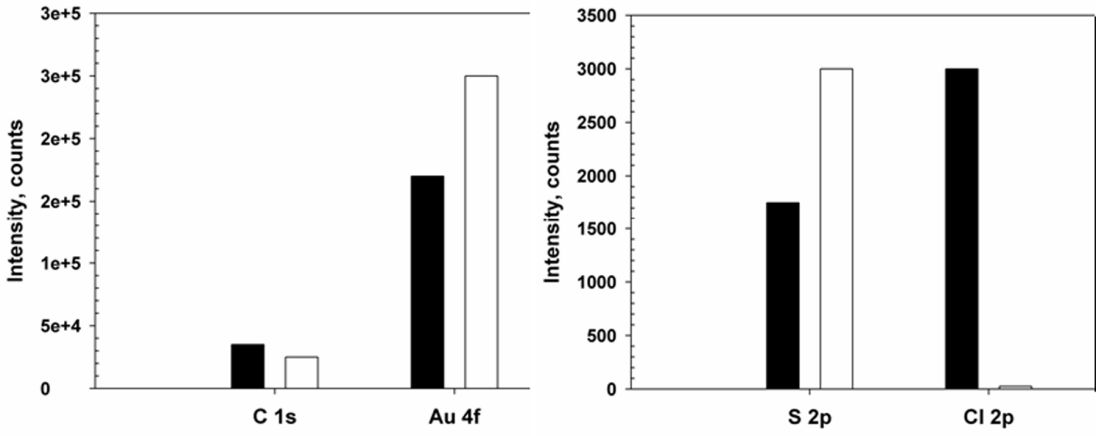

Figure 2. XPS measurements showing intensities of elements before and after treatment of the MHAE self-assembled monolayers (SAMs) (on a silicon substrate) with trifluoroacetic acid.

similar increase in S and Au intensities and a decrease in C intensity between an ordered alkanethiol and a disordered spiroalkanedithiol. Our data might therefore suggest that the bulky ester group (before treatment) helped to preserve the ordered, crystalline-like film structure and the removal of the ester group gives rise to a low density SAM that has a slightly disordered liquid-like film structure.

Ellipsometry measurements were used to determine the thickness of the monolayer before and after the treatment with TFA. For the ellipsometry measurements, only half of the glass-slide coated with gold was exposed to the MHAE SAM, thus producing a substrate with the SAM only on half of the substrate. Figure 3(a) shows the thickness (height) of the monolayer from ellipsometry measurements performed in a line across from the gold side of the sample to the MHAE side. The average thickness of the MHAE layer (with reference to zero thickness of gold) was about 22.47 ± 0.23 Å. After this measurement, the whole substrate was incubated in the 50% TFA solution in ethanol for 2 minutes. Figure 3(b) shows the thickness of the monolayer after the treatment. The average thickness (height) of the MHA layer (with reference to gold) was about 14.10 ± 0.29 Å. In the former case, the higher thickness indicates that the MHAE monolayer must be close-packed and standing upright because of the presence of bulky ester group. After the treatment, when the ester group is removed, the spaced apart MHA molecules lie down or bend in order to reduce the surface energy and hence show a lesser thickness (height).

Figure 4 (a) shows a plot of the pull-off forces measured on the MHA monolayer as a function of sample bias (0V, 10V and -10V). A monolayer thickness of ~14 Å (from ellipsometry measurements) will correspond to a field strength value of 0.71 V/Å for an

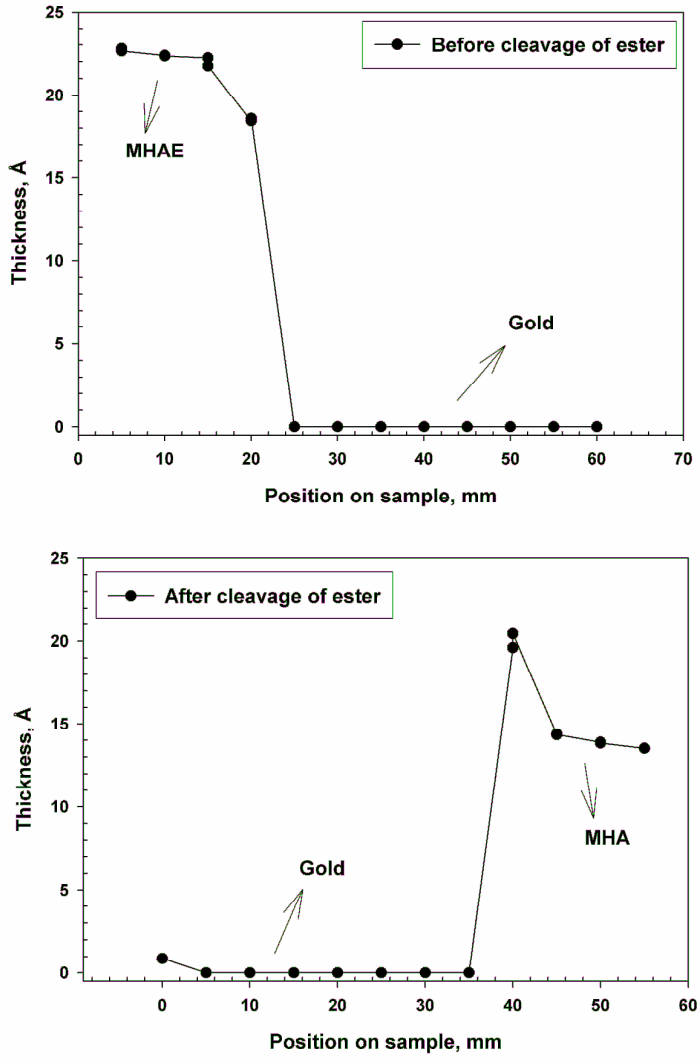

Figure 3. Thickness measurements (using ellipsometer) of the MHAE thin film (a) before treatment with TFA and (b) after treatment with TFA. The TFA treatment removes the bulky ester group, which results in a low density carboxylic acid-capped SAM system and hence a lower thickness.

applied voltage of 10V. Experiments at higher values of bias (and hence field strength) resulted in observable damage to the SAM surfaces. As a comparison, Pertsin et al.[45] performed Monte Carlo simulation studies to show that DC fields on the order of 1 V/Å can

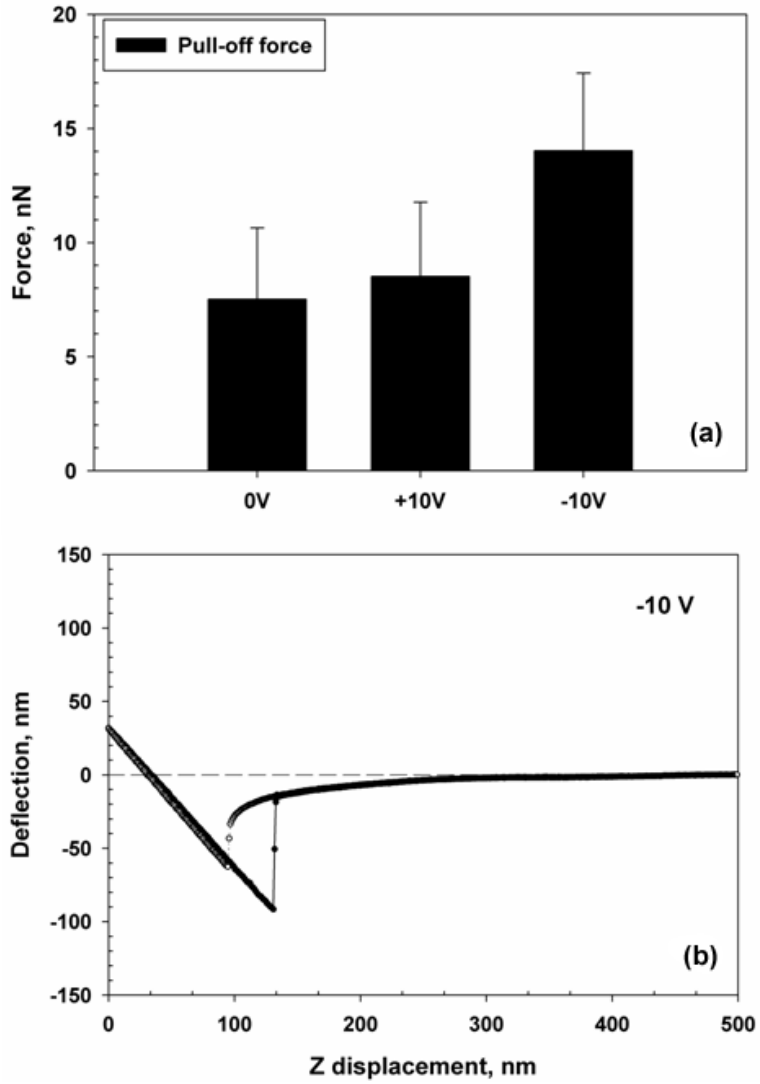

Figure 4. (a) Pull-off forces measured from AFM force curves on the MHA low density SAM system as a function of applied field (0V, +10 V and -10 V) (b) a representative force curve at -10 V showing the bending in the force curve due to the electrostatic attraction. This deflection is taken into account when calculating normal loads for friction experiments.

substantially change the equilibrium configuration of an ethylene-glycol terminated alkanethiol SAM, in particular, the oxygen atoms of the terminal group were either buried or

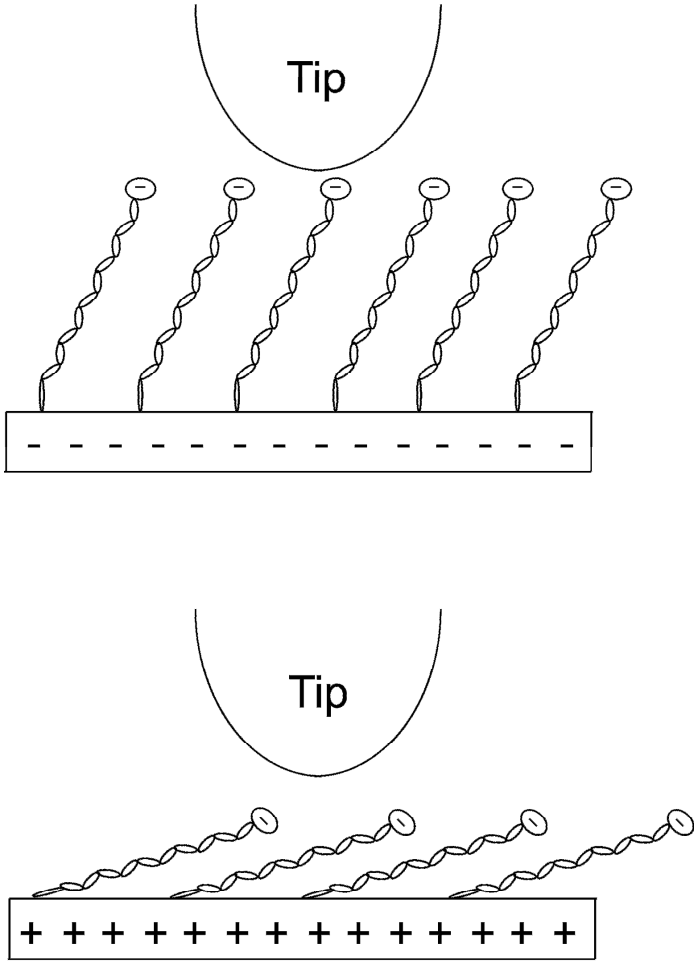

Figure 5. Schematic showing interaction of the AFM probe with the MHA molecule when a negative bias (top) and a positive bias (bottom) is applied.

exposed depending on the polarity of the applied field. Some bending of the force curve (Fig. 4 (b)) was observed during application of bias, which corresponds to deflection caused by electrostatic attraction. The difference between unbiased and biased deflection values (point of snap-in to surface of substrate) would be the amount of deflection due to electrostatic attraction, d and the normal load equivalent to this intrinsic electrostatic attraction at a particular bias (NL_{bias}) can then be calculated by multiplying the deflection by the calculated

force constant, k as $NL_{bias} = d \times k$. This additional load is taken into account while reporting normal load numbers for friction experiments.

The pull-off force is higher when a negative bias is applied than when a positive bias is applied. It is expected that when a negative bias is applied to the substrate, the resulting field will repel the carboxylic end-group and keep the molecule in a more or less upright position as shown in Figure 5(a). In this position, during a force curve experiment, these hydrophilic end groups will interact with the hydrophilic gold-coated probe. In the case of a positive bias applied to the substrate, the carboxylic molecule will be attracted towards the substrate, thus exposing the hydrophobic carbon backbone as shown in Figure 5(b). The resultant hydrophobic-hydrophilic interaction with the AFM probe would result in a lower pull-off force than in the former case. Thus the behavior of the adhesive force is indicative of the presented surface chemistry as a function of bias. This behavior is consistent with the wettability data reported by Lahann et al.[40] as a function of bias.

Our initial expectation of the friction response as a function of sample bias was to match that of the pull-off force – that is to say it would increase as the hydrophilicity of the presented end-group chemistry increased as has been shown for densely packed monolayers.[46] However, as seen in Figure 6, which shows the friction response of the low-density MHA substrate with a gold-coated conductive Si probe at 0V, +10V and -10V bias (applied to the sample), this was not the case. The data show that friction response increases with the increase in normal load in all three cases in a slightly non-linear fashion. This is commonly observed for carefully conducted friction experiments at the nanoscale[47-49] and is representative of the contact area dependence of friction.[48-50] The bias effect is illustrated by

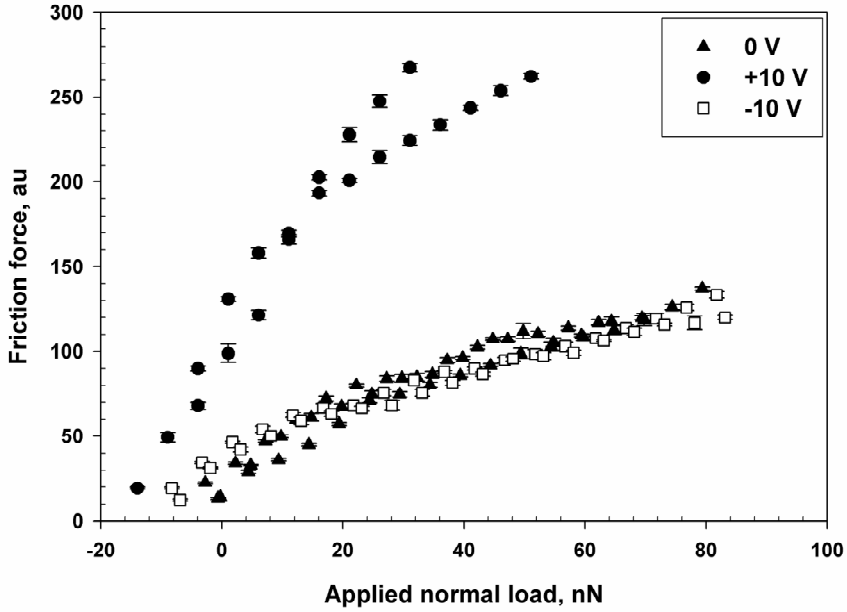

Figure 6. Data from AFM friction experiments on the MHA low density SAM for various applied fields (0V, +10 V and -10 V)

the fact that the friction response for the positive bias is much higher compared to the negative bias throughout the load range employed, which is counter to the trend seen for pull-off force. At an applied load of 40 nN, friction response for the positive bias condition is almost 3 times higher than for the negative bias condition. The friction response for the negative bias is almost equivalent to the 0V bias case at lower loads and a little lower at higher loads. Upon further investigation of the contribution to the friction force in SAM systems, it became evident that the structural order of the monolayers seems to be a critical factor in addition to presented surface chemistry. In the case of the negative bias, though the molecules are spaced apart, they are relatively ordered and well-structured. When a positive bias is applied, the bending of the molecules towards the substrate compromises the structural

order of the monolayer. Lee et al.[31] have shown that the differences in packing densities and crystalline order between an alkanethiol and spiroalkanedithiol gave rise to differing friction responses. Specifically, spiroalkanedithiol did not seem to have the ordered ($\sqrt{3}$ x $\sqrt{3}$) R30° structure and gave a higher friction response than the normal alkanethiol. Their work suggested that, when the tip traverses across the carbon backbone, which is commonly the case in disordered films than for ordered film structure, an increase in the van der waals interaction occurs, resulting in increase in shear strength per unit area and hence friction force. Applying this argument to our friction data, during positive bias, the disordered structure of the film will work to increase the friction response, whereas in the case of negative bias, the relatively ordered structure of the film will work to decrease friction response. These effects are opposite to the effect of presented surface chemistry (hydrophilicity). The fact that the observed friction does increase dramatically for the positive bias case compared to the negative bias case suggests that the contribution from the ordering of the film outweighs the contributions from presented chemistry.

8.4 Conclusions

In conclusion, we have demonstrated that an external electric field can be used as a friction switch for a low-density alkanethiol SAM film on a gold substrate. The low density allows sufficient space for field-induced conformational changes to occur as a result of attraction/repulsion between the polar end group and the substrate. AFM friction experiments, in the presence of a positive bias (+10V) show a higher friction response than a negative bias (-10V) upon application of load. The applied voltages correspond to a field

strength of approximately 0.74 V/Å. This difference in friction response upon changing the polarity of the field is attributed to the changes in the structural and crystalline (or liquid-like) order of the film. We are currently employing computational studies to further understand the nature of the conformational changes in the SAM system as well as their predicted impact on friction properties. It is expected that these efforts will lead to a better understanding of the observed friction behavior and can lead to strategies that can harness conformational changes of such film assemblies for tunable friction behavior.

References

1. Nuzzo, R. G.; Dubois, L. H.; Allara, D. L. *Journal of the American Chemical Society* **1990,** 112, (2), 558-569.

2. Bain, C. D.; Troughton, E. B.; Tao, Y. T.; Evall, J.; Whitesides, G. M.; Nuzzo, R. G. *Journal of the American Chemical Society* **1989,** 111, (1), 321-335.

3. Ulman, A. *Advanced Materials* **1990,** 2, (12), 573-582.

4. Fan, F. R. F.; Yao, Y. X.; Cai, L. T.; Cheng, L.; Tour, J. M.; Bard, A. J. *Journal of the American Chemical Society* **2004,** 126, (12), 4035-4042.

5. Stapleton, J. J.; Harder, P.; Daniel, T. A.; Reinard, M. D.; Yao, Y. X.; Price, D. W.; Tour, J. M.; Allara, D. L. *Langmuir* **2003,** 19, (20), 8245-8255.

6. Fan, F. R. F.; Yang, J. P.; Cai, L. T.; Price, D. W.; Dirk, S. M.; Kosynkin, D. V.; Yao, Y. X.; Rawlett, A. M.; Tour, J. M.; Bard, A. J. *Journal of the American Chemical Society* **2002,** 124, (19), 5550-5560.

7. Schon, J. H.; Meng, H.; Bao, Z. *Nature* **2001,** 413, (6857), 713-716.

8. Liu, Y. X.; Cui, T. H. *Journal of Nanoscience and Nanotechnology* **2005,** 5, (2), 192-197.

9. Azzaroni, O.; Schilardi, P. L.; Salvarezza, R. C. *Electrochimica Acta* **2003,** 48, (20-22), 3107-3114.

10. Kane, R. S.; Takayama, S.; Ostuni, E.; Ingber, D. E.; Whitesides, G. M. *Biomaterials* **1999,** 20, (23-24), 2363-2376.

11. Wilbur, J. L.; Kumar, A.; Biebuyck, H. A.; Kim, E.; Whitesides, G. M. *Nanotechnology* **1996,** 7, (4), 452-457.

12. Jackman, R. J.; Wilbur, J. L.; Whitesides, G. M. *Science* **1995,** 269, (5224), 664-666.

13. Sundararajan, S.; Bhushan, B. *Journal of Vacuum Science & Technology, A: Vacuum, Surfaces, and Films* **2001,** 19, (4, Pt. 2), 1777-1785.

14. Srinivasan, U.; Houston, M. R.; Howe, R. T.; Maboudian, R. *Journal of Microelectromechanical Systems* **1998,** 7, (2), 252-260.

15. Maboudian, R.; Ashurst, W. R.; Carraro, C. *Sensors and Actuators, A: Physical* **2000,** A82, (1-3), 219-223.

16. Ulman, A. *Chemical Reviews* **1996,** 96, (4), 1533-1554.

17. Koinkar, V. N.; Bhushan, B. *Journal of Vacuum Science & Technology, A: Vacuum, Surfaces, and Films* **1996,** 14, (4), 2378-2391.

18. Kim, H. I.; Koini, T.; Lee, T. R.; Perry, S. S. *Tribology Letters* **1998,** 4, (2), 137-140.

19. Lee, S.; Puck, A.; Graupe, M.; Colorado, R., Jr.; Shon, Y.-S.; Lee, T. R.; Perry, S. S. *Langmuir* **2001,** 17, (23), 7364-7370.

20. Houston, J. E.; Kim, H. I. *Accounts of Chemical Research* **2002,** 35, (7), 547-553.

21. Liu, H.; Bhushan, B. *Ultramicroscopy* **2002,** 91, (1-4), 185-202.

22. Zhang, L.; Li, L.; Chen, S.; Jiang, S. *Langmuir* **2002,** 18, (14), 5448-5456.

23. Xiao, X.; Hu, J.; Charych, D. H.; Salmeron, M. *Langmuir* **1996,** 12, (2), 235-7.

24. Lio, A.; Charych, D. H.; Salmeron, M. *Journal of Physical Chemistry B* **1997,** 101, (19), 3800-3805.

25. Kim, H. I.; Graupe, M.; Oloba, O.; Koini, T.; Imaduddin, S.; Lee, T. R.; Perry, S. S. *Langmuir* **1999,** 15, (9), 3179-3185.

26. Liu, Y.; Wu, T.; Evans, D. F. *Langmuir* **1994,** 10, (7), 2241-5.

27. Frisbie, C. D.; Rozsnyai, L. F.; Noy, A.; Wrighton, M. S.; Lieber, C. M. *Science (Washington, DC, United States)* **1994,** 265, (5181), 2071-4.

28. Brewer, N. J.; Beake, B. D.; Leggett, G. J. *Langmuir* **2001,** 17, (6), 1970-1974.

29. Lio, A.; Morant, C.; Ogletree, D. F.; Salmeron, M. *Journal of Physical Chemistry B* **1997,** 101, (24), 4767-4773.

30. Tian, F.; Xiao, X.; Loy, M. M. T.; Wang, C.; Bai, C. *Langmuir* **1999,** 15, (1), 244-249.

31. Lee, S.; Shon, Y.-S.; Colorado, R., Jr.; Guenard, R. L.; Lee, T. R.; Perry, S. S. *Langmuir* **2000,** 16, (5), 2220-2224.

32. Fujita, M.; Fujihira, M. *Ultramicroscopy* **2002,** 91, (1-4), 227-230.

33. Lavielle, L. *Wear* **1994,** 176, (1), 89-93.

34. Kimura, Y.; Nakano, K.; Kato, T.; Morishita, S. *Wear* **1994,** 175, (1-2), 143-9.

35. Hongjun, J.; Yonggang, M.; Shizhu, W.; Hong, J. *Tribology International* **1999,** 32, (3), 161-166.

36. Nakanishi, Y.; Murakami, T.; Higaki, H. *Proceedings of the Institution of Mechanical Engineering. Part H, Journal of Engineering in Medicine* 214, (2), 181-92.

37. Goto, K. *Wear* **1995,** 185, 75-81.

38. Ikeuchi, K.; Kouchiyama, M.; Tomita, N.; Uyama, Y.; Ikada, Y. *Wear* **1996,** 199, (2), 197-201.

39. Liu, H.; Fujisawa, S.; Tanaka, A.; Enomoto, Y. *Thin Solid Films* **2000,** 368, (1), 151-155.

40. Lahann, J.; Mitragotri, S.; Tran, T. N.; Kaido, H.; Sundaram, J.; Choi, I. S.; Hoffer, S.; Somorjai, G. A.; Langer, R. *Science* **2003,** 299, (5605), 371-374.

41. Peng, D. K.; Lahann, J. *Langmuir* **2007,** 23, (20), 10184-10189.

42. Torii, A.; Sasaki, M.; Hane, K.; Okuma, S. *Measurement Science & Technology* **1996,** 7, (2), 179-184.

43. Bhushan, B., *Handbook of micro/nano tribology*. 2nd ed ed.; CRC Press: Boca Raton, 1999.

44. Kanaga Karuppiah, K. S. Qunatitative friction force microscopy for micro/nanoscale friction studies of joint replacement materials. M.S. Thesis, Iowa State University, Ames, 2005.

45. Pertsin, A. J.; Grunze, M.; Kreuzer, H. J.; Wang, R. L. C. *Physical Chemistry Chemical Physics* **2000,** 2, (8), 1729-1733.

46. Leggett, G. J. *Analytica Chimica Acta* **2003,** 479, (1), 17-38.

47. Carpick, R. W.; Agrait, N.; Ogletree, D. F.; Salmeron, M. *Langmuir* **1996,** 12, (13), 3334-3340.

48. Carpick, R. W.; Agrait, N.; Ogletree, D. F.; Salmeron, M. *Journal of Vacuum Science & Technology B* **1996,** 14, (2), 1289-1295.

49. Enachescu, M.; van den Oetelaar, R. J. A.; Carpick, R. W.; Ogletree, D. F.; Flipse, C. F. J.; Salmeron, M. *Tribology Letters* **1999,** 7, (2-3), 73-78.

50. Wei, Z. Q.; Wang, C.; Bai, C. L. *Langmuir* **2001,** 17, (13), 3945-3951.

CHAPTER 9. CONCLUSIONS

Friction behavior and its contact area dependence at the micro and nanoscales

The friction behavior of two different materials, mica and ultra-high molecular weight polyethylene (UHMWPE), was evaluated at the nanoscale with an atomic force microscope (AFM) and with a custom-built ball-on-flat microtribometer at the microscale. The same counterface (Si_3N_4 probe) and environmental conditions (25 °C, RH < 10%) were maintained for all experiments. The friction force data obtained were analyzed for contact area dependence. Friction between silicon nitride and mica at the nanoscale showed initial non-linearity with normal load up to a certain load, beyond which surface damage was observed resulting in a linear dependence of friction on normal load. At the microscale, the friction of the mica-silicon nitride interface exhibited linear dependence on normal load. Friction between silicon nitride and UHMWPE exhibited non-linearity with normal load at both the length scales, for the applied load ranges of our experiment. An appropriate contact mechanics theory was applied to calculate an interfacial shear strength value for the material pair at both scales. The values at both the scales were comparable, when the conditions were carefully maintained to be the same across scales.

Effect of protein adsorption on friction behavior of UHMWPE

Medical-grade UHMWPE samples with two different surface finishing treatments, milling and melting/reforming were exposed to 10% bovine serum albumin solution and their friction responses were quantified using atomic force microscopy. The observed friction

increase upon exposure to proteins was attributed to the formation of a layer of denatured proteins on the surface. Changing the crystallinity and surface energy of UHMWPE affected the protein adsorption mechanism and the resulting increase in friction behavior.

Effect of crystallinity on friction and wear behavior of UHMWPE

In this study, the friction, wear, and surface mechanical behavior of medical grade ultra-high molecular weight polyethylene (UHMWPE) (GUR 1050 resin) were evaluated as a function of polymer crystallinity. Crystallinity was controlled by heating UHMWPE samples to a temperature above its melting point and varying the hold time and cooling rates. Degree of crystallinity of the samples was evaluated using differential scanning calorimetry (DSC). A higher degree of crystallinity in the UHMWPE resulted in lower friction force and an increase in scratch resistance at the micro and nano-scales. On the nanoscale, the lamellar structure appeared to affect the observed wear resistance. Reciprocating wear tests performed using a micro-tribometer showed that an increase in crystallinity also resulted in lower wear depth and width. Nanoindentation experiments also showed an increase in hardness values with an increase in sample crystallinity.

Effect of crystallinity in the presence of lipids on friction and wear behavior of UHMWPE

In this study, the friction and wear behavior of ultra-high molecular weight polyethylene (UHMWPE) were evaluated as a function of polymer crystallinity in the presence of the phospholipid DPPC (dipalmitoyl phosphatidylcholine) dissolved in ethanol. Samples of UHMWPE were separately heat-treated to get high and low crystallinity samples. Degree of crystallinity was evaluated using differential scanning calorimetry (DSC).

Quantitative friction and wear experiments were conducted using a custom-made microtribometer with commercially available spherical Si_3N_4 probes in controlled and phospholipid-dissolved lubricants. The higher crystallinity sample exhibited slightly lower friction than the lower crystallinity in the control, and decreased significantly when phospholipids were present. The higher crystallinity sample showed a higher wear resistance than the lower crystallinity sample during all reciprocating wear tests. DPPC acting as a lubricant had a marginal effect on the wear resistance of high crystallinity UHMWPE, whereas the low crystallinity sample became more prone to wear. AFM topography images and contact angle measurements of both samples before and after phospholipid exposure indicate that the higher crystallinity sample absorbed a greater density of DPPC. Increasing crystallinity is a way of escalating adsorption of surface active phospholipids (SAPL) onto UHMWPE, in order to make a more wear-resistant load bearing material for Total Joint Replacement.

Surface stress generation during the formation of SAMs

A high resolution curvature interferometer [Wang, J., Shrotriya, P., Kim, K.S., 2006. Surface residual stress measurement using curvature interferometry. Experimental Mechanics 46 (1), 39–46] was utilized to measure surface stress development associated with formation of self-assembled monolayers (SAM) of octadecanethiols on macroscale domains (25 mm x 25 mm). Atomistic simulations were performed to investigate surface stress generation associated with SAM formation. The results of the molecular simulations were incorporated into the multiscale framework to understand the surface stress generation and curvature change observed during experiments at continuum scale.

Active friction modulation of SAMs using external electric fields

In this study, we have perfromed initial experimental investigations to actively modulate the nanoscale properties of a self-assembled monolayer (SAM) using an external electric field that drives conformational changes in the SAM. Friction properties of a low-density -COOH terminated alkanethiol were evaluated using an atomic force microscope (AFM) in the presence of a DC bias applied between the sample and the AFM probe under ambient conditions. The low density allows reorientation of the SAM molecules to accommodate the attractive force between the –COOH terminal group and a positively biased surface. This enables the surface to present a hydrophilic group or a hydrophobic backbone depending upon the direction of the field (bias), thereby exhibiting a modulation in the friction response when in contact with an AFM probe. Synthesis and deposition of the low-density SAM (LD-SAM) is reported. XPS and ellipsometry have been used to confirm the presence and thickness of the monolayer respectively. Results from AFM experiments showed that the increased friction response of the LD-SAM system in the presence of a positive bias and a decreased friction response in the presence of a negative bias. The difference in the friction response is attributed to the change in the structural and crystalline order of the film upon application of the bias.

APPENDIX

MATLAB code for fitting a parabola to tip shape and determination of tip radius

Program to read the DI image

```
function [im1a,im1b] = readimage(file)
fid = fopen(file,'rt');
for ii =1:110
  fgets(fid);
end;
test=fgets(fid);
soft=str2num(test(18:26));
for ii=114:544
  fgets(fid);
end
test=fgets(fid);
hard=str2num(test(49:58));
fclose(fid);
fid = fopen(file,'r','n');
fseek(fid,40960,'bof');
im1 = fread(fid,[256,512],'bit16');
im1a = (hard*soft)*((im1(:,1:256)-min(min(im1(:,1:256)))))/65536;
```

```
%im1b = im1(:,257:512);
Return
```

Program to locate the maximum points on x and y profile

```
function [p1,p2] = locate( xpts,ypts,imsize )
%This program takes the information about the tip across the x-axis and y-axis and finds the
max pts along the top of the tip%

imsize1=imsize/256*1000;
h=size(xpts);
g=size(ypts);
h1=(1:h(1))*imsize1;
h2=(1:h(2))*imsize1;
g2=(1:g(2))*imsize1;
g1=(1:g(1))*imsize1;

yfit=max(xpts');
xfit=max(ypts);

p1=figure;
subplot(2,1,1); plot(h2,xpts')
subplot(2,1,2); plot(g2,xfit)
```

```
p2=figure;
subplot(2,1,1); plot(g1,ypts)
subplot(2,1,2); plot(h1,yfit)
[X1,RES1,fig1,Rc] = curve(yfit,imsize1);
[X2,RES2,fig2,Rc2] = curve(xfit,imsize1);
return;
```

Program for fitting a parabola

```
function [X,RES,ydata,f] = fitting(x0,ydata)

%Input the name of your file in the load function. The first column of the data file should be
(xnot) values. The second col. should be y values. The function then utilizes a nonlinear least
square fit to fit the function f.

for i=1:length(ydata)
xdata(i)=i;
end
ydata=ydata;

f = inline('x(1)*(xdata).^2+x(2)*xdata+x(3)','x','xdata');
[x,resnorm]=lsqcurvefit(f,x0,xdata(:),ydata(:));
```

```
x0=x;
[x,resnorm] = lsqcurvefit(f,x0,xdata,ydata);
%The unknown values along with the residual value are passed out of the function
X=x;
RES=resnorm;
```

Program for best fit by iterative routine

```
function [X,RES,fig,Rc,xmax] = curve(ydata,imsize)

%This program utilizes fitting.m to find the lowest residual value and the best fit.  It then
plots the laboratory data against the best fit line and gives values for the radius of curvature
and curvature in (nm).

y=ydata;
x0=[1,.2,325];
[X,RES,y,f] = fitting(x0,y);
n=0;
while (RES)>=1e-6
   x0=X;
   [X,RES,y,f] = fitting(x0,y);
   n=n+1;
   if n==30
```

```
        break
    end
end
X
RESIDUAL=RES;
%Post processing
X(1)=X(1)/imsize.^2;
X(2)=X(2)/imsize;
xmax=-X(2)/(2*X(1))
%calculate the radius of curvature
kappa=2*X(1)/((2*X(1)*xmax).^2+4*X(1)*xmax*X(2)+X(2).^2+1).^(3/2);
Rc=1/kappa
X(1)=X(1)*imsize.^2;
X(2)=X(2)*imsize;
%End post processing

for i=1:length(y)
xdata(i)=i;
end

%Plotting laboratory data against best fit line
fig=figure; hold
```

```
plot(xdata*imsize,f(X,xdata))

plot(xdata*imsize,y,'o')

xlabel('nm')

ylabel('Height Data (nm)')

legend('NL least sq','data',sprintf('Radius of Curv. = %1.5f',Rc))

title('Find Radius of Curvature ')

return;
```